Werkstofftechnik

UNIVERSITÄT SIEGEN

Ximan Dong

Folded Nanocrystalline-Stacked WO_3 with Photo-Enhanced Functionality for High-Performance Ammonium-ion Storage

Schriftenreihe der Arbeitsgruppe
des Lehrstuhls für Oberflächen- und Werkstofftechnologie
im Institut für Werkstofftechnik

Herausgeber: Prof. Dr. rer. nat. habil. Xin jiang

Band 23

Ximan Dong

Folded nanocrystalline-stacked WO_3 with photo-enhanced functionality for high-performance ammonium-ion storage

Schriftenreihe der Arbeitsgruppe des Lehrstuhls für Oberflächen- und Werkstofftechnologie im Institut für Werkstofftechnik

Impressum

Prof. Dr. rer. nat. habil. Xin Jiang

Lehrstuhl für Oberflächen- und Werkstofftechnologie

Institut für Werkstofftechnik

Universität Siegen

57076 Siegen

ISSN: 2194-0096

Zugl.: Siegen, Univ., Diss., 2026

Folded nanocrystalline-stacked WO_3 with photo-enhanced functionality for high-performance ammonium-ion storage

Von der Naturwissenschaftlich-Technischen Fakultät
der Universität Siegen

zur Erlangung des Grades eines Doktors
der Ingenieurwissenschaften
genehmigte

Dissertation

von:	M.Sc. Ximan Dong
eingereicht am:	19. November 2025
Mündliche Prüfung am:	27. March 2026
Referent:	Prof. Dr. rer. nat. habil. Xin Jiang
Korreferent:	Prof. Dr. Nianjun Yang

Kurzfassung

Die Integration der Lichtnutzung mit elektrochemischer Energiespeicherung wird zunehmend als vielversprechender Weg zur Bewältigung der globalen Energiekrise anerkannt. Durch die direkte Kopplung der Photonabsorption mit Ionenspeicherungsprozessen bieten lichtunterstützte Energiespeichersysteme einzigartige Vorteile gegenüber herkömmlichen Batterien und Kondensatoren. Diese intrinsische Synergie verbessert nicht nur die Geräteleistung, sondern eröffnet auch neue Möglichkeiten für solarwiederaufladbare Energiespeichertechnologien. Unter den verschiedenen wässrigen Energiespeichersystemen haben sich ammoniumionenbasierte Geräte aufgrund ihres einzigartigen, wasserstoffbrückengetriebenen Insertionsmechanismus von NH_4^+, der einen schnellen Ionentransport und eine hohe Reversibilität in milden wässrigen Elektrolyten ermöglicht, als vielversprechende Kandidaten erwiesen. Die Integration einer solchen NH_4^+-Speicherchemie mit photoaktiven Elektroden könnte die Funktionalität wässriger Systeme weiter in Richtung lichtunterstützter Ladungsspeicherung erweitern. In Verbindung mit Ammonium-Ionen-Hybrid-Superkondensatoren (AIHSs) stellt dieses Konzept ein attraktives und neuartiges wässriges Energiespeichersystem dar, das durch geringe Kosten, inhärente Sicherheit, Umweltfreundlichkeit und einzigartige, wasserstoffbrückengetriebene Insertionsmechanismen überzeugt. Um diese besonderen Eigenschaften zu erreichen, müssen AIHSs insbesondere mit photoaktiven Elektroden gekoppelt werden, die sowohl eine hohe Leistungsfähigkeit als auch lichtverstärkte Ladungsspeicherung bieten.

Diese Dissertation konzentriert sich daher auf das rationale Design von WO_3-basierten Elektroden mit photoverstärkter Funktionalität zur effizienten Speicherung von Ammonium-Ionen. Durch die Entwicklung gefalteter nanokristallin–amorpher WO_3-Strukturen, von WO_3/TiO_2-Heteroübergängen und WO_3/BDD-Kompositen wird in dieser Arbeit systematisch die Struktur–Eigenschaft–Leistungs-Beziehung etabliert und es werden neue Designprinzipien zur Konstruktion leistungsstarker, solarresponsiver wässriger Energiespeichergeräte aufgezeigt. Drei experimentelle Teile werden im Folgenden im Detail beschrieben.

I) Gefaltete nanokristallin–amorphe WO_3-Elektroden: Die gefalteten, nanokristallin gestapelten amorphen WO_3 (a-WO_3)-Elektroden wurden mittels eines schnellen elektrochemischen Abscheidungsverfahrens synthetisiert. Sie besitzen hierarchische Strukturen, in denen ~5 nm große Kristallite locker in eine amorphe Matrix eingebettet

sind. Ihre umfassende Charakterisierung erfolgte mittels Mikroskopie, Spektroskopie, elektrochemischer Methoden und Dichtefunktionaltheorie-Simulationen. Besonders wichtig war die Untersuchung des Zusammenhangs zwischen struktureller Architektur, Defektchemie und NH_4^+-Speicherleistung. Die a-WO_3-Elektroden zeigten eine überlegene elektrochemische Aktivität mit einer Kapazität von 2783 mF cm^{-2} und hervorragender Ratenleistung im Vergleich zu kristallinen Gegenstücken. Es wurde bestätigt, dass die amorphe Struktur zahlreiche Korngrenzen, Sauerstoffleerstellen und gemischtvalente Wolframzustände bietet, die den schnellen NH_4^+-Transport durch Wasserstoffbrückenbindungen erleichtern. Als Demonstration wurde die a-WO_3-Elektrode zur Herstellung eines vollständigen Ammonium-Ionen-Hybrid-Superkondensators mit einer Polyanilin-Kathode verwendet. Dieser Superkondensator liefert bemerkenswerte Energie- und Leistungsdichten von 620 mWh cm^{-2} bzw. 23.980 mW cm^{-2} und zeigt nach 3000 Zyklen noch 81,5 % Kapazitätserhalt. Diese Ergebnisse unterstreichen die Wirksamkeit der kontrollierten Amorphisierung als Strategie, um die intrinsischen Einschränkungen von kristallinem WO_3 zu überwinden und gleichzeitig hohe Kapazität und Haltbarkeit zu erreichen. Alle diese Ergebnisse sind in *Kapitel 3* dargestellt.

II) WO_3/TiO_2-Heteroübergänge für lichtunterstützte Energiespeicherung: Die WO_3/TiO_2-Heterokomposite wurden mit dem Ziel entwickelt, lichtverstärkte Energiespeicherfähigkeiten durch synergetische optische und elektrochemische Eigenschaften zu nutzen. Die Bandanpassung zwischen WO_3 und TiO_2 wurde verwendet, um Typ-II-Heteroübergänge zu konstruieren, die die hervorragende Photokatalyseaktivität von TiO_2 und die Fähigkeit zur Ladungstrennung ausnutzen, um letztlich die elektrochemische Leistung von WO_3 zu verbessern. Durch gezielte Steuerung der elektrochemischen Abscheidungsparameter wurden inselartig verteilte WO_3-Nanokristalle auf TiO_2 abgeschieden, wodurch eine gleichzeitige Exposition beider Materialien gegenüber dem Elektrolyten gewährleistet und echte Synergieeffekte statt einer einfachen seriellen Kopplung erzielt wurden. Diese inselartige Wachstumsweise maximiert die Heteroübergangsfläche, fördert eine effiziente Ladungstrennung und verbessert den Ladungstransport. Die TiO_2-Komponente bietet eine überlegene Photokatalyseaktivität und erweitert den photoaktiven Spektralbereich, während WO_3 eine hohe NH_4^+-Speicherfähigkeit liefert. Eine umfassende Charakterisierung dieser Verbundelektroden zeigt eine verbesserte Lichtabsorption, optimierte Ladungsträgerdynamik und beschleunigte Ionentransportkinetik unter Beleuchtung.

Unter Lichtbestrahlung zeigte das typische Verbundmaterial eine um 40 % erhöhte Kapazität im Vergleich zu Dunkelbedingungen, einen deutlich verringerten Ladungstransferwiderstand um 80–85 %, eine Photostromdichte von 0,47 mA cm^{-2} sowie eine deutlich verbesserte Ladungsträgerdichte und Grenzflächenkinetik. All diese Ergebnisse bestätigen die Effektivität des Heteroübergangsdesigns für die lichtunterstützte Energiespeicherung. Diese Details sind in *Kapitel 4* zusammengefasst.

III) WO_3/BDD-p–n-Übergang für lichtunterstützte Energiespeicherung: Dieser Abschnitt befasst sich mit den anhaltenden Leitfähigkeitsbeschränkungen von WO_3-Elektroden durch die Integration von bor-dotiertem Diamant (BDD), einem Kohlenstoffmaterial mit weitem Potentialfenster, hoher Leitfähigkeit und chemischer Stabilität. Die strategische Kombination erzeugt eine p–n-Übergangskonfiguration, die das ultrabreite Bandgap von Diamant (5,5 eV) und die hervorragenden elektronischen Eigenschaften von p-Typ-BDD an der Grenzfläche zu n-Typ-WO_3 nutzt. Das intrinsische elektrische Feld am Übergang verbessert die Effizienz der Ladungstrennung, während die außergewöhnliche Leitfähigkeit von BDD die NH_4^+-Speicherfähigkeit von WO_3 ergänzt. Im Vergleich zu reinem WO_3 zeigte das Komposit eine etwa 1,7-fach höhere Photostromdichte, und die Flächenkapazität unter Beleuchtung wurde um nahezu 20 % erhöht. Darüber hinaus behielt die Elektrode nach längerer Zyklisierung über 90 % ihrer Kapazität und übertraf damit das reine WO_3. Der WO_3/BDD-p–n-Übergang liefert somit eine deutlich erhöhte Photostromantwort, verbesserte NH_4^+-Speicherkapazität unter Beleuchtung und verlängerte Lebensdauer. Das eingebaute elektrische Feld erleichtert den gerichteten Ladungstransport und unterdrückt Rekombinationsverluste, was zu einer überlegenen photoelektrochemischen Leistung führt. Diese Ergebnisse werden in *Kapitel 5* dargestellt.

Zusammenfassend bietet diese Dissertation mehrere erfolgreiche Ansätze für das Design und die Optimierung WO_3-basierter Elektrodenmaterialien für nachhaltige Ammonium-Ionen-Energiespeicheranwendungen durch fortschrittliches Strukturdesign und innovative Photoverstärkungsstrategien. Durch die Entwicklung gefalteter nanokristallin gestapelter Architekturen, die Konstruktion von Typ-II- und p–n-Heteroübergängen sowie die Integration photokatalytischer Funktionalitäten wird in dieser Arbeit das große Potenzial von WO_3 bei der Realisierung leistungsfähiger, umweltfreundlicher Energiespeichergeräte mit dualer Solarenergienutzung und elektrochemischer Speicherung aufgezeigt. Die systematische Untersuchung der lichtunterstützten Mechanismen verdeutlicht, dass die Bildung von Heteroübergängen eine effiziente

Ladungstrennung ermöglicht, Rekombinationsverluste reduziert und die elektrochemische Leistung unter Beleuchtung deutlich verbessert. Diese Arbeit etabliert grundlegende Designprinzipien für photoresponsive Elektrodenmaterialien. Über die Ammonium-Ionen-Speicherung hinaus eröffnen die hier vorgestellten Strategien neue Wege für multifunktionale wässrige Systeme, die gleichzeitig Sonnenenergie ernten und Ionen speichern können.

Abstract

The integration of light harvesting with electrochemical energy storage has been increasingly recognized as a promising pathway to address the global energy crisis. By directly coupling photon absorption with ion storage processes, photo-assisted energy storage systems offer unique advantages over conventional batteries and capacitors. This intrinsic synergy not only enhances device performance but also opens new opportunities for solar-rechargeable energy storage technologies. Among various aqueous energy-storage systems, ammonium-ion-based devices have recently emerged as promising candidates owing to the unique hydrogen-bond-driven insertion mechanism of NH_4^+, which enables fast ion transport and high reversibility in mild aqueous electrolytes. Integrating such NH_4^+ storage chemistry with photoactive electrodes could further expand the functionality of aqueous systems toward light-assisted charge storage. Married this context with ammonium-ion hybrid supercapacitors (AIHSs), this concept represents an attractive and novel aqueous energy storage system, thanks to their low cost, intrinsic safety, environmental benignity, and unique hydrogen-bond-driven insertion mechanisms. To achieve these distinctive features, AIHSs particularly need to be coupled with photoactive electrodes featuring both high-performance and light-enhanced charge storage.

This dissertation thus focuses on the rational design of WO_3-based electrode owning photo-enhanced functionality for efficient ammonium-ion storage. Through the development of folded nanocrystalline–amorphous WO_3 structures, WO_3/TiO_2 heterojunctions, and WO_3/BDD composites, this work systematically establishes structure–property–performance relationship and demonstrates new design principles to construct high-performance, solar-responsive aqueous energy storage devices. Three experimental parts are detailed as follows.

I) Folded nanocrystalline–amorphous WO_3 electrodes: The folded nanocrystalline-stacked amorphous WO_3 (a-WO_3) electrodes were synthesized *via* a rapid electrochemical deposition method. They own hierarchical frameworks where ~5 nm crystallites are loosely assembled within an amorphous matrix. Their comprehensive characterization was conducted using microscopy, spectroscopy, electrochemical techniques, and density functional theory simulations. More importantly, the relationship between structural architecture, defect chemistry, and NH_4^+ storage performance was investigated in detail. The a-WO_3 electrodes demonstrated superior electrochemical

activity with a capacitance of 2783 mF cm^{-2} and excellent rate performance compared to crystalline counterparts. The amorphous structure is confirmed to provide abundant grain boundaries, oxygen vacancies, and mixed-valence tungsten states, facilitating rapid NH_4^+ transport through hydrogen bonding mechanisms. As a demonstration, the a-WO_3 electrode was employed to construct a full ammonium-ion hybrid supercapacitor with a polyaniline cathode. This supercapacitor delivers remarkable energy and power densities of 620 mWh cm^{-2} and 23,980 mW cm^{-2}, respectively, further with 81.5% capacity retention after 3000 cycles. These results highlight the effectiveness of controlled amorphization as a strategy to overcome the intrinsic limitations of crystalline WO_3 and achieve both high capacity and durability. All these are shown in Chapter 3.

II) WO_3/TiO_2 heterojunctions for light-assisted energy storage: The WO_3/TiO_2 heterojunction composites were designed with an aim to harness photo-enhanced energy storage capabilities through synergistic light and electrochemical properties. The band alignment between WO_3 and TiO_2 was utilized to engineer Type II heterojunctions, which leverage the superior photocatalytic activity of TiO_2 and charge separation capability, eventually enhancing electrochemical performance of WO_3. Through controlled electrochemical deposition parameters, island-like distributed WO_3 nanocrystals have been coated on TiO_2, ensuring simultaneous exposure of both materials to the electrolyte and meanwhile achieving true synergistic effects rather than simple serial coupling. This island-like growth mode maximizes the heterojunction interface area, promoting efficient charge separation and transport. The TiO_2 component provides superior photocatalytic activity and extends the photoactive spectral range, while WO_3 offers high-capacity NH_4^+ storage capability. Comprehensive characterization of these composite electrodes reveals their enhanced light absorption, improved charge carrier dynamics, and accelerated ion transport kinetics under illumination. Under light irradiation, the typical composite material showed 40% capacity enhancement compared to that under dark conditions, with a significantly reduced charge transfer resistance by a factor of 80-85%, a photocurrent density of 0.47 mA cm^{-2}, and substantially improved carrier density and interfacial kinetics. All these validate the effectiveness of heterojunction design in achieving photo-assisted energy storage. These details are summarized in Chapter 4.

III) WO_3/BDD p-n junction for light-assisted energy storage: This session addresses the persistent conductivity limitations of WO_3 electrodes by incorporating boron-doped diamond (BDD), a carbon material known for its wide potential window, high conductivity, and chemical robustness. The strategic combination creates a p–n junction

configuration that exploits the ultra-wide bandgap of diamond (5.5 eV) and the superior electronic properties of p-type BDD interfaced with n-type WO_3. The intrinsic electric field at the junction enhances charge separation efficiency, while the exceptional conductivity of BDD complements the NH_4^+ storage capability of WO_3. Compared with pristine WO_3, the composite delivered a ~1.7-fold higher photocurrent density and the areal capacitance under light was enhanced by nearly 20%. In addition, the electrode maintained over 90% of its capacity after extended cycling, outperforming pristine WO_3. Therefore, the WO_3/BDD p–n junction delivers significantly enhanced photocurrent response, improved NH_4^+ storage capacity under illumination, and extended cycling lifetime compared to pristine WO_3. The built-in electric field facilitates directional charge transport and suppresses recombination losses, resulting in superior photoelectrochemical performance. These results are demonstrated in Chapter 5.

In summary, this thesis provides several successful approaches to design and optimize WO_3-based electrode materials for sustainable ammonium-ion energy storage applications in the way of both advanced structural engineering and innovative photo-enhancement strategies. By developing folded nanocrystalline-stacked architectures, engineering Type II and p-n heterojunctions, and integrating photocatalytic functionalities, the great potential of WO_3 in achieving high-performance, environmentally friendly energy storage devices have been proved in this thesis. They also feature dual solar energy harvesting and electrochemical storage capabilities. Such systematic investigation of photo-assisted mechanisms clarifies that heterojunction formation enables efficient charge separation, reduces recombination losses, and significantly enhances electrochemical performance under illumination. This work establishes fundamental design principles for photo-responsive electrode materials. Beyond ammonium-ion storage, the strategies presented here open new avenues for multifunctional aqueous devices capable of simultaneously harvesting solar energy and storing ions.

Acknowledgements

This dissertation was completed during my work as a research associate at the Chair of Surface and Materials Technology, Institute of Materials Engineering (LOT), University of Siegen and at the Faculty of Sciences, Hasselt University. At this point, I would like to take this opportunity to express my heartfelt gratitude to all those who have supported and encouraged me during this challenging yet rewarding journey.

First, I would like to express my deepest appreciation to my supervisor, Prof. Xin Jiang, for his continuous guidance and generous support throughout my doctoral studies at the University of Siegen. He has always been exceptionally friendly and encouraging, patiently guiding me step by step while also allowing me the freedom to explore new ideas. His generous support, insightful guidance in defining the direction of my research, and his passion for science have constantly kept me motivated throughout my studies. I am deeply indebted to him for granting me the invaluable opportunity to pursue independent exploration, which has greatly shaped both my academic development and personal growth.

I am sincerely grateful to Prof. Nianjun Yang, whose support gave me the opportunity to pursue my doctoral studies at the University of Siegen and the good fortune to become a Joint-PhD at Hasselt University as well. Our numerous discussions have always been thought-provoking and inspiring, often bringing me fresh ideas and new directions for my research. Moreover, he provided me with numerous opportunities to attend academic conferences, where I was able to meet leading scholars in the field and greatly broaden my academic and personal horizons. Beyond research, I am especially thankful to him and his wife, Dr. Wang, for their kind support in many aspects of my daily life, which has been invaluable during my years abroad.

I would also like to extend my sincere thanks to my defense committee members, Prof. Quan-Hong Yang, Prof. Ken Haenen, Prof. Hyacinthe Randriamahazaka, Prof. Robert Brandt, and Prof. Holger Schönherr for their insightful comments and constructive feedback, which have been significant in improving and refining this dissertation.

My special thanks go to my colleagues in the LOT research group. Your assistance, collaboration, and companionship have made my research journey more productive and enjoyable. Great thanks are given to Dr. Xinyue Chen, with whom I have shared encouragement and mutual support over the past four years. Our cooperation has gone far beyond research; together we have also explored the meaning of life, which has made this period both inspiring and memorable. I am also grateful to Changli Li for his generous help, as he provided me with diamond samples for my research and often took on the responsibility of driving when I needed to travel to Hasselt University. My sincere thanks also go to Yao Li, who always offered me delicious food, bringing warmth and care into my daily life. I am deeply thankful to Dr. Chuyan Zhang and Dr. Zhaofeng Zhai, whose dedication to their own research has been a constant source of inspiration. Other colleagues from LOT are also highly appreciated. They are Dr. Thorsten Staedler, Dr. Kevin Suta, Dr. Hamid Ullah, Dr. Aleksandr Zubtsovskii, Dr. Akif Zeb, Petra auf dem Brinke, Tianxiao Guo, Claudia Kretzer, Bharath Reddy Lakki Reddy Venkata, Stefan Wagener, and Chen Wang. Especially, many thanks are given to Ms Andrea Brombach who fully supported me and my research with respect to ordering and office issues during my doctoral study.

Apart from my colleagues at the University of Siegen, I would also like to express my sincere gratitude to my colleagues at Hasselt University. I am especially thankful to Shuang Liu, who kindly helped me with numerous matters during my stay in Hasselt. Her generous support made my time there much smoother and more enjoyable.

Finally, I would like to express my deepest gratitude to my friends and family. I am truly thankful to my friends, whose companionship and kindness have brought joy and warmth to this journey. To my family, I would like to say: 非常感谢我的家人给予我不断的支持和无条件的爱，尊重我并支持我成长路上的每一个选择，给了我肆意成长和追求梦想的自由和勇气。

Publication list

1. **Ximan Dong**, Pei Li, Xinyue Chen, Yue Chu, Chuyan Zhang, Aleksandr Zubtsovskii, Ziyang Lu, Changli Li, Renée S. Hoffmann, Felix Thiel, Peter Haring Bolívar, Nan Huang, Holger Schönherr, Quan-Hong Yang, Xin Jiang, Nianjun Yang, Folded Nanocrystalline-Stacked WO_3 for Efficient Ammonium-Ion Storage, *Energy Storage Mater.* 2026, 86, 104932.
2. **Ximan Dong**, Xinyue Chen, Xin Jiang, Nianjun Yang, Light-Assisted Energy Storage Devices: Principles, Performance, and Perspectives, *Advanced Energy Materials,* 2023, *13* (38), 2301143.
3. Xiyue Chen, **Ximan Dong**, Xin Jiang, Nianjun Yang, Diamond Composite: A "1+ 1> 2" Strategy to Design and Explore Advanced Functional Materials, *Accounts of Materials Research*, 2024, *5* (3), 295-306.
4. Changli Li, **Ximan Dong**, (co-author) Zhaofeng Zhai, Nan Huang, Xin Jiang, Nianjun Yang, High-Performance Flexible Supercapacitors Using Diamond Cloth, *The Journal of Physical Chemistry C*, 2025, *129* (14), 6618-6627.
5. Xinyue Chen, **Ximan Dong**, Chuyan Zhang, Meng Zhu, Essraa Ahmed, Giridharan Krishnamurthy, Rozita Rouzbahani, Paulius Pobedinskas, Nicolas Gauquelin, Daen Jannis, Kawaljit Kaur, Aly Mohamed Elsayed Hafez, Felix Thiel, Rainer Bornemann, Carsten Engelhard, Holger Schönherr, Johan Verbeeck, Ken Haenen, Xin Jiang, Nianjun Yang, Interlayer Affected Diamond Electrochemistry, *Small methods*, 2025, *9* (2), 2301774.

Content

Kurzfassung ..... **I**

Abstract ..... **V**

Acknowledgements **9**

Publication list **11**

Content ..... **I**

Symbol List ..... **IV**

Symbols ..... **VII**

Units ..... **VIII**

1 Introduction **1**

1.1 Overview 1

1.2 Energy landscape: why light-electrochemical synergy? 3

1.2.1 Current applications and research status 4

1.2.2 Working principles of photo-assisted energy storage devices 6

1.3 Ammonium ion storage 7

1.3.1 Fundamental principles and theoretical framework 8

1.3.2 Current research progress 10

1.4 Electronic structure and intercalation phenomena of tungsten oxide 12

1.4.1 Electronic structure of tungsten oxide 12

1.4.2 Ion intercalation phenomena in tungsten oxide 14

1.5 Composite design: heterojunctions and synergy 17

1.5.1 Type-II Heterojunctions 18

1.5.2 p–n Junctions 18

1.5.3 Z-Scheme Systems 18

1.6 Outline of this thesis 19

2 Experimental **22**

2.1 Material preparation 22

2.1.1 Electrochemical deposition 22

2.1.2 Magnetron sputtering 23
2.1.3 Microwave plasma enhanced chemical vapor deposition 24
2.1.4 Thermal chemical vapor deposition 25
2.2 Materials preparation 26
2.2.1 Substrate preparation 26
2.2.2 Electrochemical deposition of WO_3 26
2.2.3 Synthesis of h-WO_3 electrodes 27
2.2.4 Synthesis of PANI electrodes 28
2.2.5 Preparation of WO_3/TiO_2 Composites 28
2.2.6 Preparation of WO_3/BDD Composites 30
2.3 Material Characterization 33
2.3.1 Scanning electron microscopy 33
2.3.2 Transmission electron microscope 33
2.3.3 Raman spectroscopy 34
2.3.4 X-ray diffraction 35
2.4 Surface chemistry analysis 35
2.4.1 X-ray photoelectron spectroscopy 35
2.4.2 N_2 adsorption and desorption 36
2.5 Electrochemical measurements 36
2.5.1 Cyclic voltammetry 37
2.5.2 Galvanostatic charge-discharge 38
2.5.3 Electrochemical impedance spectroscopy 38
2.5.4 Mott–Schottky analysis 39
2.5.5 Linear sweep voltammetry 39
2.5.6 Amperometry (*i–t* curves) 40
2.6 Photo-assisted electrochemical measurements 41
2.7 Calculations Section 41
2.8 Density functional theory (DFT) calculations 42

3 WO_3 materials for ammonium-ion hybrid supercapacitor 43

3.1 Design of folded nanocrystalline-stacked WO_3 structure 44

3.2 Growth mechanism of the folded nanocrystalline-stacked the WO_3 51

3.3 Storage mechanism about NH_4^+ ion in the WO_3 58

3.4 The performance of the ammonium-ion hybrid supercapacitor 64

3.5 Conclusion 66

4 WO_3/TiO_2 heterojunctions for light-assisted energy storage 68

4.1 Band diagram analysis of WO_3/TiO_2 photo-assisted ammonium ion storage mechanism 69

4.2 Material preparation and characterization 71

4.3 Electrochemical and photoelectrochemical performance 76

4.4 photoelectrochemical performance towards ammonium ion storage 78

4.5 Conclusions 92

5 WO_3/BDD p-n junction for light-assisted energy storage 93

5.1 Working principle of WO_3/BDD photo-enhanced electrode 94

5.2 Characterization of WO_3/BDD composites 96

5.3 Electrochemical performance of the WO_3/BDD composites 99

5.5 Conclusions 109

6 Summary and outlook 111

6.1 Summary 111

6.2 Outlook 113

6.2.1 Advanced characterization of nanocrystalline structures 113

6.2.2 Dual-ion systems and multi-chemistry integration 114

6.2.3 Advanced characterization of photo-enhancement mechanisms 114

7 References 116

Symbol List

Abbreviations

AIHSs	ammonium-ion hybrid supercapacitors
AIBs	ammonium-ion batteries
AC	alternating current
BDD	boron-doped diamond
BET	Brunauer–Emmett–Teller
BJH	Barrett–Joyner–Halenda
CB	conduction band
CC	carbon cloth
CE	counter electrode
CV	cyclic voltammetry
CVD	chemical vapor deposition
DC	direct current
Dia	diamond
DFT	density functional theory
DOS	density of states
E_{FB}	flat-band potential
ECR	electron cyclotron resonance
EDS	energy-dispersive spectrometer
EDLC	electrical double-layer capacitor
EIS	impedance spectroscopy
ELNES	energy-loss near edge structure
FE	faradaic efficiency
FETs	field-effect transistors
PEO	plasma electrolytic oxidation
GCD	galvanostatic charge and discharge

HFCVD	hot filament chemical vapor deposition
HPHT	high pressure-high temperature
HER	hydrogen evolution reaction
LAES	light-assisted energy storage
LIBs	lithium-ion batteries
LSV	linear sweep voltammetry
MPCVD	microwave plasma chemical vapor deposition
MWCVD	microwave chemical vapor deposition
NHE	normal hydrogen electrode
OCP	open circuit potential
OCV	open circuit voltage
OER	oxygen evolution reaction
OEP	oxygen evolution potential
PAW	projector augmented wave method
PC	pseudocapacitor
pH	potential of hydrogen
PV	photovoltaic
PVD	physical vapor deposition
RHE	reversible hydrogen electrode
RE	reference electrode
RF	radio frequency
SEM	scanning electron microscope
STEM-EELS	scanning transmission electron microscopy - electron energy loss spectroscopy
TCVD	thermal chemical vapor deposition
TEM	transmission electron microscope
UV-VIS	ultraviolet spectroscopy or ultraviolet-visible
VASP	vienna ab initio simulation package

VB	valence band
WE	working electrode
XPS	X-ray photoelectron spectroscopy
XRD	x-ray diffraction

Chemicals

ANI	aniline
Al	aluminum
APS	ammonium persulfate
Ar	argon
B	boron
C	carbon
CdS	cadmium sulfide
C_3N_4	graphitic carbon nitride
CH_4	methane
Cu	copper
$Cu_3[Fe(CN)_6]_2$	copper (II) hexacyanoferrate
$Fe(CN)_6^{3-/4-}$	ferricyanide/ferrocyanide
$Fe_4[Fe(CN)_6]_3$	iron (III) hexacyanoferrate
H_2	hydrogen
H_2SO_4	sulfuric acid
HCl	hydrochloric acid
H_2O_2	hydrogen peroxide
K	potassium
MnO_2	manganese dioxide
MoS_2	molybdenum disulfide
MoO_3	molybdenum trioxide
Mg	magnesium
Li	lithium

LSV	linear sweep voltammetry
N	nitrogen
N_2	nitrogen gas
Na	sodium
Na_2SO_4	sodium sulfate
$NaFe[Fe(CN)_6]$	sodium iron hexacyanoferrate
$Na_2WO_4 \cdot 2H_2O$	sodium tungstate dihydrate
NH_3	sulfamic acid
NH_4Cl	ammonium chloride
$(NH_4^+)_xWO_3$	ammonium tungsten bronze
O_2	oxygen
PANI	polyaniline
Pt	platinum
TMS	tetramethylsilane
Ti	titanium
TiO_2	titanium dioxide
TMB	trimethyboron
V_2O_5	vanadium Pentoxide
VO_x	vanadium Oxide with variable stoichiometry
VS_2	vanadium Disulfide
W	tungsten
WO_3	tungsten oxide
WO_6	tungsten (VI) oxide octahedron
$W_{18}O_{49}$–O_v	oxygen-deficient tungsten oxide ($W_{18}O_{49}$ with oxygen vacancies)
Zn	zinc

Symbols

C	capacitance

C_{dl}	double-layer capacitance
ΔE^*	change in activation energy
ΔG^*	change in Gibbs free energy
ΔS	change in entropy
ΔZPE	change in zero-point energy
E_g	band gap energy
F	faraday's constant
I	current
λ	wavelength
P	power
Q	charge
R_{ct}	charge transfer resistance
R_s	internal resistance
S	entropy
T	temperature
V	voltage
Z_w	mass transfer impedance
η	removed fraction

Units

%	percentage
°	degree
Å	ångström (10^{-10} meters)
c mol^{-1}	coulombs per mole
cm	centimeter
cm^{-3}	per cubic centimeter
cm^2	square centimeter
°C	degrees celsius

eV	electron volt
g L^{-1}	gram per liter
Hz	hertz (frequency)
h	hour
k	boltzmann constant
kV	kilovolt (thousand volts)
kW kg^{-1}	kilowatt per kilogram (power per unit mass)
l/mm	lines per millimeter (resolution measure)
M	mol
mA cm^{-2}	milliamps per square centimeter (current density)
mbar	millibar (pressure)
meV/pixel	millielectron volt per pixel (energy resolution)
mg/L	milligrams per liter (concentration)
mF cm^{-2}	millifarads per square centimeter (capacitance)
min	minute
mL	milliliter (volume)
ms	millisecond (time)
mrad	milliradian (angle)
mV	millivolt
mV s^{-1}	millivolts per second (scan rate)
mW	milliwatt
mAh g^{-1}	watt-hour per kilogram
mW·cm^{-2}	milliwatts per square centimeter (power density)
mWh cm^{-2}	milliwatts-hour per square centimeter (energy density)
nm	nanometer
pA	picoampere
ppm	parts per million
rpm/min	revolutions per minute

sccm	standard cubic centimeters per minute (flow rate)
Torr	unit of pressure
V	volt
V/s	volts per second
W	watt
Wh kg^{-1}	watt-hours per kilogram
μF cm^{-2}	microfarads per square centimeter
μg L^{-1}	micrograms per liter
μg·h^{-1}·cm^{-2}	micrograms per hour per square centimeter
$μm^2$	square micrometer
Ω	ohm

1 Introduction

1.1 Overview

The global energy landscape is undergoing a profound transformation in the 21st century. While fossil fuels such as oil and natural gas have historically powered industrial and economic development, their continued exploitation has brought severe environmental pollution and energy security concerns[1,2]. As climate change intensifies, there is an urgent need to promote an energy revolution characterized by clean, low-carbon, safe, and efficient systems[3]. The rapid penetration of renewable resources such as solar and wind has accelerated this transition, but their inherent intermittency and fluctuation pose significant challenges to grid stability and long-term energy security[4,5]. Consequently, advanced energy storage technologies are indispensable to ensure reliable and flexible energy supply.

Among various strategies, electrochemical energy storage (EES) has emerged as one of the most promising approaches due to its ability to directly store and release clean electricity without geographical or climatic limitations[6]. Over the past decades, lithium-ion batteries (LIBs) have dominated the portable electronics and electric vehicle markets[7,8]. However, challenges such as uneven lithium resource distribution, escalating costs, limited energy density, and intrinsic safety risks restrict their large-scale deployment in grid applications[9–11]. Post-lithium chemistries, including sodium-, potassium-, and aluminum-ion batteries, have attracted attention owing to their abundance and lower cost. Yet, these systems still suffer from sluggish intercalation kinetics, structural instability, and inadequate cycling life, particularly in aqueous environments[12,13].

In this context, non-metallic charge carriers, for example ammonium ions (NH_4^+), have emerged as a promising alternative. Unlike conventional metal cations that rely on strong coordination interactions, NH_4^+ insertion is dominated by reversible hydrogen bonding, leading to fast ion diffusion and lower diffusion barriers[14,15]. These unique features endow

NH_4^+ storage with high reversibility, intrinsic safety, and environmental friendliness. Nevertheless, the field is still in its infancy and faces two critical challenges: (i) the lack of suitable electrode materials that can simultaneously ensure efficient electron/ion transport and structural stability, and (ii) the difficulty of balancing energy density and power density within a single device architecture[16].

To address these limitations, the concept of photo-electrochemical synergy has recently emerged as a transformative strategy[17–19]. Unlike traditional photocatalysis, which primarily relies on photogenerated carriers to drive surface chemical reactions, photo-assisted electrochemical storage leverages light not only as an additional energy source but also to modulate electrode–electrolyte interfacial properties[20]. Photovoltage and band bending at the semiconductor–electrolyte interface can reduce ion insertion barriers, while efficient carrier separation can suppress recombination losses[21,22], and surface photoactivation can introduce new active sites and improve electrolyte wettability[23]. Collectively, these effects enable enhancements in capacity, rate capability, and cycling stability that cannot be achieved through structural design alone. Therefore, the integration of light and electrochemistry represents not merely a supplement to existing storage technologies, but a paradigm shifts in energy utilization. Applying this concept to NH_4^+ storage is expected to establish a new class of safe, low-cost, and high-performance energy storage devices, bridging the gap between fundamental materials innovation and practical application[24].

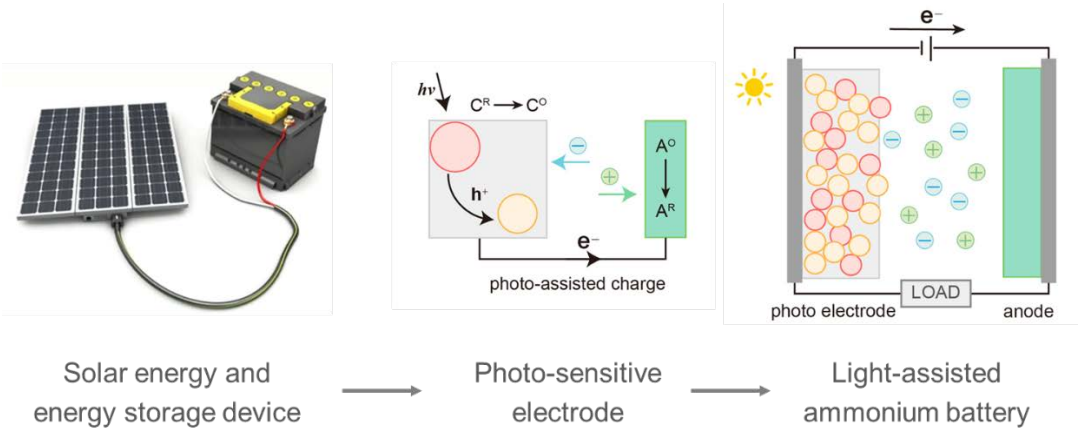


Figure 1.1 The integration of light and electrochemistry.

1.2 Energy landscape: why light-electrochemical synergy?

The rapid expansion of renewable energy has highlighted the urgent demand for flexible and efficient energy storage technologies. Traditional approaches rely exclusively on electrochemical driving forces, leaving devices constrained by the intrinsic trade-off between energy density, power density, and cycling stability.[25] This long-standing challenge motivates the exploration of new paradigms that can couple additional energy sources into charge storage processes[26,27]. Light-assisted energy storage (LAES) has emerged as a promising strategy. Early efforts primarily combined photovoltaic (PV) modules with conventional batteries or supercapacitors, in which solar energy was first converted into electricity and then stored electrochemically. Although such hybrid systems demonstrate feasibility, they suffer from additional energy losses in external connections, bulky device architectures, and limited overall efficiency. More recently, integrated concepts have been proposed, where photosensitive or semiconductor materials are directly incorporated into electrodes[28–30]. In these systems, light absorption, charge generation, and ion storage occur within the same device, thereby reducing conversion losses and simplifying the overall architecture.

The rationale for introducing light into electrochemical storage is twofold. First, illumination provides an auxiliary energy input: photogenerated carriers produce a photovoltage that can reduce charge-transfer barriers and accelerate ion intercalation/extraction. Second, light induces dynamic modulation of electrode interfaces, including carrier separation, suppression of recombination, and activation of otherwise inert surface states, all of which collectively enhance electrochemical kinetics.[31,32] As a result, LAES devices can achieve faster charging, higher capacity retention, and in certain cases even self-charging capabilities under ambient light. From a broader perspective, light-assisted storage devices represent a step toward multifunctional and integrated energy systems. Beyond conventional applications in stationary storage, these devices hold promise for portable and wearable electronics, where simultaneous energy harvesting and storage on a single lightweight platform is

particularly attractive[33,34]. Despite rapid progress, challenges remain in material compatibility, spectral utilization, and device stability, highlighting the importance of developing systematic design principles and standardized evaluation protocols. Thus, the integration of photonic energy into electrochemical storage is not merely an incremental improvement but a paradigm shift. By transforming light from an external power source into an intrinsic driving force within the electrode, photo–electrochemical synergy opens new opportunities to overcome the conventional limitations of batteries and supercapacitors and sets the stage for the design of next-generation sustainable energy devices.[35–37]

1.2.1 Current applications and research status

In recent years, light-assisted electrochemical storage has progressed from conceptual demonstrations to practical prototype systems (**Figure 1.2**)[38–48]. The earliest attempts were PV–battery coupled devices, in which photovoltaic modules were externally integrated with batteries or supercapacitors[45]. Although technically straightforward, these systems suffered from additional conversion losses and bulky architectures, limiting their efficiency and scalability. Subsequent studies advanced to photoelectrode-assisted configurations, where a photo-assisted electrode was directly integrated into the electrochemical cell. In such systems, illumination generated photovoltage and photocarriers that directly participated in charge storage, leading to measurable improvements in capacity, rate performance, and cycling stability.

More recently, research has focused on integrated two-electrode architectures, in which the same electrode simultaneously harvests light and stores ions. This compact design minimizes energy loss pathways and has been successfully applied in diverse chemistries including lithium-, sodium-, and zinc-ion systems. For example, MoS_2, WO_3, and carbon-based heterostructures have been shown to deliver higher areal capacitance and improved high-rate stability under illumination.[49–51] At the device level, photo-supercapacitors and hybrid photo-batteries have been fabricated, demonstrating proof-of-concept for

multifunctional energy platforms capable of self-charging or operation under ambient light. Overall, while the absolute energy and power densities of current devices remain below those of commercial storage technologies, the steady progression from external PV coupling to integrated photoactive electrodes highlights the growing maturity of this field. Current research efforts are increasingly directed toward optimizing material selection, heterojunction design, and device integration to improve efficiency, stability, and scalability.

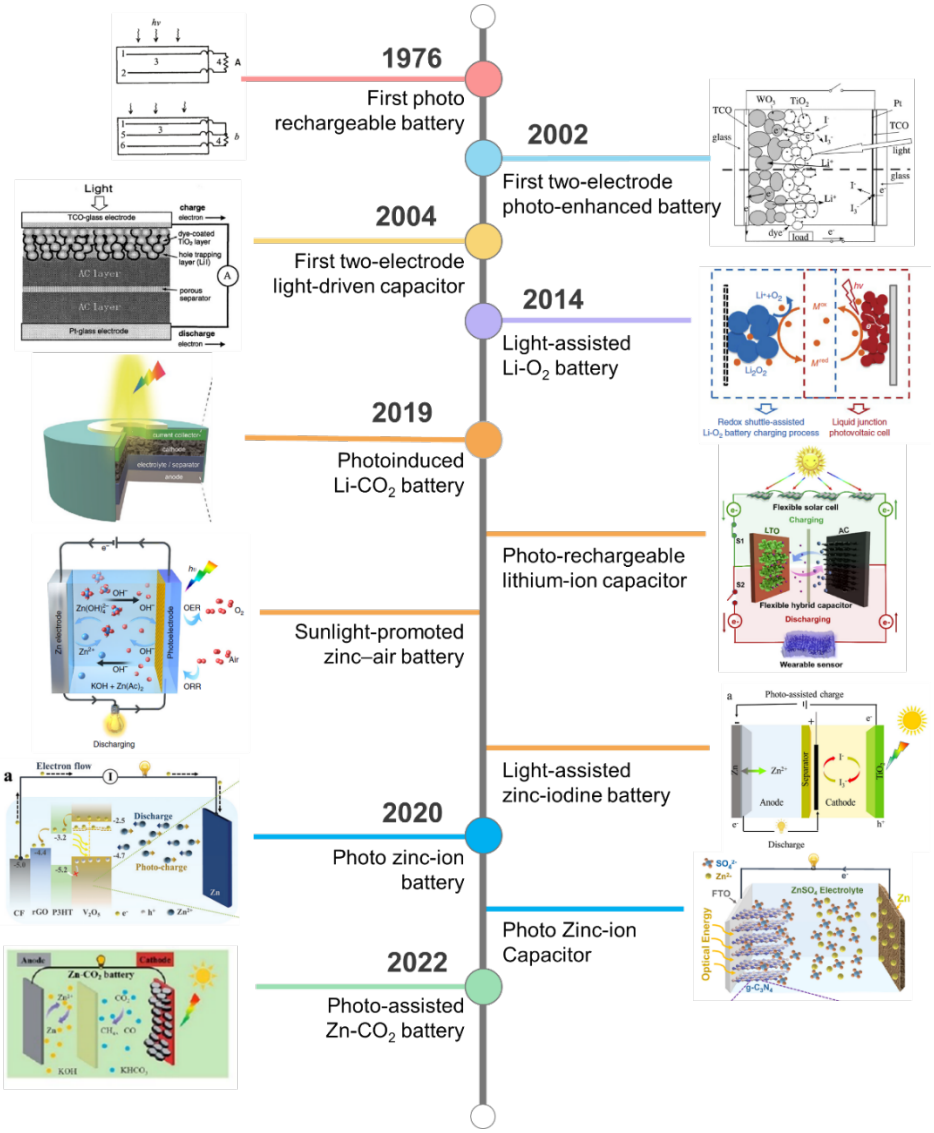


Figure 1.2 The development timeline of photo-assisted energy storage devices. Reproduced with permission.[38-48] Copyright 1976, 2014, 2019, Springer Nature. Copyright 2002, The Electrochemical Society. Copyright 2004, American Institute of

Physics. Copyright, 2019, 2020, Elsevier. Copyright, 2019, 2020, Wiley-VCH. Copyright, 2020, 2021, Royal Society of Chemistry.

1.2.2 Working principles of photo-assisted energy storage devices

In a light-assisted energy storage system, the electrode itself is designed to simultaneously function as a photo absorber and an electrochemical host, thereby directly coupling light harvesting with ion storage[52]. Upon illumination, the semiconductor electrode absorbs photons and generates electron–hole pairs. These photogenerated carriers are subsequently separated under the influence of the built-in electric field and the electrode/electrolyte interfacial band bending, as schematically shown in **Figure 1.3a**[53]. During the charging process, photogenerated electrons migrate through the external circuit toward the counter electrode, where they participate in reduction reactions, while the complementary holes remain within the illuminated electrode to drive oxidation processes. Simultaneously, charge neutrality is maintained by the migration of electrolyte ions, such as NH_4^+ or other cations, into or out of the host framework. In this manner, photons act as an auxiliary driving force that lowers the energetic barrier for ion intercalation and accelerates redox kinetics. The discharge process proceeds in reverse, where the stored chemical energy is released as electrical energy. The effect of illumination is usually seen in electrochemical analyses. For example, cyclic voltammetry curves show increased redox currents (**Figure 1.3b–c**) while galvanostatic charge–discharge profiles reveal shorter charging times and longer discharging durations (**Figure 1.3d–e**).[54,55]

These coupled mechanisms enable photo-assisted systems to simultaneously enhance capacity, improve rate capability, and extend cycle life compared with their dark conditions. The key distinction from conventional electrochemical storage arises from that light provides an additional energetic contribution directly at the electrode/electrolyte interface, rather than indirectly through external photovoltaics or third electrodes[56,57]. This conceptual evolution is reflected in the device configurations: from externally

coupled PV–battery systems (**Figure 1.3f**), to hybrid cells incorporating dedicated photoelectrodes (**Figure 1.3g**), and ultimately to compact two-electrode architectures in which a single photoactive electrode simultaneously harvests light and stores ions (**Figure 1.3h**). Such intrinsic integration of light absorption and charge storage makes the two-electrode configuration the most compact and potentially scalable design for future multifunctional energy devices.[58,59]

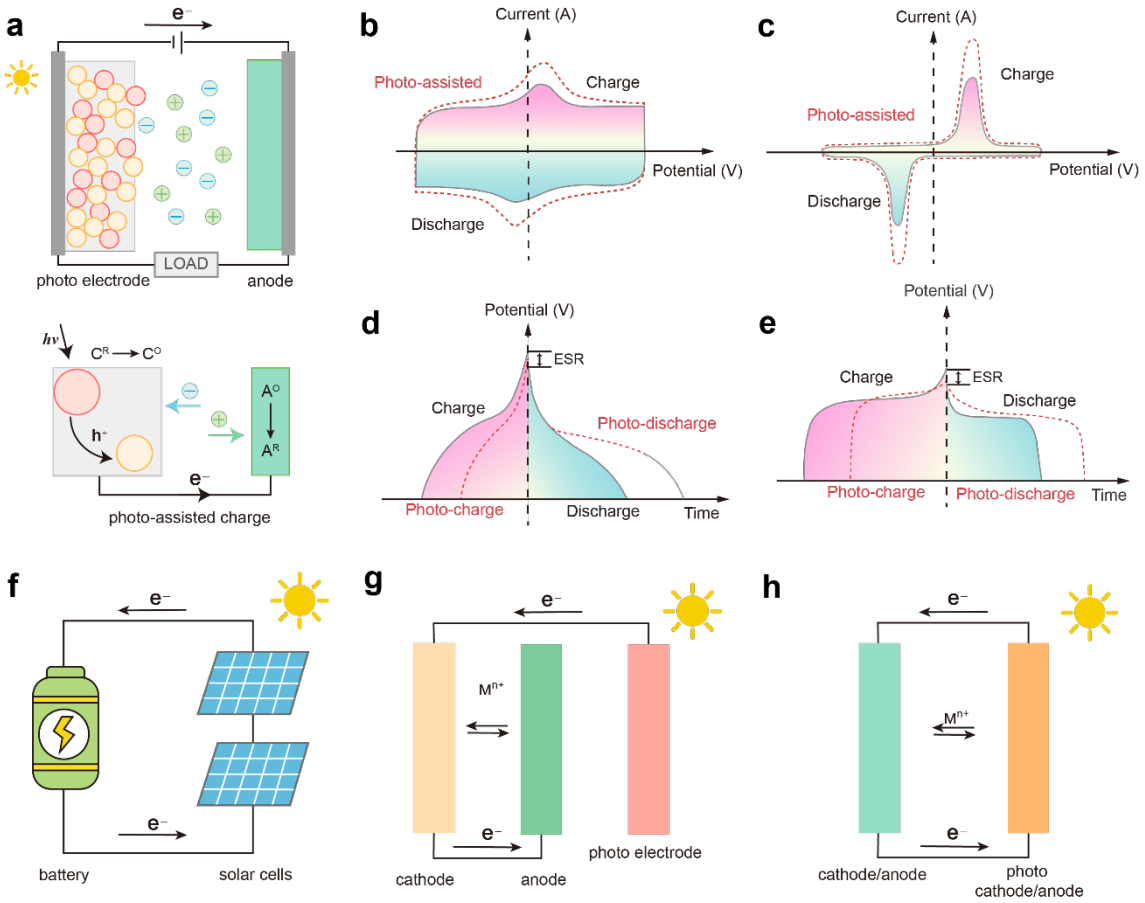


Figure 1.3 (a) Working principle of a photo-assisted energy storage device. (b,c) The CVs and GCD curves of photo-assisted devices. (f-h) The classification of photo-induced energy storage devices.[53] Copyright, 2023, Wiley-VCH.

1.3 Ammonium ion storage

In parallel with the exploration of post-lithium chemistry, NH_4^+ electrochemistry has recently emerged as a distinctive and promising branch of aqueous energy storage [60,61]. Unlike metallic cations such as Li^+, Na^+, or Zn^{2+}, whose insertion processes are governed

by strong coordination interactions with host frameworks, the charge storage behavior of NH_4^+ is dominated by reversible hydrogen bonding interactions. The tetrahedral structure of NH_4^+ enables it to form dynamic hydrogen bonds with lattice oxygen atoms in host materials, thereby facilitating fast insertion and extraction with relatively low energy barriers. This unique storage mechanism endows NH_4^+ systems with several advantages. First, the fast kinetics associated with hydrogen bonding allow for high-rate charge–discharge performance compared to multivalent metal-ion systems. Second, the insertion process generally induces less severe lattice distortion, contributing to improved cycling stability. Third, ammonium salts are abundant, inexpensive, and environmentally benign, making them particularly attractive for sustainable and safe large-scale storage applications.[62,63]

Despite these benefits, the field remains at an early stage of development. The number of electrode materials capable of reversible NH_4^+ storage is still limited, and the electron/ion coupling efficiency at electrode–electrolyte interfaces often constrain performance[63,64]. Addressing these limitations requires the rational design of electrode architectures that can fully exploit the hydrogen-bonding mechanism while overcoming intrinsic transport and interfacial bottlenecks. The following subsections introduce fundamental theoretical framework underlying NH_4^+ electrochemistry (Section 1.3.1), then reviews recent research progress and discusses the key challenges and future opportunities in this emerging field (Section 1.3.2).

1.3.1 Fundamental principles and theoretical framework

The fundamental operating principle of NH_4^+ energy storage devices is schematically illustrated in **Figure 1.4**. When a potential is applied, NH_4^+ cations migrate through the aqueous electrolyte and reversibly intercalate into the host frameworks of the cathode and anode. Unlike metallic cations, which interact with lattice sites through strong coordination bonds, the insertion of NH_4^+ is governed by hydrogen-bonding interactions between hydrogen atoms of ammonium ions and the oxygen atoms in the host lattice.

This distinct host–guest chemistry enables fast and reversible insertion/extraction with relatively low migration barriers. During the charging process, electrons flow from the cathode to the anode through the external circuit, while NH_4^+ ions migrate in the opposite direction within the electrolyte to maintain charge neutrality. The ions insert into the anode structure, forming hydrogen bonds with lattice oxygen sites. Conversely, in the discharging process, the electrons return through the external circuit, and NH_4^+ ions are released back into the electrolyte and reinserted into the cathode framework.[65] This dynamic hydrogen-bond-mediated insertion mechanism results in several distinguishing characteristics: (i) fast kinetics, as weak H-bonding lowers the energy barrier for diffusion compared with strong coordination interactions; (ii) reduced lattice distortion, since H-bonds are flexible and induce less structural strain during repeated cycling; and (iii) hybrid capacitive behavior, combining pseudocapacitive surface processes with bulk intercalation, which supports high power delivery and long cycling stability. NH_4^+ electrochemistry represents a novel storage paradigm where H-bonding rather than coordination bonding dominates ion–host interactions, conferring unique advantages in rate performance, structural stability, and environmental sustainability[66–68]. This distinctive working principle forms the scientific basis for subsequent material design strategies aimed at developing efficient NH_4^+ storage electrodes.

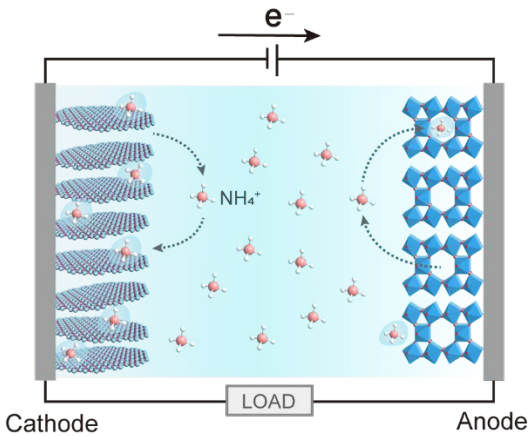


Figure 1.4 Working principle of NH_4^+ energy storage devices

1.3.2 Current research progress

Since the first demonstration of reversible NH_4^+ insertion, research on NH_4^+ energy storage devices has rapidly advanced, progressing from proof-of-concept studies to systematic investigations of diverse host materials. In the past several years, layered oxides, open-framework compounds, and carbon-based composites have been extensively explored to clarify storage mechanisms and evaluate device performance[69–71]. Central to these advances is the recognition that the storage of NH_4^+ ions is intrinsically governed by the crystal structure and dimensionality of the electrode host, which dictate ion transport pathways, storage capacity, and overall electrochemical behavior. As a result, these NH_4^+ storage materials can be systematically classified into three types according to their structural dimensionality. It helps to provide a clearer framework for the understanding of ion–host interactions and to guide the rational design of high-performance electrodes for ammonium-ion hybrid supercapacitors and batteries.

In more detail, one-dimensional materials represent a significant category of NH_4^+ storage hosts, featuring tunnel-like structures that provide direct pathways for NH_4^+ion insertion and desertion through intercalation mechanisms. These materials are characterized by tunnel channels with typical dimensions of approximately 0.50 nm × 0.50 nm framework structures that can accommodate NH_4^+ ions within the tunnels. They also possess direct ion diffusion pathways along the tunnel that enable fast ion transport kinetics. Representative materials in this category include α-MnO_2, h-MoO_3 and h-WO_3[72–74]. The NH_4^+ storage mechanism in these one-dimensional materials primarily occurs through intercalation within the tunnel structures, where the ions can move freely along the tunnel channels, leading to fast ion transport kinetics. Meanwhile, the hydrogen bonding between NH_4^+ and the framework oxygen atoms provides additional stabilization that enhances storage reversibility.

Two-dimensional layered materials constitute another important class of NH_4^+ storage hosts, offering interlayer spaces for NH_4^+ storage through mechanisms that take advantage of the flexible nature of layered structures. These materials are characterized

by layered structures with an interlayer spacing of approximately 0.57 nm × 0.96 nm, *Van der Waals* interactions between layers that allow for expansion during ion insertion, and flexible interlayer distances that can accommodate different ion sizes without significant structural damage. Representative materials include VS_2VO_x, V_2O_5, and δ-MnO_2[75–77]. In two-dimensional materials, NH_4^+ ions are intercalated into the interlayer spaces, where the layers reversibly expand to accommodate the ions, ensuring efficient transport and stable cycling.

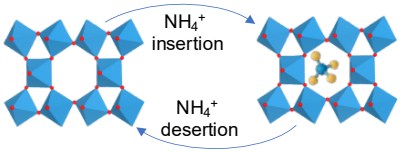
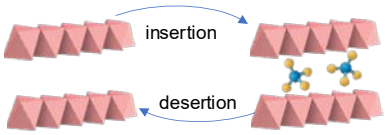
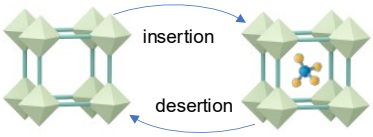
Types	Reaction mechanism	Channel type & size	Electrode materials
One dimensional		Tunnel channel Tunnels ~0.50 x 0.50 nm	α-MnO_2 h-MoO_3 h-WO_3
Two dimensional		Layered space Interlayer spacing ~0.57 x 0.96 nm	VS_2VO_x V_2O_5 δ-MnO_2
Three dimensional		Tunnel channel Tunnel ~0.32 x 0.32 nm	$Cu_3[Fe(CN)_6]_2$ $Fe_4[Fe(CN)_6]_3$ $NaFe[Fe(CN)_6]$

Figure 1.5 Classification of NH_4^+ storage materials based on structural dimensionality and corresponding storage mechanisms.

Three-dimensional framework materials provide the most complex ion storage environments, featuring interconnected tunnel networks that offer multiple pathways for NH_4^+ storage through sophisticated mechanisms combining intercalation and ion exchange processes. These materials are characterized by interconnected tunnel systems with channels of approximately 0.32 nm × 0.32 nm, framework structures that offer multiple diffusion pathways for enhanced ion transport, and high structural stability due to the three-dimensional connectivity that prevents structural collapse during cycling. $Cu_3[Fe(CN)_6]_2$, $Fe_4[Fe(CN)_6]_3$ and $NaFe[Fe(CN)_6]$ are representative materials in this category[78–80]. Three-dimensional materials store NH_4^+ ions within the framework cavities

through a combination of intercalation and ion exchange mechanisms, where the three-dimensional connectivity provides multiple pathways for ion diffusion leading to excellent rate performance, and the framework structure remains stable during cycling due to the strong covalent bonding network that maintains structural integrity.

Comparative analysis of these different storage mechanisms reveals distinct advantages and limitations for each dimensional category, with one-dimensional materials offering the fastest transport along tunnel directions but potentially suffering from channel blocking that can limit capacity. Two-dimensional materials provide good transport kinetics with flexibility for structural accommodation and generally the highest capacity due to large interlayer spaces. Three-dimensional materials exhibit excellent ion and electron transport (due to multiple pathways) and the highest structural stability (due to framework connectivity). Unfortunately, they may have smaller channel sizes that can limit the size of ions that can be accommodated. Despite significant progress in the understanding and development of NH_4^+ storage materials, several challenges still remain, including limited understanding of the exact roles of hydrogen bonding and its impact on storage kinetics, the better control over channel and layer dimensions for the optimization of NH_4^+ accommodation, the development of suitable electrolytes that can maximize the advantages of NH_4^+ storage, the improvement of long-term cycling stability (particularly for layered materials), and the enhancement of high-rate capabilities for practical applications.

1.4 Electronic structure and intercalation phenomena of tungsten oxide

1.4.1 Electronic structure of tungsten oxide

Tungsten oxide (WO_3) is a typical transition-metal oxide that has been extensively studied stemming from its rich structural versatility and semiconducting properties. WO_3 is composed of corner- or edge-sharing WO_6 octahedra, which can be arranged in different configurations when the applied temperature and synthesis conditions are varied. Multiple polymorphs including monoclinic, orthorhombic, tetragonal, and hexagonal

phases are accessible. Note that each exhibits distinct lattice symmetries and ion-diffusion pathways (**Figure 1.6**)[81,82]. This structural diversity provides a flexible platform for the reversible insertion of virous cations (e.g., H^+, Li^+, Na^+, Zn^{2+}, and NH_4^+) featuring different sizes. In other words, WO_3 is a universal intercalation host. The electronic properties of WO_3 are strongly influenced by its oxidation state chemistry. For example, tungsten can exist predominantly in the +6-oxidation state but can adopt lower oxidation states such as +5 and +4 under reduction conditions or through oxygen vacancy formation. The presence of mixed-valence tungsten states significantly alters the electronic structure of WO_3. Once additional electronic states are introduced within the bandgap, a more conductive material will be created through enhanced charge carrier density and improved electron mobility[83]. Taking oxygen vacancies as an example, they are commonly formed during synthesis or electrochemical cycling. As electron donors, they then create localized defect states that can facilitate charge transport through hopping mechanisms between adjacent tungsten sites[84]. These defect states also modify the work function and surface electronic properties, making the material more suitable for electrochemical applications in that they lower the energy barriers for charge transfer processes at the electrode/electrolyte interface.

From an electronic perspective, WO_3 is generally considered an n-type semiconductor, with a bandgap typically ranging from 2.6 to 2.8 eV. The conduction band is mainly derived from its W 5d orbitals, while its valence band is composed of O 2p states. This band alignment not only facilitates efficient electron transport but also enables visible-light absorption. In short, WO_3 can be positioned as a suitable photoactive material for photoelectrochemical processes[85,86]. Importantly, the conduction band minimum lies at an energetically favorable level relative to many redox couples in aqueous electrolytes, providing the thermodynamic driving force for electron transfer under illumination.

Amorphization of tungsten oxide leads to profound changes in its electronic structure that generally favor enhanced electrochemical activity compared to crystalline phases[87,88]. The loss of long-range order in amorphous materials generally results in a broadening of

electronic states and the creation of additional defect levels within the bandgap. Electrical conductivity is further increased through enhanced charge carrier density and modified transport mechanisms. The amorphous structure also promotes the formation of a higher concentration of oxygen vacancies and mixed-valence tungsten states, further contributing to improved electronic properties. Additionally, the increased disorder in amorphous tungsten oxide creates a more flexible electronic structure that can better accommodate the electronic changes that are associated with ion insertion and extraction processes. In conclusion they potentially lead to improved cycling stability and reversibility in electrochemical applications.

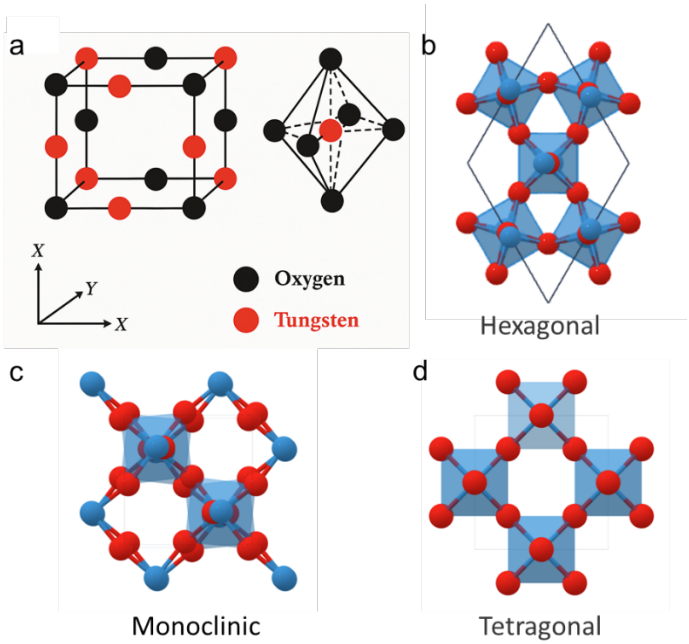


Figure 1.6 (a) Basic unit cell of WO_3. (b-d) Typical crystal structure of WO_3.

1.4.2 Ion intercalation phenomena in tungsten oxide

Tungsten oxide has recently gained increasing attention as one of the most promising inorganic hosts for NH_4^+ storage. Its structural versatility, open frameworks, and strong affinity for hydrogen bonding make it particularly suitable for accommodating NH_4^+ cations in aqueous electrolytes. In contrast to metallic cations such as Zn^{2+} or Li^+, whose insertion into WO_3 is driven by coordination interactions, NH_4^+ storage is dominated by

hydrogen bonding between the hydrogen atoms of NH_4^+ and the lattice oxygen atoms of WO_3. This unique interaction provides several intrinsic advantages: reduced lattice strain during insertion, lower migration barriers, and enhanced reversibility over long-term cycling[15]. Electrochemical studies have demonstrated that WO_3 electrodes can deliver stable capacity and high-rate performance in NH_4^+ systems. For instance, layered and nanostructured WO_3 frameworks provide one-dimensional or quasi-two-dimensional channels that enable fast NH_4^+ diffusion, while the hydrogen-bonding mechanism ensures reversible intercalation/extraction. Compared with other transition-metal oxides, WO_3 exhibits a favorable balance between capacity, cycling stability, and ionic kinetics. Therefore, it has been recognized as a versatile platform for aqueous NH_4^+ batteries and hybrid supercapacitors[14].

Monoclinic WO_3 (m-WO_3) represents the most widely investigated polymorph. The First-principles calculations and ex-situ analyses have demonstrated that NH_4^+ insertion into m-WO_3 proceeds through a three-dimensional equilibrium diffusion pathway, accompanied by the reversible reconfiguration of linear and trifurcated hydrogen bonds within the lattice. This dynamic hydrogen-bonding evolution not only reduces structural strain but also enhances ion mobility. In one report, m-WO_3 electrodes deliver capacities as high as ~150 mAh g^{-1} at low rates, retain ~48 mAh g^{-1} even at 5 A g^{-1}, and maintain >95% of their initial capacity after 5000 cycles[89]. The full NH_4^+ aqueous batteries where m-WO_3 anodes were integrated with γ-MnO_2 cathodes have achieved energy densities approaching 65 Wh kg^{-1}. They own also both practical feasibility and long-term stability.

In addition to m-WO_3, hexagonal WO_3 (h-WO_3) has recently been introduced as a superior high-rate host for ion storage[72]. Its one-dimensional tunnels, stabilized by interstitial water molecules, provide highly conductive ionic pathways that are perfect to confine NH_4^+ insertion and extraction within the channel network. This confinement minimizes structural degradation compared to layered oxides and supports rapid pseudocapacitive behavior. Strikingly, h-WO_3 delivers ~82 mAh g^{-1} at 1 A g^{-1} and retains

68% of its capacity after 200,000 cycles at an ultrahigh current of 20 A g^{-1}, establishing a new benchmark in aqueous NH_4^+ systems in terms of their cycle life.

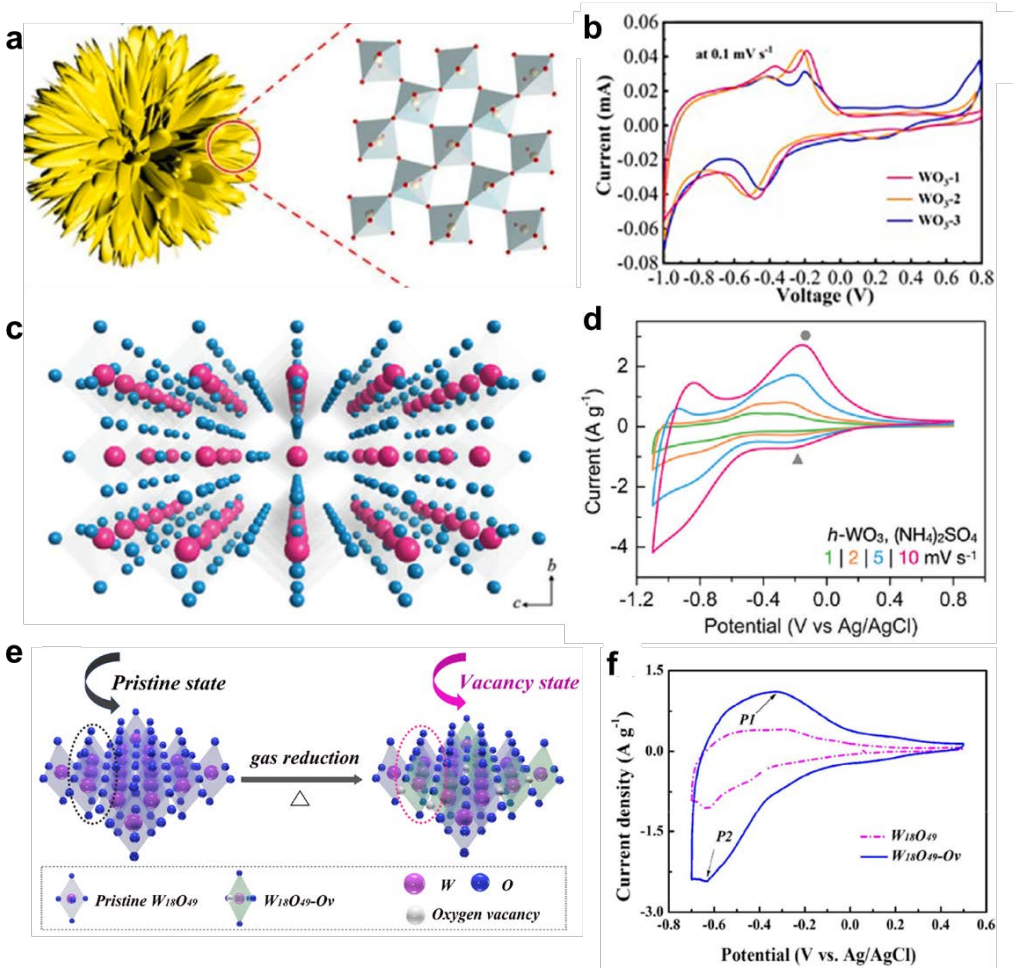


Figure 1.7 (a) Schematic illustration of m-WO_3, (b) the cyclic voltammogram of m-WO_3. (c) Schematic illustration of h-WO_3. (d) The cyclic voltammogram of h-WO_3. (e) Schematic illustration of $W_{18}O_{49}$–O_v. (f) The cyclic voltammogram of $W_{18}O_{49}$–O_v.[72,82,89] Copyright, 2022, 2023, Elsevier. Copyright, 2022, Wiley-VCH.

In parallel, oxygen vacancy engineering has been explored to overcome the intrinsic limitations of electronic conductivity and sluggish redox kinetics inside WO_3. For example, defect-rich phases such as $W_{18}O_{49}$–O_v can introduce shallow donor states that will narrow the bandgap, enhance charge transport, and provide abundant adsorption sites for NH_4^+ storage[84]. These modifications accelerate interfacial charge transfer and improve overall utilization of the WO_3 lattice, representing a versatile approach to further optimize

both rate capability and capacity retention. Collectively, these advances highlight WO_3 as a model system for the study of hydrogen-bond-driven ion storage. By leveraging structural polymorphism (hexagonal vs monoclinic) as well as defect engineering, WO_3 electrodes have achieved high capacity, remarkable cycling stability, and fast kinetics in NH_4^+ storage systems. Nevertheless, many challenges remain. For example, these WO_3 electrodes only possess limited energy density compared with Li^+ or Zn^{2+} storage systems. Their mechanistic understanding of H-bond dynamics is incomplete. The scalability of such electrode architecture needs to be addressed. These issues trigger and define the next stage of WO_3 research in AIBs. Considering that our goal is to construct light-assisted AIHSs, it is necessary to develop electrode architectures that can simultaneously facilitate ion transport and photon utilization. Composite structures, especially semiconductor heterojunctions or conductive hybrids, are expected to effectively improve charge separation and broaden light absorption, thereby paving the way for subsequent photo-assisted energy-storage systems. Therefore, the following section discusses composite design strategies focusing on heterojunctions and interfacial synergies.

1.5 Composite design: heterojunctions and synergy

As a powerful approach to enhance the optical and electrochemical properties of energy storage materials beyond what can be achieved with individual components alone, the development of composite materials has emerged through the strategic combination of different components. In more detail, composite design enables the creation of heterojunctions that can fundamentally alter charge transfer dynamics, light absorption characteristics, and improved storage mechanisms through synergistic effects[90–92]. The formation of heterojunctions between different materials is expected to create interfaces with unique electronic and optical properties. These properties arise from band alignment, charge redistribution, and the creation of built-in electric fields. These fields can facilitate charge separation and transport processes. These processes are essential for advanced energy storage applications. Some general heterojunctions are discussed below.

1.5.1 Type-II Heterojunctions

Type-II heterostructures are constructed by coupling two semiconductors with staggered band alignments.[93] Upon illumination, photogenerated electrons migrate to the lower conduction band while holes to the higher valence band. In other words, effective charge separation occurs. In some reported WO_3-based systems, TiO_2, g-C_3N_4, or carbonaceous semiconductors have been coupled. These compositions have shown extended visible-light response and reduced recombination losses[94–96]. These finally exhibit enhanced photocurrent density and faster NH_4^+ insertion kinetics compared with pristine WO_3.

1.5.2 p–n Junctions

A p–n heterojunction is formed at the interface when a n-type semiconductor is coupled with a p-type semiconductor. The equilibration of their Fermi levels induces band bending, then creates an internal electric field that drives photogenerated electrons toward the n-type and holes toward the p-type domain[97,98]. This built-in field effectively promotes carrier separation, reduces charge recombination, and lowers interfacial overpotentials. Some reported p–n junctions do exhibit improved photovoltage generation and enhanced interfacial kinetics, enabling more efficient utilization of photogenerated carriers. Such characteristics render p–n heterostructures particularly attractive for the applications where strong interfacial electric fields and efficient charge transport are required. They thus provide a general design principle for advancing photo responsive electrochemical systems.

1.5.3 Z-Scheme Systems

Differently, Z-scheme heterojunction is inspired by natural photosynthesis. It couples two photoactive semiconductors so that photogenerated electrons in one conduction band can recombine with holes in the other valence band[99]. This configuration preserves high redox potential of the remaining carriers, providing strong oxidizing and reducing abilities

simultaneously. One example is WO_3 integrated Z-scheme architecture with CdS or carbon-based photocatalysts. Such systems exhibit both broader spectral utilization and stronger driving force for surface redox reactions[100].

1.6 Outline of this thesis

Based on the above considerations, this dissertation is structured around the systematic development and further optimization of tungsten oxide-based electrode materials for AIHSs, progressing from fundamental material design to advanced composite architectures with photo-enhanced capabilities. The research follows a logical progression that addresses the key limitations of conventional electrode materials through innovative structural engineering and strategic composite formation, ultimately demonstrating the potential for next-generation energy storage devices with superior performance characteristics. This thesis thus contains 6 chapters:

Chapter 1 reviews light-assisted energy storage and motivates AIHSs. It introduces NH_4^+ storage principles, the electronic structure and intercalation behavior of WO_3, and composite strategies (Type-II, p–n, and Z-scheme) that guide later chapters; the chapter ends with the thesis outline.

Chapter 2 outlines the experimental details, including material preparation technologies (electrochemical deposition, magnetron sputtering, MWCVD, thermal CVD), fabrication of WO_3, h-WO_3, PANI, WO_3/TiO_2 and WO_3/BDD, and the full characterization toolbox (SEM/TEM, Raman, XRD, XPS, N_2 adsorption). It also specifies electrochemical and photo-electrochemical tests (CV, GCD, EIS, Mott–Schottky, LSV, i–t) as well as data/DFT methods.

Chapter 3 introduces conventional tungsten oxide electrodes that face significant challenges including poor electronic conductivity, limited ion accessibility, and insufficient cycling stability. To simultaneously address these limitations, this chapter introduces the innovative design concept that folded nanocrystalline-stacked amorphous tungsten oxide (a-WO_3) electrodes to create a hierarchical framework optimized for NH_4^+

storage. The rapid electrochemical synthesis method is detailed, along with comprehensive characterization of the structural and electrochemical properties of material. The growth mechanism is systematically investigated through parameter optimization studies, revealing the critical factors governing material morphology and performance.

Chapter 4 establishes photo-enhanced energy storage systems represent an emerging frontier that combines solar energy harvesting with electrochemical storage capabilities. Building upon the foundation established in Chapter 3, the synthesis and optimization of photo-assisted WO_3/TiO_2 composites are systematically investigated. Comprehensive photophysical and electrochemical characterization reveals the synergistic effects between the two oxide components, demonstrating enhanced light absorption, improved charge carrier dynamics, and accelerated ion transport kinetics under illumination. The chapter establishes the potential for dual-functional energy storage devices that can harvest solar energy while providing high-performance electrochemical storage capabilities.

Chapter 5 designs **t**he p-n junction materials that offer unprecedented opportunities to harness photo-generated charge carriers for enhanced electrochemical energy storage through strategic semiconductor coupling and interfacial engineering. This thesis will demonstrate how the unique electronic properties of BDD can be strategically combined with WO_3 to form WO_3/BDD that simultaneously address fundamental limitations in conductivity, light absorption, and charge separation efficiency. The formation of p-n junctions creates built-in electric fields that facilitate spatial separation of photo-generated electrons and holes. The WO_3/BDD exhibits synergistic photo-electrochemical behaviors that dramatically enhance NH_4^+ storage performance under light illumination, leading to improved capacity, accelerated kinetics, and superior cycling stability in light-assisted AIHSs.

Chapter 6 summarizes the structural engineering of a-WO_3, Type-II in WO_3/TiO_2 and p-n heterojunctions in WO_3/BDD enable photo-enhanced NH_4^+ storage, and outlines future

work on advanced operando characterization, dual-ion/multi-chemistry integration, and deeper mechanism studies of photo-enhancement.

2 Experimental

2.1 Material preparation

2.1.1 Electrochemical deposition

Electrochemical deposition is a solution-based technique that enables the formation of solid films or nanostructures on conductive substrates by applying an external potential or current. The process is generally conducted in a three-electrode configuration, consisting of a working electrode, a counter electrode, and a reference electrode, connected to a potentiostat or galvanostat for precise controls (**Figure 2.1**). When a potential is applied, charged species in the electrolyte migrate toward the oppositely charged electrode. At the working electrode, these ions undergo electron transfer reactions: cations can be reduced to their metallic or oxidized solid states, while anions may participate in complementary oxidation reactions. The reduction or oxidation process initiates the nucleation of solid nuclei on the electrode surface, which subsequently grows into a continuous film. The morphology, thickness, and crystallinity of the deposit are governed by the applied conditions such as the potential or current density, the ion concentration, the pH of the electrolyte, and the duration of deposit. The counter electrode serves as the site where charge-balancing reactions occur, thereby completing the electrical circuit, while the reference electrode provides a stable potential against which the working electrode is controlled. This configuration ensures reproducibility and accuracy in the deposition process.

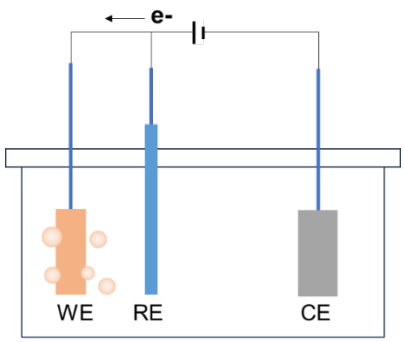


Figure 2.1 Schematic illustration of the electrochemical deposition principle using a three-electrode configuration.

2.1.2 Magnetron sputtering

Magnetron sputtering is a widely used physical vapor deposition technique that enables the formation of thin films with well-controlled composition and thickness. In this process, a target material is placed inside a vacuum chamber, and an electric field is applied between the target (cathode) and the chamber wall (anode) to ignite a plasma, typically in an argon atmosphere. Plasma generates positively charged ions, which are accelerated toward the negatively biased target surface. Through momentum transfer, these energetic ions eject atoms or clusters from the target material, which then travel through the chamber and condense on the substrate, forming a thin film (**Figure 2.2**).

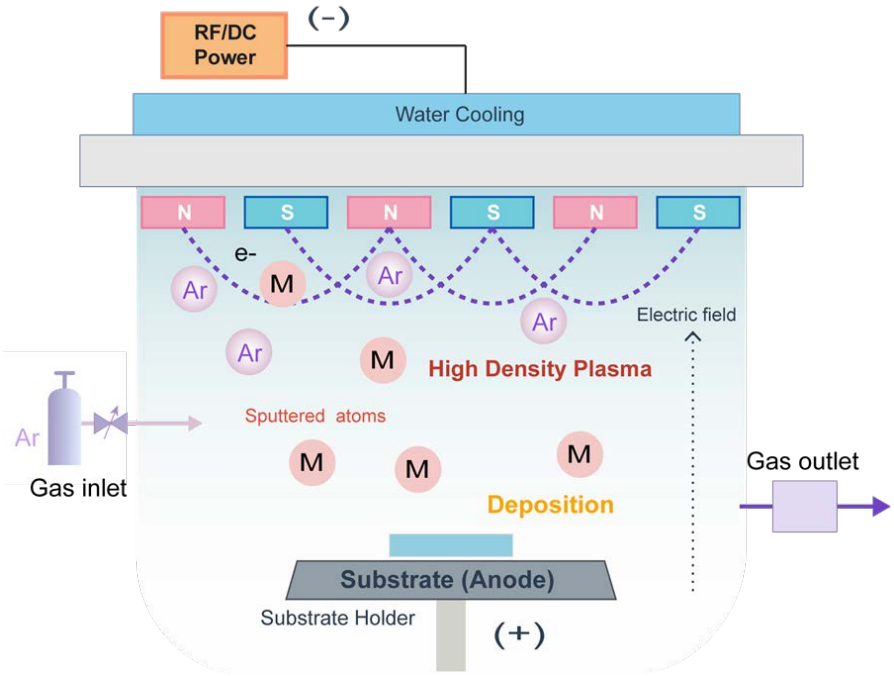


Figure 2.2 Schematic diagram of the magnet sputtering physical vapor deposition.

The incorporation of a magnetic field close to the target surface creates a closed-loop path for electrons, effectively trapping them near the target. This confinement enhances the ionization efficiency of the plasma, thereby increasing the density of energetic ions that bombard the target. As a result, the sputtering rate is improved, and the process can be operated at lower pressures while maintaining a stable discharge. The properties of as-deposited films are strongly influenced by the operating parameters, such as working pressure, sputtering power, target-to-substrate distance, and substrate temperature.

Furthermore, by introducing reactive gases such as oxygen or nitrogen into the chamber, reactive sputtering can be achieved, enabling the formation of compound films with tailored stoichiometry.

2.1.3 Microwave plasma enhanced chemical vapor deposition

Microwave assisted chemical vapor deposition (MWCVD) is a plasma-enhanced CVD technique that utilizes microwave electromagnetic radiation at 2.45 GHz or other frequencies to generate and sustain high-density plasma for precursor decomposition and further the film formation (**Figure 2.3**). The fundamental principle relies on the interaction between microwave energy and gas molecules, where the oscillating electric field of microwave radiation accelerates free electrons in the gas phase through both collisional and collision-less heating mechanisms. These energetic electrons subsequently collide with neutral precursor molecules, causing ionization, dissociation, and excitation processes that create a rich environment of reactive species including ions, radicals, and excited molecules.

The microwave energy coupling occurs through electron cyclotron resonance (ECR) or direct plasma heating, depending on the magnetic field configuration and operating conditions. In the absence of magnetic fields, electrons gain energy through collisions with the oscillating electric field, leading to avalanche ionization and plasma formation when the electron energy exceeds the ionization threshold of the gas molecules. The high-frequency nature of microwave radiation (2.45 GHz) ensures efficient energy transfer to electrons while minimizing ion heating, resulting in a non-equilibrium plasma characterized by high electron temperatures (1-10 eV) and relatively low gas temperatures.

The enhanced chemical reactivity in MWCVD arises from the high concentration of reactive species generated by electron impact processes. Precursor molecules undergo various decomposition pathways through electron impact dissociation, creating highly reactive radicals that readily participate in surface reactions on the heated substrate. The

plasma environment also provides ion bombardment effects that enhance surface mobility and promote crystalline growth, while the reduced substrate temperature requirements compared to thermal CVD result from the high chemical reactivity of plasma-generated species, enabling film deposition through pathways that are not accessible in purely thermal processes.

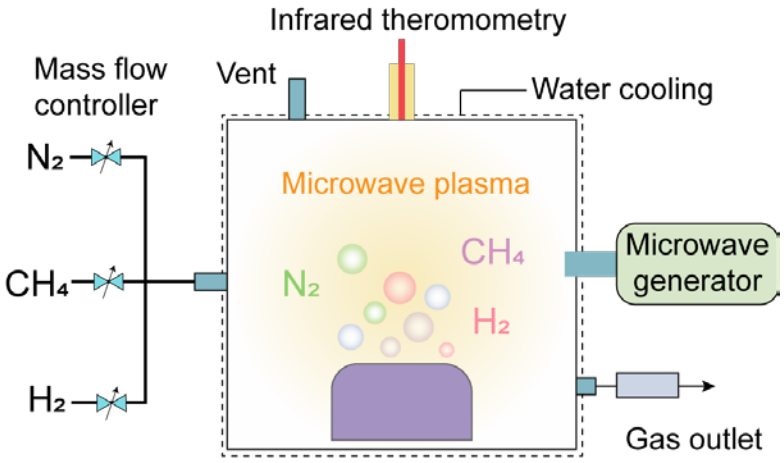


Figure 2.3 Schematic illustration of the microwave plasma chemical vapor deposition process.

2.1.4 Thermal chemical vapor deposition

Thermal chemical vapor deposition (Thermal CVD) is a classical film growth technique in which volatile precursor gases decompose or react at elevated temperatures to form a solid material on the substrate surface (**Figure 2.4**). Unlike plasma-enhanced CVD, where energetic plasma species provide activation energy, thermal CVD relies solely on external heating of the reaction chamber or the substrate to initiate and sustain the chemical reactions.

In a typical setup, precursor gases are introduced into a heated quartz tube, which is embedded within a resistively heated furnace. As the gases flow through the reaction zone, the high temperature induces decomposition into reactive intermediates. These species subsequently adsorb onto the heated substrate surface, where they undergo surface diffusion, nucleation, and chemical bonding, ultimately leading to film growth.

The process parameters—including precursor composition, gas flow rate, furnace temperature, and residence time—play a decisive role in determining the deposition rate, film thickness, crystallinity, and uniformity. Thermal CVD is widely employed due to its simplicity and capability of producing large-area coatings, although it often requires higher temperatures compared to plasma-enhanced methods.

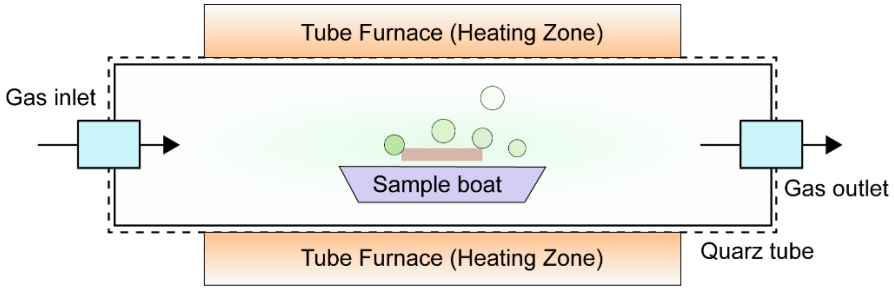


Figure 2.4 Schematic illustration of the Thermal chemical vapor deposition

2.2 Materials preparation

2.2.1 Substrate preparation

The carbon cloth (CC) was first ultrasonically cleaned in acetone for 30 mins to remove organic contaminants and manufacturing residues, followed by sequential cleaning in ethanol and deionized water for 15 min each to eliminate residual solvents and ionic impurities. After cleaning, the substrates were dried in a vacuum oven at 60 °C for 12 h to remove moisture and volatile compounds that could interfere with subsequent coating processes. All subsequent deposits were performed using pretreated substrate samples.

2.2.2 Electrochemical deposition of WO_3

The a-WO_3@CC electrodes were prepared by an electrochemical deposition method. In the frist step, 1.65 g of $Na_2WO_4 \cdot 2H_2O$ was dissolved in 50 mL of 0.5 M aqueous H_2SO_4 solution with aid of stirring. Then, 510 μL of hydrogen peroxide was added and continuous stirring was applied. In the resultant solution (Precursor solution) a constant potential of −3 V (*vs*. working electrode, WE) was applied for 1000 min with a platinum

foil as the counter electrode and the Ag/AgCl as the reference electrode. After the deposition, it was soaked in deionized water for 2 h. Finally, the *a*-WO_3 electrode was naturally dried in air.

To obtain the optimized samples, systematic variations in deposition parameters were performed, including the concentration of H_2O_2, the applied potential, and the deposition time. These adjustments allowed us to identify the most favorable conditions for achieving uniform film morphology and enhanced electrochemical performance.

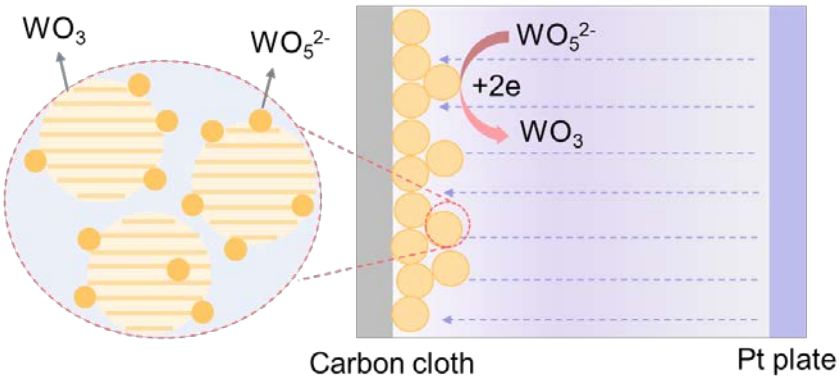


Figure 2.5 The schematic illustration shows the process of electrochemical deposition of WO_3.

2.2.3 Synthesis of h-WO_3 electrodes

The h-WO_3 electrodes were prepared by use of a hydrothermal method. Initially, 100 mL of 0.125 M sodium tungstate solution was prepared by dissolving 4.125 g of $Na_2WO_4 \cdot 2H_2O$ into 100 mL deionized water, where 3 M HCl solution was subsequently added and continuous stirring was employed until the pH value of the solution reached about 1 or untill the solution became pale yellow. After that, 0.025 M $H_2C_2O_4$ was added and the solution was stirred for 10 min and then fixed up to 250 mL in a 250-mL volumetric flask. This was a precursor solution.

Finally, 30 mL of the precursor solution was transferred where 1.5 g of ammonium sulphate was added. In a water bath the resultant solution was stirred for 2 h at 60 ℃. After repeating such a process for seveal times, the hydro-thermal reaction of this solution

was conducted in an autoclave at 180 ℃ for 16 h. After the natural cooling down of the autoclave, the product was taken out and sequentially washed with ethanol and deionised water. After its drying in an oven at 60 °C for 1 h, the product was placed in a muffle furnace, ventilated with air and sintered at 450 °C for 1 h. The final product was obtained.

2.2.4 Synthesis of PANI electrodes

The CC was firstly immersed in an aqueous solution of 10 mL 1 M HCl and 1 mL aniline (ANI) for 12 h. It was then removed and placed in a water glass, followed by the addition of a certain amount of ammonium persulfate (APS). Polymerisation was carried out at 0 °C for 2 h. The PANI electrode was then obtained, rinsed three times using deionised water and dried in a vacuum oven at 50 °C[101].

2.2.5 Preparation of WO_3/TiO_2 Composites

Construction of TiO_2 Layer

The titanium deposition was carried out using DC magnetron sputtering in a high-vacuum chamber equipped with a pure titanium target (99.99% purity, 4-inch diameter). The sputtering chamber was evacuated using a turbo-molecular pump backed by a mechanical roughing pump. The chamber was continuously pumped until a base pressure of 5×10^{-6} Torr was achieved, as measured by an ion gauge. Following successful vacuum evacuation, the CC substrates underwent controlled preheating to optimize the nucleation and growth of the titanium film. The substrate holder was gradually heated to 300 °C at a rate of 30 °C min^{-1} to minimize thermal stress and prevent rapid outgassing that can degrade vacuum conditions.

Prior to actual titanium deposition, the titanium target underwent thorough cleaning through a pre-sputtering process designed to remove surface oxides and contaminants. High-purity argon gas (99.999%) was introduced into the chamber, establishing a working pressure of 0.015 Torr. The RF power supply gradually increased to 350 W while

a protective shutter was positioned between the target and substrate during this cleaning phase. The pre-sputtering process was continued for 10 mins to ensure complete removal of surface contaminants, with visual monitoring of the plasma color and stability serving as indicators of cleaning effectiveness. Following successful target cleaning, the actual titanium deposition commenced with the protective shutter retracted to expose the substrate to the sputtered titanium flux. The sputtering power was adjusted to 300 W to provide optimal deposition rate while maintaining stable plasma conditions. The argon working pressure was maintained at 15 sccm throughout the deposition process. The deposition process was conducted for 120 mins to achieve a target titanium film thickness of approximately 300 nm.

Table 2.1 Parameters for the physical vapor deposition (PVD) sputtering of Ti on CC

Parameter	Value
Background pressure / torr	5×10^{-6}
Working pressure / torr	0.015
RF power / W	300
Ar flow rate / sscm	15
Heater power / V	50
sputtering time / min	120
Substrate temperature / °C	300

After titanium deposition, the samples were carefully transferred to a tube furnace for thermal oxidation in air at 600 °C. The temperature was ramped at a rate of 5 °C min^{-1}. Once 600 °C was reached, it was held for 1 h to ensure complete oxidation of metallic titanium and the formation of a well-crystallized anatase TiO_2 phase. Following the isothermal treatment, the samples were naturally cooled to room temperature.

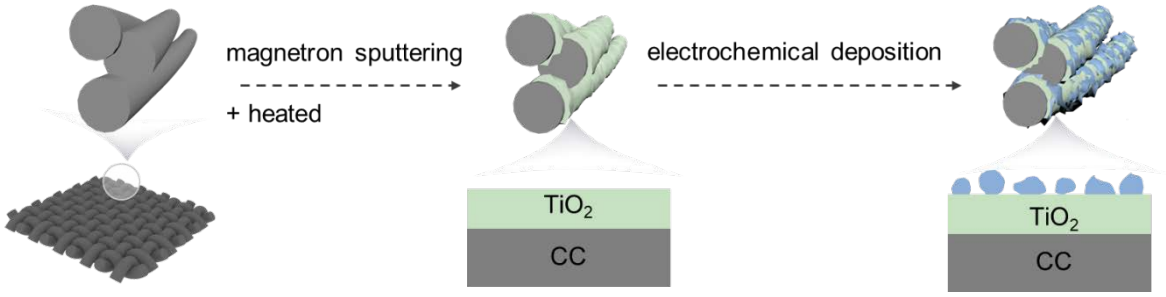


Figure 2.6 Schematic illustration of the fabrication process: (left) bare carbon cloth, (middle) TiO_2 layer deposited on carbon cloth (~300 nm), and (right) subsequent WO_3 deposition forming the WO_3/TiO_2 composites.

Composite fabrication process

On this TiO_2@CC substrate, WO_3 deposition was further coated by electrochemical deposition, leading to the final composite electrode.

2.2.6 Preparation of WO_3/BDD Composites

Preparation for BDD

A titanium interlayer was subsequently deposited onto the CC using a radio frequency (RF, 13.56 MHz) magnetron sputtering system. A high-purity titanium target (99.995%, ZhongNuo Advanced Material (Beijing) Technology Co., Ltd., Φ101.6 × 6 mm) was employed, with pre-sputtering conducted for 10 min under a closed shutter to eliminate surface contamination. The Ti deposition was carried out in an Ar atmosphere for 1 min. The detailed sputtering conditions, including background pressure, working pressure, RF power, Ar flow rate, heater power, sputtering time, and substrate temperature, are summarized in **Table 2.2**.

Table 2.2 Parameters for the PVD sputtering of Ti on BDD

Parameter	Value
Background pressure /torr	$1.2\sim2.3\times10^{-5}$
Working pressure /torr	0.008
RF power / W	200
Ar flow rate / sscm	20
Heater power / v	50
sputtering time / min	60
Substrate temperature / °C	400

Subsequently, BDD films were deposited on the Ti-coated CC substrates in a MWCVD reactor. Before deposition, the substrates were immersed in ethanol for 45 min, followed by seeding in a nanodiamond suspension (1 g L^{-1} in water) under ultrasonication for 90 min. To investigate the influence of substrate temperature, three growth temperatures were employed, and the corresponding BDD-coated carbon cloths were denoted as BDD. The deposition parameters, including chamber pressure, working pressure, H_2/CH_4/trimethyl borane (TMB) gas flow rates, microwave power, deposition time, and substrate temperature, are provided in **Table 2.3**.

Finally, the as-grown BDD samples were thermally treated in air at 450 °C for 2 h. This post-treatment step effectively reduced the residual sp^2-carbon content and introduced oxygen-containing functional groups, thereby improving surface hydrophilicity[102].

Table 2.3 Growth parameters of boron-doped diamond sample

Parameter	Value
Power / W	1000
Working pressure / W	30
H_2 flow rate / sscm	400
CH_4 flow rate / sscm	4.0
TMB flow rate / sscm	5.0
Deposition time / min	360
Substrate temperature / °C	823-853

Composite fabrication process

On this BDD substrate, WO_3 deposition was further coated by means of electrochemical deposition. In this way, the final composite electrode was constructed.

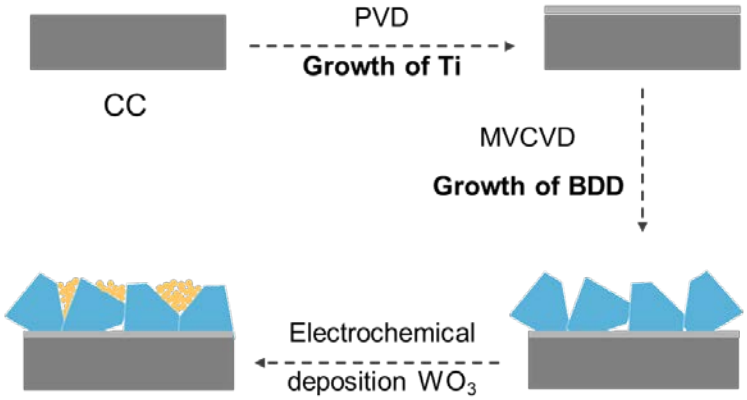


Figure 2.7 Schematic illustration of the fabrication process WO_3/BDD.

2.3 Material Characterization

2.3.1 Scanning electron microscopy

Scanning electron microscopy (SEM) was mainly employed to observe and analyze the microscopic morphology of prepared materials and to determine their dimensions. Equipped with an energy-dispersive spectrometer (EDS), it can also provide preliminary information about the elemental distribution and content. In SEM, a focused high-energy electron beam interacts with the surface of a solid sample to generate various signals. Electrons emitted from the electron gun are converted into a fine beam by a series of electromagnetic lenses. Under an applied accelerating voltage, this electron beam scans the sample surface and excites secondary electrons, which are collected by a detector and subsequently converted into light signals by a scintillator. The resulting signal corresponds to the scanned electron beam position, thus forming an SEM image. In this work, a field-emission scanning electron microscope (FE-SEM, Zeiss Ultra55, Germany) equipped with an energy-dispersive spectrometer was used.

2.3.2 Transmission electron microscope

Transmission electron microscope (TEM) was employed to observe and analyze the fine structure of as-grown samples. By combining lattice fringes and electron diffraction patterns, it also provided information for identifying the crystal structure of these materials within selected areas. To record TEM images, an accelerated and focused electron beam is transmitted through an ultrathin specimen, where electrons are scattered by collisions with atoms in the sample. The scattering angles depend on factors such as sample density and thickness, resulting in contrast variations that form bright and dark regions in the image. After magnification and focusing by electromagnetic lenses, the transmitted signals are recorded on an imaging device to produce high-resolution micrographs.

In this work, a field-emission transmission electron microscope (TEM, Tecnai G2 F20, FEI, USA) was used. The preparation of TEM specimens was carried out as follows: the synthesized films were gently scraped from the substrate with a razor blade, dispersed in ethanol, and ultrasonicated for 1–10 mins. A droplet of the resulting suspension was then placed onto a copper grid using a micropipette and dried prior to further observation.

2.3.3 Raman spectroscopy

Raman spectroscopy is a rapid and convenient technique to probe the molecular structure of samples, and thus it has been widely applied in the structural analysis of carbon-based materials. By examining the spectral bands arising from nonpolar groups or skeletal vibrations of symmetric molecules, Raman spectroscopy allows identification of chemical species, characteristic structural features, or functional groups. It serves as a complementary method to infrared absorption spectroscopy. The Raman shift, along with the intensity and line shape of Raman peaks, provides important information about chemical bonds and functional groups. In addition, the polarization characteristics of Raman signals can be used to distinguish molecular isomers. The sharpness and relative intensity of characteristic peaks further enable the evaluation of structural defects, crystallinity, and bonding states of the sample.

In this thesis, Raman spectra of the investigated films were recorded using a custom-built Raman microscope based on an inverted microscope (Nikon TE300) equipped with Nikon objective lenses and optical filters from AHF Analysentechnik. A 532 nm laser (Coherent Compass 315M-100, 100 mW output power) was employed as the excitation source. The scattered light was dispersed by a monochromator (Jobin Yvon TRIAX 320, equipped with a 1200 l/mm grating) and detected using a spectroscopic back-illuminated EMCCD camera (Oxford Instruments Andor, Newton EMCCD DU970P).

2.3.4 X-ray diffraction

X-ray diffraction (XRD) is one of the most powerful techniques for the study of crystal structures. It is particularly suitable for phase analysis of crystalline materials. When an X-ray is incident on a crystalline specimen, the electrons within the atoms are forced into oscillation and emit scattered waves. Due to the periodic arrangement of atoms in the lattice, these scattered waves interfere constructively, producing diffraction patterns that are characteristic of the crystal structure. Different crystal structures yield distinct diffraction patterns, which can be analyzed to determine the internal atomic arrangement of the material.

In this work, the XRD pattens of the films were recorded using an X-ray diffractometer (3000 PTS, GE Inspection Technologies GmbH). The measurements were carried out with Cu Kα radiation (λ = 1.5418 Å) at an operating voltage of 40 kV and a current of 40 mA. The diffraction patterns were collected over a 2θ range of 20 – 80° with a step size of 0.013°.

2.4 Surface chemistry analysis

2.4.1 X-ray photoelectron spectroscopy

X-ray photoelectron spectroscopy (XPS) is a surface-sensitive analytical technique that provides information about the elemental composition, chemical states, and electronic environments of atoms within the top few nanometers of a material. The method is based on the photoelectric effect: when a sample surface is irradiated with a monochromatic X-ray, core-level electrons are ejected from atoms. By measuring the kinetic energy of these photoelectrons, their binding energy can be determined, which is characteristic of specific elements and sensitive to their oxidation states and bonding environments.

In this work, XPS measurements were carried out using S-probe ESCA SSX-100 spectrometer (Surface Science Instruments, USA). The spectra were recorded with a monochromatic Al Kα X-ray source (hν = 1486.6 eV). Charge neutralization was applied

to minimize charging effects during measurement. The shown binding energies in the thesis were calibrated against the C 1s peak at 284.8 eV.

2.4.2 N_2 adsorption and desorption

For porous materials, surface area and pore size distribution are two critical indicators reflecting their structural characteristics. Gas adsorption is the most used technique to determine the specific surface area and pore size distribution of a porous material. Nitrogen, argon, and carbon dioxide are the typical adsorbates. At a constant temperature, only a limited amount of gas can be adsorbed on the solid surface under a given adsorbate pressure. Therefore, by measuring the adsorption amount at a series of relative pressures, an adsorption isotherm can be obtained. The shape of the adsorption isotherm provides valuable information about the surface structure of the material as well as its interaction with the adsorbate. Based on appropriate mathematical models, the specific surface area and pore size distribution of the material can be further calculated.

The specific surface area and pore size distribution of the prepared samples in this thesis were characterized by N_2 adsorption–desorption measurements at 77 K using an Anton Paar NOVA 300e surface area and porosity analyzer. The Brunauer–Emmett–Teller (BET) model was applied to calculate the specific surface area of the studied porous materials, while the Barrett–Joyner–Halenda (BJH) method was used to determine their pore size distribution.

2.5 Electrochemical measurements

In this thesis, electrochemical techniques including cyclic voltammetry (CV), electrochemical impedance spectroscopy (EIS), linear sweep voltammetry (LSV), amperometry (*i–t* curves), galvanostatic charge–discharge (GCD), and Mott–Schottky analysis were performed using a CHI660E workstation (Shanghai Chenhua Inc., China) and a Princeton Applied Research electrochemical workstation (Princeton, USA). These

electrochemical measurements were employed to investigate the electrochemical performances of WO_3, TiO_2/WO_3, and BDD/WO_3 electrodes.

The electrochemical workstation integrates a potentiostat, a current–voltage converter, and a data acquisition system, enabling precise control and recording of experimental parameters. A conventional three-electrode electrochemical cell was used, consisting of a working electrode (the investigated material), a platinum foil counter electrode, and an Ag/AgCl reference electrode, immersed in the electrolyte solution. In this configuration, the working electrode serves as the site of electrochemical reactions, the counter electrode provides current balance, and the reference electrode maintains a stable reference potential. The electrolyte ensures ionic conductivity between electrodes and sustains the redox processes during the measurements.

2.5.1 Cyclic voltammetry

Cyclic voltammetry is a versatile technique that can be used to evaluate the reversibility of electrode reactions and to gain insights into phenomena such as the formation of intermediate species, interfacial adsorption, and the generation of new phases during electrochemical processes. In this method, within the potential range where redox reactions occur, the electrode potential is controlled and swept linearly at various scan rates in a triangular waveform, either once or repeatedly, while recording the resulting current response. The obtained current–potential relationship constitutes the cyclic voltammogram. In this thesis, CV measurements were primarily employed to characterize the pseudocapacitive and electric double-layer capacitance behaviors of NH_4^+ storage devices, to assess the reversibility of the associated electrochemical reactions, and to analyze phenomena such as ion intercalation and surface adsorption.

2.5.2 Galvanostatic charge-discharge

The galvanostatic charge–discharge (GCD) technique is one of the most fundamental methods to evaluate the energy storage performance of electrode materials. In this method, a constant current is applied to the working electrode while the corresponding potential variation is recorded as a function of the operating time. The obtained charge–discharge curves provide direct information on the capacity or capacitance, Coulombic efficiency, and cycling stability of the electrode. Ideally, an electrode with purely capacitive behavior exhibits a symmetric triangular profile, whereas deviations from linearity or symmetry indicate the involvement of faradaic redox reactions, polarization effects, or resistive losses.

In this thesis, GCD measurements were employed to characterize the charge storage capability of NH_4^+ storage devices. The slope of the potential–time curve was used to calculate the specific capacitance, while the degree of symmetry between charge and discharge branches was analyzed to evaluate the reversibility and stability of the electrochemical processes.

2.5.3 Electrochemical impedance spectroscopy

Electrochemical impedance spectroscopy (EIS) characterizes the combined resistive and capacitive response of an electrode system to an applied alternating current (AC) signal. It is primarily used to study electrode kinetics and interfacial phenomena. By fitting the impedance spectra, parameters such as ohmic resistance, charge-transfer resistance, diffusion resistance, and double-layer capacitance can be extracted. As shown in Figure 2-4, R_s and R_p represent the ohmic resistance and charge-transfer resistance, respectively. The ohmic resistance originates from the electrolyte resistance, the contact resistance between the electrode material and electrolyte, and the intrinsic resistance of the electrode material. The ion diffusion resistance is described by the Warburg impedance, which is identified from the 45° (or near 45°) line in the mid-frequency region, where the intercept with the real axis corresponds to the diffusion resistance. In addition, for electrodes

exhibiting ideal capacitive behavior, the low-frequency region of the Nyquist plot presents a nearly vertical line with respect to the real axis.

In this thesis, EIS measurements were carried out in the frequency range of 10^{-2} – 10^{5} Hz with a potential amplitude of 5 mV. This technique was employed to analyze the impedance characteristics of the main steps in the electrode reactions of NH_4^+ storage devices, as well as to evaluate the relaxation times of the electrode materials during polarization processes.

2.5.4 Mott–Schottky analysis

Mott–Schottky analysis is a widely used electrochemical method to probe the photoelectronic of electrode materials. It is based on measuring the capacitance of the electrode–electrolyte interface as a function of applied potential. By plotting the reciprocal squared capacitance ($1/C^2$) against the applied potential, information such as the flat-band potential, charge carrier density, and semiconductor type (n-type or p-type) can be obtained. The slope of the Mott–Schottky plot is directly related to the doping density, while the intercept provides the flat-band potential, which is crucial for understanding the band alignment at the electrode–electrolyte interface.

In this thesis, Mott–Schottky analysis was employed to investigate the semiconductor characteristics of WO_3, WO_3/TiO_2, and WO_3/BDD electrodes. These measurements provided insights into the electronic properties, band structure, and carrier density of these electrodes, which are essential for correlating their electrochemical performance with intrinsic electronic conductivity and photoelectrochemical behavior.

2.5.5 Linear sweep voltammetry

Linear sweep voltammetry is a potential-controlled technique in which the electrode potential is swept linearly with time in a single direction while monitoring the resulting current response. Unlike cyclic voltammetry, the potential is not reversed, making LSV

particularly suitable for analyzing the onset of electrochemical reactions and evaluating the kinetics of electrode processes. The resulting current–potential curve reflects the threshold potential at which electrochemical reactions are initiated, as well as the magnitude of current associated with reaction rates.

In this thesis, LSV measurements were mainly employed to investigate the electrochemical deposition processes. By monitoring the current response as a function of applied potential, the onset potential of electrode reactions can be identified, thereby clarifying the specific point at which the deposition occurs. This enables a better understanding of the underlying reaction mechanisms during the electrodeposition of WO_3-based and composite films.

2.5.6 Amperometry (*i–t* curves)

Amperometry, or current–time (*i–t*) measurement, is an electrochemical method in which the potential of a working electrode is held at a constant value while the resulting current is continuously monitored as a function of time. Its principle lies in the fact that the current response directly reflects the electrochemical processes occurring at the electrode surface, such as charge transfer, ion diffusion, and interfacial reactions. The time-dependent current evolution provides valuable insights into the kinetics of these processes, including transient responses, adsorption/desorption phenomena, and steady-state behavior.

In this thesis, *i–t* measurements were conducted under alternating light on/off conditions to investigate the photoelectrochemical response of WO_3, WO_3/TiO_2, and WO_3/BDD electrodes. When illuminated, photogenerated charge carriers contribute to an additional current, while turning off the light leads to a rapid decay as recombination or surface relaxation dominates. By analyzing the rise and decay dynamics of the photocurrent, several parameters were evaluated covering charge carrier generation efficiency, separation, and recombination rates. Furthermore, the magnitude and stability of the photocurrent response served as indicators of the electrodes' capability to sustain photo-assisted ion storage processes.

2.6 Photo-assisted electrochemical measurements

The ultimate test for a photoelectrochemical device or a photoelectrode was performed under light irradiation at a density of 1 mW cm^{-2}. Light source is known to be a key component of a photoelectrochemical measurement setup. The light source used in this thesis is a 150 W Xenon lamp coupled with a monochromator (MSH-300, LOT-Quantum Design GmbH), which was used to transmit a mechanically selectable narrow band of wavelengths. An optical lens was used to properly focus the light on the samples. The potential applied to the samples was again controlled by a CHI 660E electrochemical analyzer, which also measures the current.

The current voltage measurement is the most important technique to determine the photoelectrochemical performance of a photoelectrode. The information about the dark current and photocurrent density as a function of applied potential can be obtained from such measurements. The photocurrent can be measured under different initial voltages or while sweeping the potential at a constant scan rate. The current voltage measurement can be conducted in dark, under constant illumination, or by switching the illumination on and off at a fixed frequency. In this thesis, CV, EIS, LSV and amperometry (*i-t* curves) were employed to analyze the photoelectrochemical performances of a WO_3/TiO_2 and WO_3/BDD composite photoelectrode.

2.7 Calculations Section

The areal capacitances (C, mF cm^{-2}) of as-constructed supercapacitors were calculated based on the GCD curves, according to the following equation (1):

$$C_S = \frac{I \times \Delta t}{S \times \Delta V} \qquad (1)$$

where S (cm^2) is the area of the electrode. I (A), Δt (s), and ΔV (V) are the discharge current, discharge time, and potential window, respectively.

The areal energy densities (E, mWh cm^{-2}) and power densities (P, mW cm^{-2}) were respectively calculated from equations (2) and (3):

$$E = \frac{C_s \Delta V^2}{2\times 3600} \quad (2)$$

$$P = \frac{E\times 3600}{\Delta t} \quad (3)$$

where ΔV is the discharge voltage range (V) and Δt is the discharge time (s).

2.8 Density functional theory (DFT) calculations

The DFT calculations were carried out using a hybrid Gaussian/Plane-Wave scheme (GPW)-based method CP2K code (http://www.cp2k.org) with the Quickstep module.[103] The core electrons and nuclei were represented with the GTH-PBE pseudopotential. The wave functions were expanded in optimized double-ζ Gaussian basis sets, and the plane waves were expanded with a cutoff energy of 400 Rydberg. The vacuum layer was set to 20 Å to avoid the interaction between the slabs. For geometry optimization, the total energy converge was below 1.0 × 10^{-6} in inner Self-Consistent Field steps and the force converge was less than 4.5×10^{-4}. The *k*-point was settled with 3 × 3 ×1. The projected density of states *(pDOS*) of each atom was analyzed and illustrated by the *Multiwfn*[*] and *Vesta* software. The calculation of NH_4^+ adsorption energy was conducted according to the equation of

$E_{ads} = E_{NH_4/slab} - E_{slab} - E_{NH_4}$, where $E_{NH_4/slab}$, E_{slab} and E_{NH_4} are the total energies of NH_4^+ ion on the WO_3 electrode, WO_3 electrode and NH_4^+ ion, respectively.

3 WO_3 materials for ammonium-ion hybrid supercapacitor

Ammonium-ion hybrid supercapacitors (AIHSs) have attracted considerable attention in that they feature unique advantages, including the abundance and low cost of ammonium salts, the non-toxic nature of NH_4^+ ions, and the distinctive hydrogen bonding characteristics that can facilitate rapid ion transport[104,105]. However, the practical implementation of AIHSs faces several critical challenges, particularly in the development of suitable electrode materials that can efficiently accommodate NH_4^+ ions and in the meantime maintain structural stability and high electrochemical performance.

Tungsten oxide (WO_3) has emerged as a promising candidate for NH_4^+ storage, thanks to its layered crystal structure, multiple oxidation states, and inherent redox activity. The tunnel-like framework of WO_3 provides potential pathways for ion intercalation, while its multiple tungsten valence states (W^{6+}, W^{5+}, W^{4+}) enable pseudocapacitive charge storage mechanisms[106,107]. However, conventional crystalline WO_3 suffers from several limitations that hinder its practical application: (1) poor electronic conductivity due to the wide bandgap of the material, (2) limited ion accessibility within the rigid crystalline framework, (3) structural instability during repeated charge-discharge cycles, and (4) sluggish ion diffusion kinetics that restrict high-rate performance[108,109].

To address these fundamental challenges, this chapter presents a comprehensive investigation of a novel electrode design strategy based on folded nanocrystalline-stacked amorphous tungsten oxide (a-WO_3). The core innovation lies in the rational engineering of the material's microstructure *via* controlled amorphization and nanocrystalline fragmentation.[110–112] This process creates a hierarchical architecture that combines the advantages of amorphous and crystalline phases.[113] This approach aims to: (1) enhance electronic conductivity through the introduction of oxygen vacancies and defect states[114,115], (2) improve ion accessibility via the creation of abundant grain boundaries and porous networks[116,117], (3) provide mechanical flexibility to accommodate volumetric changes during cycling, and (4) promote fast surface-dominated charge storage mechanisms[118].

This chapter provides a systematic understanding of the material design, synthesis, characterization, and applications of the folded nanocrystalline-stacked a-WO_3 electrodes. Beginning with the design principles and synthesis strategy, this chapter then explores the growth mechanisms underlying the formation of this unique architecture. Subsequently, detailed structural, chemical, and electrochemical characterizations are presented to elucidate the relationship between material properties and NH_4^+ storage performance. The related storage mechanism has been investigated through both experimental techniques and theoretical calculations where insights into the ion transport and charge storage processes have been shed. Finally, the practical applicability of the developed electrode is demonstrated through the construction and testing of a full AIHS device.

3.1 Design of folded nanocrystalline-stacked WO_3 structure

Crystalline tungsten oxide has been widely investigated for electrochemical applications due to its redox activity and tunnel structures. It however suffers from low conductivity, poor cycling tolerance, and limited NH_4^+ accessibility when used in its bulk form. To address these limitations, a novel folded nanocrystalline-stacked architecture is introduced on base of a-WO_3. It is rationally engineered to enhance ion and electron transport, provide mechanical flexibility, and promote high-rate reversible NH_4^+ storage. The design concept is rooted in the principle of nano structural fragmentation combined with controlled amorphization. For example, the proposed architecture consists of nano crystallites (~5 nm) loosely assembled within an amorphous matrix, forming a hierarchical, porous, and grain boundary-rich framework. Such a design is expected to reduce the effective diffusion length for NH_4^+ ions, expose many electrochemically active sites, and accommodate volumetric changes during cycling. Moreover, the presence of a high concentration of oxygen vacancies and surface oxygen-containing functional groups can further facilitate NH_4^+ adsorption and improve charge transfer kinetics at the electrode/electrolyte interface.

To realize this architecture, a rapid electrochemical deposition strategy was developed. Tungsten oxide was directly deposited on conductive CC by applying a cathodic potential of −2.5 V (*vs*. the working electrode) for 1000 s in a precursor solution. The high overpotential promotes rapid nucleation and partial reduction of tungstate species, leading to the formation of a hybrid material with disordered and crystalline domains WO_3 (**Figure 3.1a-c**). In contrast, a hydrothermally synthesized hexagonal WO_3 (h-WO_3) sample, used as a control experiment, yielded dense, well-ordered crystal grains with fewer defect sites and less surface area (**Figure 3.1c**). This highlights the advantages of the electrochemical method in producing structurally open, defect-rich WO_3 films.

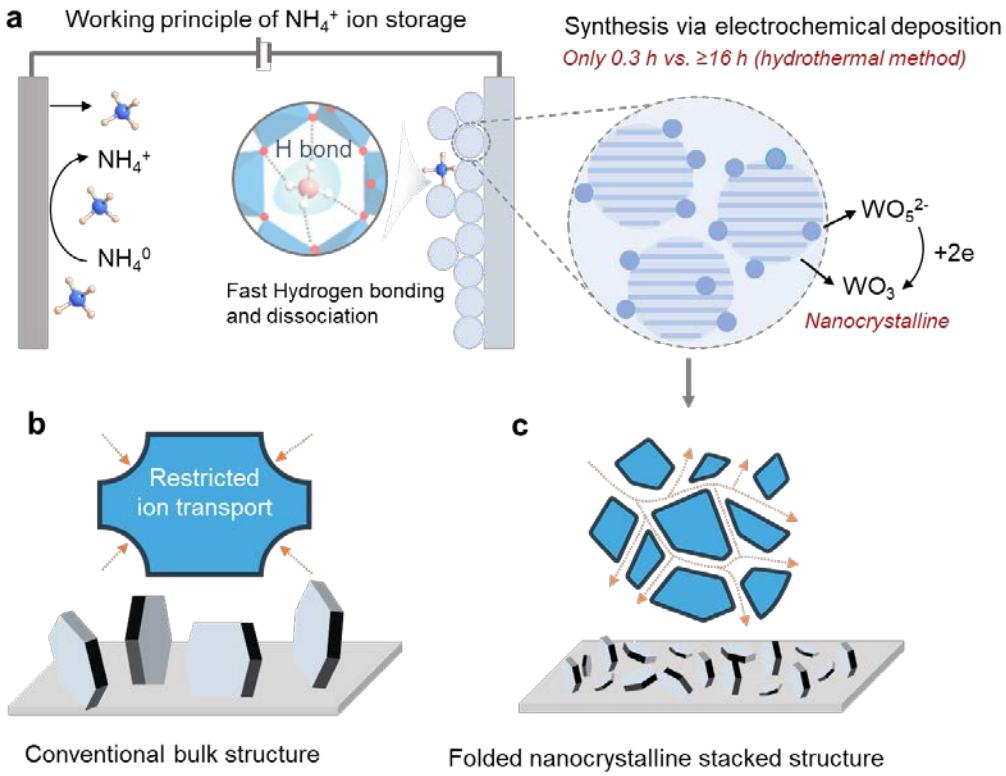


Figure 3.1 Synthesis of nanocrystalline a-WO_3 for efficient NH_4^+ storage: a) Working principle of NH_4^+ ion storage (left) and electrochemical synthesis of nanocrystalline a-WO_3 (right). b, c) Major advantages of folded nanocrystalline structure strategy compared with h-WO_3

Figure 3.2 systematically compares the morphological features of a-WO_3 and h-WO_3, highlighting their distinct structural architectures. The a-WO_3 sample presents a uniform and conformal coating across the CC substrate (**Figure 3.2a**), forming a continuous film with intimate contact with the current collector. At a higher magnification (**Figure 3.2b**), its surface consists of loosely packed, nanoscale particle aggregates, yielding a rough and porous texture that may facilitate electrolyte infiltration and ion accessibility. In contrast, the h-WO_3 sample **(Figure 3.2c**) exhibits large spherical aggregates with a fluffy and porous structure. Its high-magnification image (**Figure 3.2d**) reveals that these microspheres are composed of densely interwoven nanorods, forming an open framework with high crystallinity.

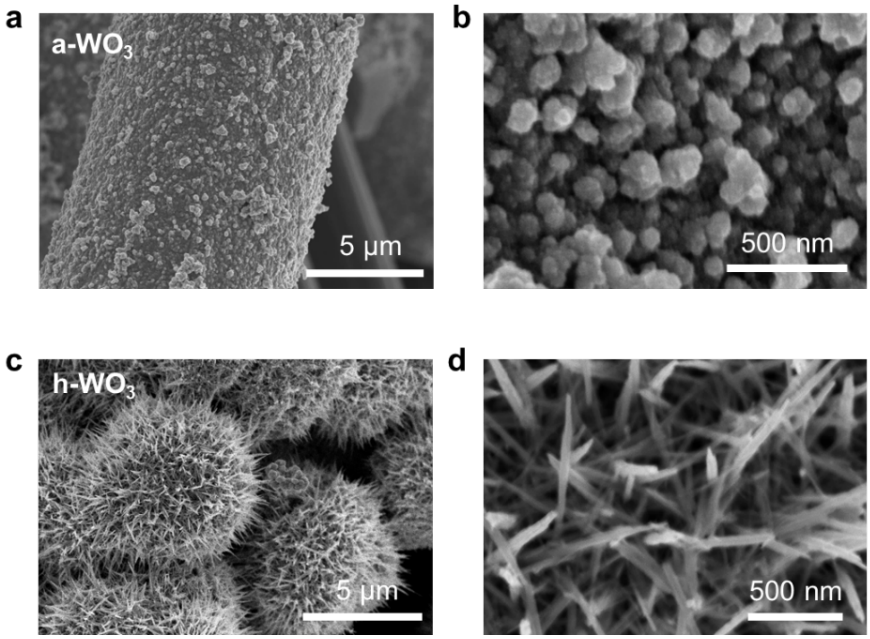


Figure 3.2 SEM images of (a,b) a-WO_3 and (c,d) h-WO_3 at different magnifications.

TEM images were collected to examine the microstructure of the electrochemically deposited a-WO_3. As displayed in **Figure 3.3a-b**, the material exhibits interconnected nanoscale regions, where fine crystallites, approximately 5 nm in diameter, are dispersed within an amorphous framework. These nanocrystalline regions adopt a folded, irregular stacking, forming curved and wrinkled layers rich in grain boundaries. This distinctive morphology results in the generation of continuous nanochannels and shortened ion

diffusion routes, which greatly improve both ion transport and electronic conductivity. In contrast, h-WO_3 shows well-ordered crystalline grains with a typical size of ~20 nm, along with sharp (200) lattice planes of 0.317 nm spacing (**Figure 3.3c-d**). The highly ordered and less defective lattice of h-WO_3 offers more rigid ion pathways, resulting in substantially different electrochemical performance when compared to the amorphous counterpart.

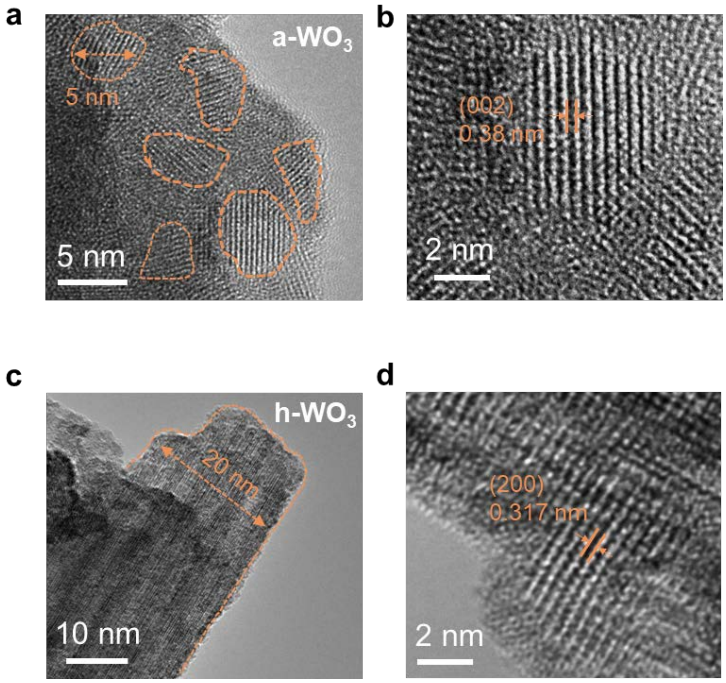


Figure 3.3 TEM images of (a,b) a-WO_3 and (c,d) h-WO_3 at different magnifications.

In addition, the specific surface areas of both a-WO_3 and h-WO_3 were evaluated using N_2 adsorption–desorption measurements. As shown in **Figure 3.4**, the a-WO_3 sample exhibits a significantly higher N_2 adsorption capacity compared to h-WO_3, indicating the presence of a hierarchical porous structure with an enhanced surface area. This porous architecture is expected to facilitate electrolyte ion diffusion and improve surface accessibility, thereby contributing to the superior electrochemical performance observed.

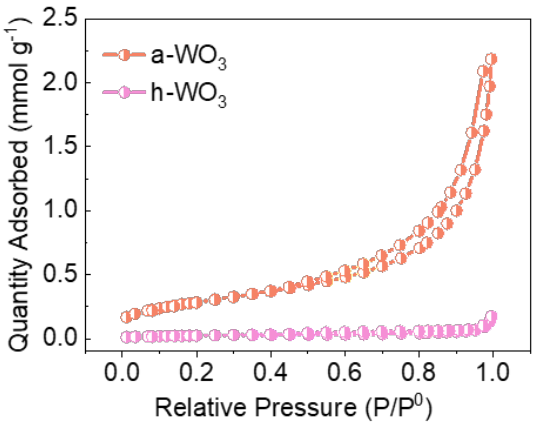


Figure 3.4 N_2 adsorption-desorption isotherms (77 K) of a-WO_3 and h-WO_3.

The electrical conductivity of these two WO_3 materials was subsequently measured. As presented in **Figure 3.5a**, a-WO_3 possesses a significantly higher conductivity compared to h-WO_3, which is attributed to the presence of abundant oxygen vacancies and disordered network structures that facilitate charge carrier transport. This is consistent with the amorphous nature of a-WO_3 revealed by means of XRD (**Figure 3.5b**). In more detail, the a-WO_3 exhibits broad and ill-defined diffraction humps, with a pronounced feature at low 2θ angles (10–15°), indicative of short-range order and lack of long-range crystallinity. In contrast, h-WO_3 shows sharp and well-resolved diffraction peaks corresponding to a hexagonal crystalline structure, with characteristic reflections indexed to the (200), (002), and (202) planes.

Complementary insights were provided by Raman spectroscopy (**Figure 3.5c**). Raman spectroscopy corroborates these findings: the a-WO_3 spectrum displays broad vibrational bands at approximately 210, 666, and 953 cm^{-1}, corresponding to O–W–O bending and W=O terminal stretching modes, whereas h-WO_3 exhibits narrow peaks consistent with well-ordered W–O networks. Notably, a shoulder near 950 cm^{-1} in a-WO_3 is attributed to the presence of surface-bound WO_5^{2-} species and terminal oxygen defects, indicating a high density of active surface sites.

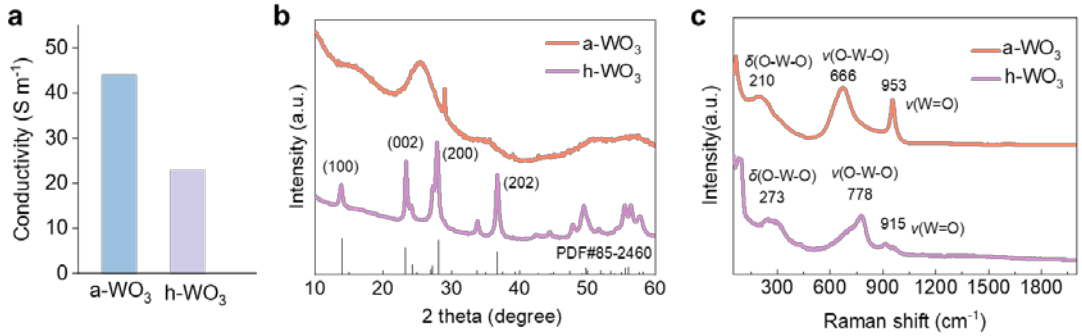


Figure 3.5 (a) Electrical conductivity, (b) XRD patterns and (c) Raman spectra of the a-WO_3 and h-WO_3 electrodes.

The presence of multiple tungsten oxidation in nanocrystalline a-WO_3 was further evidenced through detailed XPS analysis (**Figure 3.6a**). The W 4f spectrum has been deconvoluted into six distinct components, with two primary peaks located at 38.1 eV and 36.0 eV corresponding to W^{6+} species. Additional weaker peaks at 37.5 eV and 35.0 eV are assigned to W^{5+}, while minor contributions at 39.1 eV and 37.1 eV suggest the presence of W^{4+} species. This distribution of mixed-valence tungsten states indicates a significant concentration of oxygen vacancies and pronounced structural disorder within the a-WO_3 framework, both of which are known to promote enhanced electronic conductivity and electrochemical activity. In contrast, the W 4f spectrum of h-WO_3 is dominated by sharp W^{6+} peaks, with only negligible contributions from W^{5+} species, consistent with a well-ordered crystalline phase and near-stoichiometric composition. Further insights are provided by the O 1s (**Figure 3.6b**), which reveal three distinct peaks centered at 529.9 eV, 531.2 eV, and 532.6 eV, corresponding to lattice oxygen, oxygen-deficient sites, and adsorbed hydroxyl groups, respectively. The substantially higher intensity of oxygen vacancy and surface-adsorbed oxygen species in a-WO_3, relative to h-WO_3, confirms the greater defect density and surface reactivity of the amorphous material. These variations in tungsten oxidation states and oxygen coordination environment likely originate from the incorporation of WO_5^{2-} species and oxygen

vacancy formation during the electrochemical deposition process, thereby contributing to the superior electrochemical properties of a-WO_3.

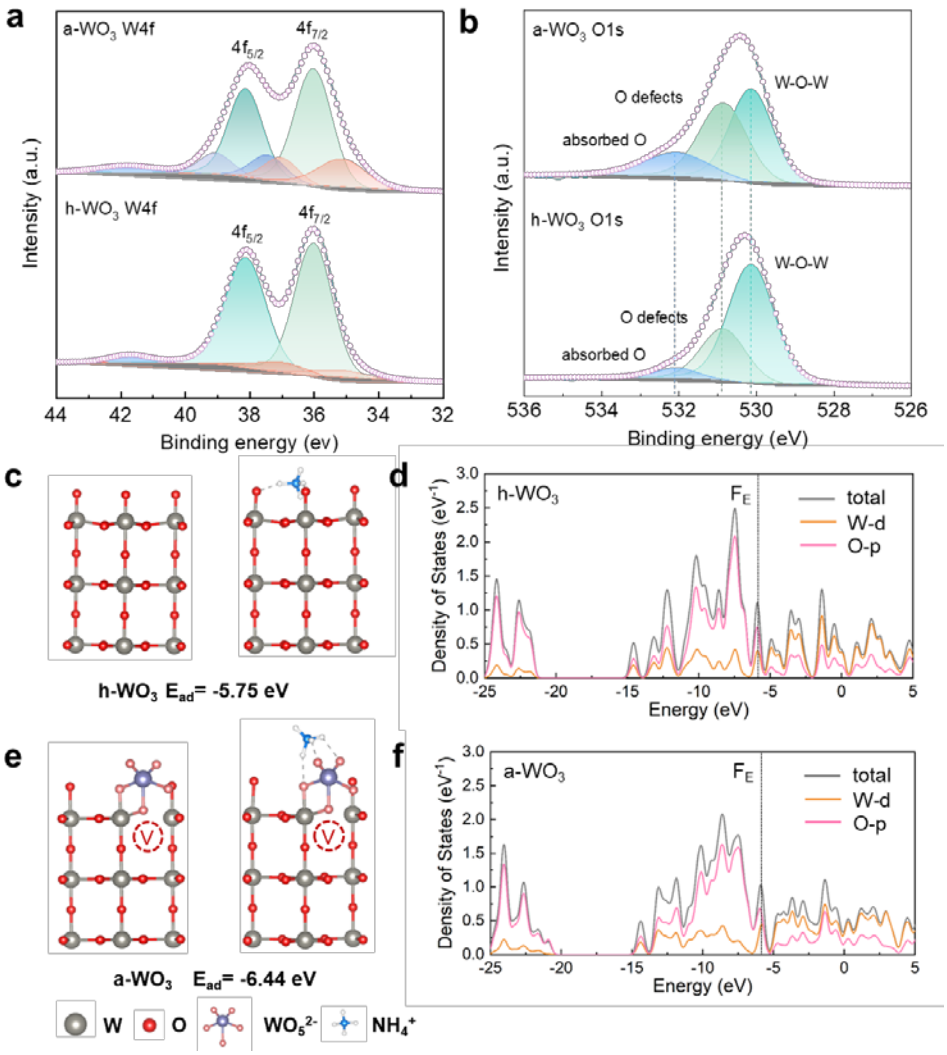


Figure 3.6 XPS and DFT insights into NH_4^+ storage on a-WO_3 and h-WO_3: (a) W 4f XPS spectra and (b) O 1s XPS spectra of a-WO_3 and h-WO_3. Schematic diagram and adsorption energy of single NH_4^+ ions adsorbed on the surface of (c) h-WO_3 and (d) a-WO_3. (e-f) The corresponding DOS diagrams.

To investigate NH_4^+ adsorption energetics, DFT simulations were performed. The calculated adsorption energy of NH_4^+ on the a-WO_3 surface is −6.44 eV, significantly higher than the −5.75 eV observed on h-WO_3. This stronger interaction is attributed to

the presence of surface WO_5^{2-} groups and the negatively charged environment created by oxygen vacancies. The formation of hydrogen bonds between NH_4^+ and terminal oxygen atoms on the WO_3 surface further stabilizes the adsorbed configuration. The projected DOS shows increased electronic density near the Fermi level in a-WO_3, indicating enhanced charge delocalization and stronger electrostatic attraction toward cationic species.

3.2 Growth mechanism of the folded nanocrystalline-stacked the WO_3

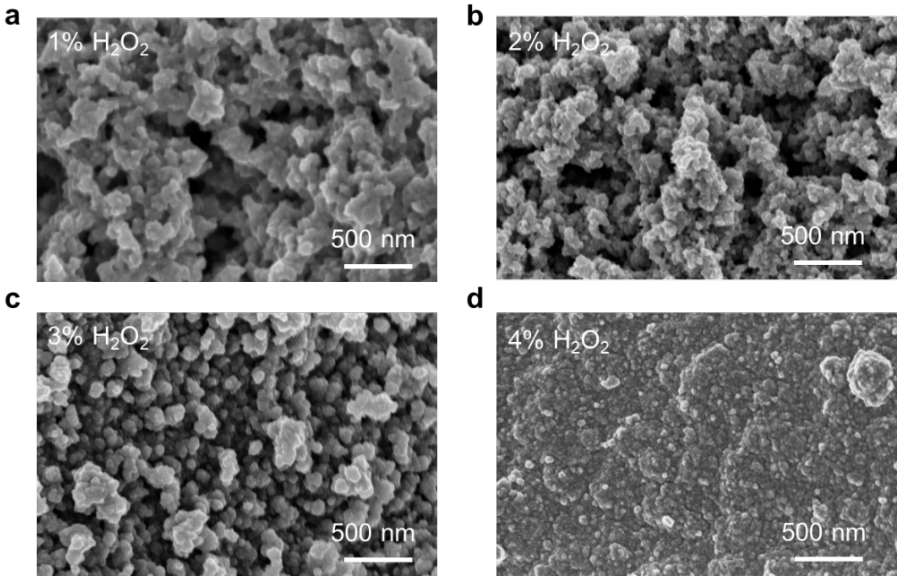


Figure 3.7 SEM images of WO_3 samples prepared with a H_2O_2 concentration of a) 1%, b) 2%, c) 3%, and d) 4%.

The synthesis conditions of a-WO_3 were systematically optimized, with particular emphasis on the influence of H_2O_2 concentration on the resulting material morphology. Related SEM images (**Figure 3.7**) reveal a pronounced morphological evolution as the H_2O_2 concentration increases from 1% to 4%. At a low concentration of 1%, the material exhibits a loosely packed, porous structure. Increasing the concentration to 2% promotes partial densification of the particles and improves overall uniformity. The optimal morphology was obtained at an H_2O_2 concentration of 3%, where nanoparticles are densely packed into a continuous network with minimal interparticle voids, achieving a

desirable balance between porosity and mechanical integrity. However, further increasing the concentration to 4% results in excessive particle aggregation, which diminishes the effective surface area and limits ionic accessibility.

Next, electrochemical performance of the samples prepared with different H_2O_2 concentrations was evaluated. As shown in **Figure 3.8a–d**, with increasing H_2O_2 concentration, the pseudocapacitive contribution of the material gradually increases.

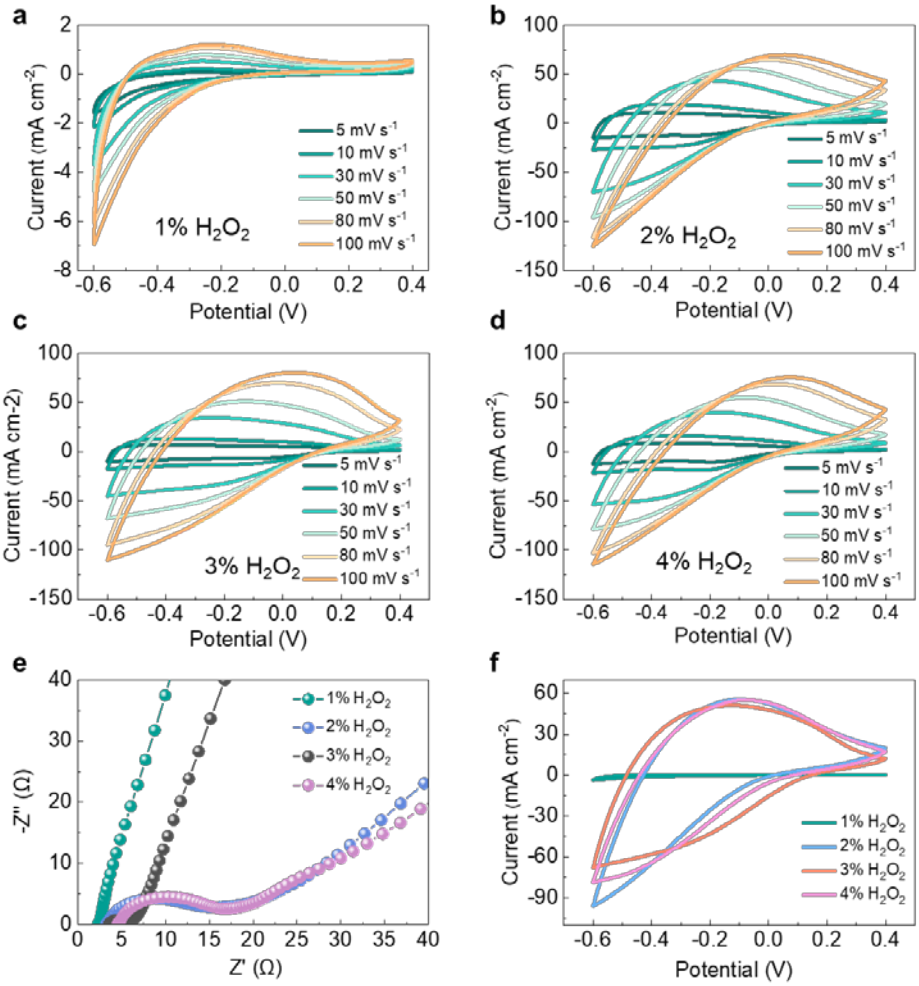


Figure 3.8 Cyclic voltammograms of WO_3 samples prepared with a H_2O_2 concentration of (a) 1%, (b) 2%, (c) 3%, and (d) 4% at different scan rates. (e) Nyquist plots and (f) Cyclic voltammograms of WO_3 samples prepared with different H_2O_2 concentrations at a scan rate of 50 mV s^{-1}.

However, when the concentration exceeds 3%, a decline in rate performance is observed. This is mainly attributed to excessive particle aggregation, which reduces the effective utilization of the material. which can be attributed to particle over-aggregation and a subsequent reduction in the number of accessible active sites. The EIS results (**Figure 3.8e**) further reveal that the samples prepared with 1% and 3% H_2O_2 exhibit lower charge transfer resistance, indicating faster electron transport kinetics. In addition, Cyclic voltammogram obtained at the same scan rate (**Figure 3.8f**) show that the sample synthesized with 3% H_2O_2 possesses the largest redox peak area, reflecting enhanced pseudocapacitive behavior and superior charge transfer capability.

The formation of the folded nanocrystalline-stacked tungsten oxide architecture during electrochemical deposition is supposed to be governed by a complex interplay of reduction kinetics, nucleation density, electrochemical potential, and deposition time. Understanding this growth mechanism is essential for the rational control of film morphology, defect concentration, and phase composition, which ultimately determine electrochemical behavior. In this chapter, the growth behavior was systematically examined by modulating the deposition parameters and elucidating the structural evolution via integrated spectroscopic and microscopic analyses.

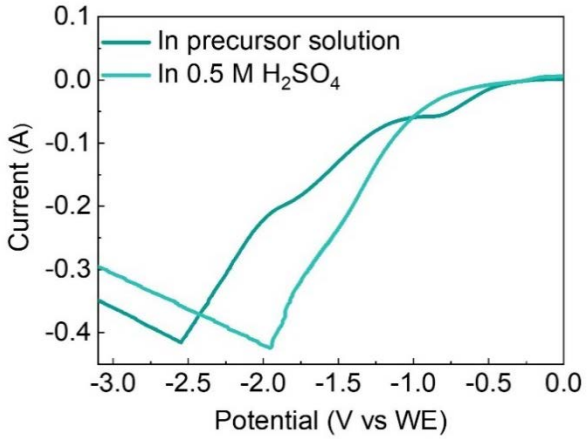


Figure 3.9 LSVs of an electrode in a precursor solution + 0.5 M H_2SO_4 at a scan rate of 50 mV s^{-1}

LSV curves were first monitored to examine the electrochemical behavior of the precursor (**Figure 3.9**). A sharp increase in cathodic current is observed around −0.8 V (*vs*. the working electrode), indicating the onset of WO_5^{2-} reduction and nucleation of tungsten oxide species on the CC substrate. At this early stage, sparse and poorly defined nuclei are formed, as evidenced by related SEM images (**Figure 3.10**) where isolated clusters are seen with a limited surface coverage. As the applied potential becomes more negative, the nucleation rate increases rapidly, leading to denser deposition and the formation of interconnected networks. At −2.5 V, an optimal potential identified for structural quality and electrochemical performance, a continuous and porous film composed of nanospheres was observed. This morphology reflects a regime of fast reduction kinetics coupled with sufficient nucleation density to support the formation of multi-grain stacked domains with nanoscale dimensions. At more negative potentials, gas evolution significantly, disrupting the uniform growth and potentially introducing internal stress and inhomogeneity.

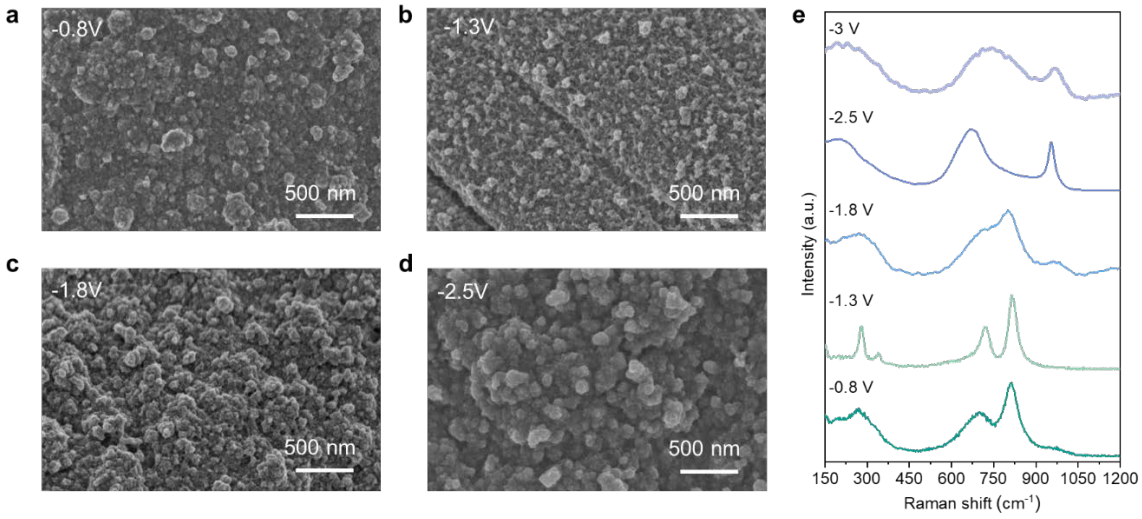


Figure 3.10 (a-d) SEM images of WO_3 samples deposited at a potential of −0.8 V (a), −1.3 V (b), −1.8 V (c) and −2.5 V (d) (*vs*. OCP). (e) Their Raman spectra.

The influence of deposition potential on the crystal structure and phase distribution was further examined by means of Raman spectroscopy (**Figure 3.10e**). At low potentials, sharp and well-defined bands are observed near 700-800 cm^{-1}, corresponding to the

characteristic W-O-W bond stretching vibrations, associated with monoclinic WO_3. A further increase in this potential significantly enhances the intensities of these peaks, indicating the formation of more stable crystalline structures. However, an increase in deposition potential progresses further the reduction process, resulting in structural changes in WO_3, including the formation of partially amorphous WO_3 or mixed-phase regions. Additionally, a peak near 950 cm^{-1} appears. This is an indication of the formation of oxygen vacancies at higher reduction potentials, possible adsorption of anions (e.g., WO_5^{2-}) on the WO_3 surface, and ultimately the altered local chemical environment of W=O bonds.

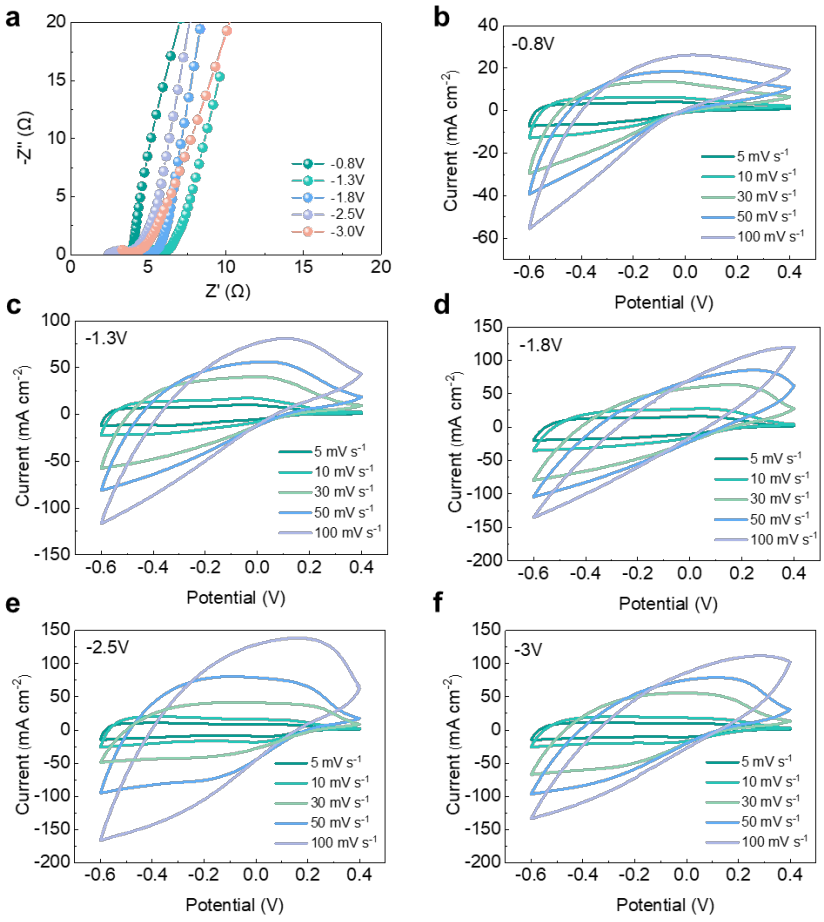


Figure 3.11 (a) Nyquist plots of the a-WO_3 samples prepared with different deposition potentials. Cyclic voltammograms of a-WO_3 samples prepared with a deposition potential of (b) −0.8 V, (c) −1.3 V, (d) −1.8 V, (e) −2.5 V, and (f) −3 V (*vs*. OCP) at different scan rates ranging from 5 to 100 mV s^{-1}.

Meanwhile, electrochemical tests were conducted to evaluate the performance of materials prepared with different deposition potentials (**Figure 3.11**). One can see that as the deposition potential increases the electrode capacitance continuously rises, reaching its peak at a deposition potential of -2.5 V before its decline.

During this electrochemical deposition process, the applied deposition time was also found to be crucial to vary the morphology of these WO_3 samples. The Raman spectra of WO_3 samples prepared at different deposition times (**Figure 3.12a**) show several significant changes as the deposition time increases. For example, the intensities of the characteristic peaks associated with the W-O stretching and bending vibrations are much enhanced with a longer deposition time. This tendency suggests an increase in crystallinity of synthesized WO_3 samples in that an extended deposition time allows for the formation of a more ordered WO_3 lattice. In more detail, the prominent peaks appear around 800 cm^{-1} and 950 cm^{-1}. Since they are respectively attributed to W=O terminal bonds and bridging W-O-W bonds, improved structural integrity and reduced amorphization of these samples are further confirmed. Furthermore, a longer deposition time results in narrower peaks, reflecting reduced structural disorder and the growth of larger crystalline domains of these WO_3 samples, or a transition from an initially amorphous and poorly crystallized structure to a more crystalline one. In addition, some slight redshifts and blueshifts in peak positions are observed with an increased deposition time. These shifts suggest changes in local bonding environments, potentially due to strain relaxation or improved atomic ordering within the WO_3 framework. The formation of additional phases or sub-domains within the WO_3 matrix is thus realized.

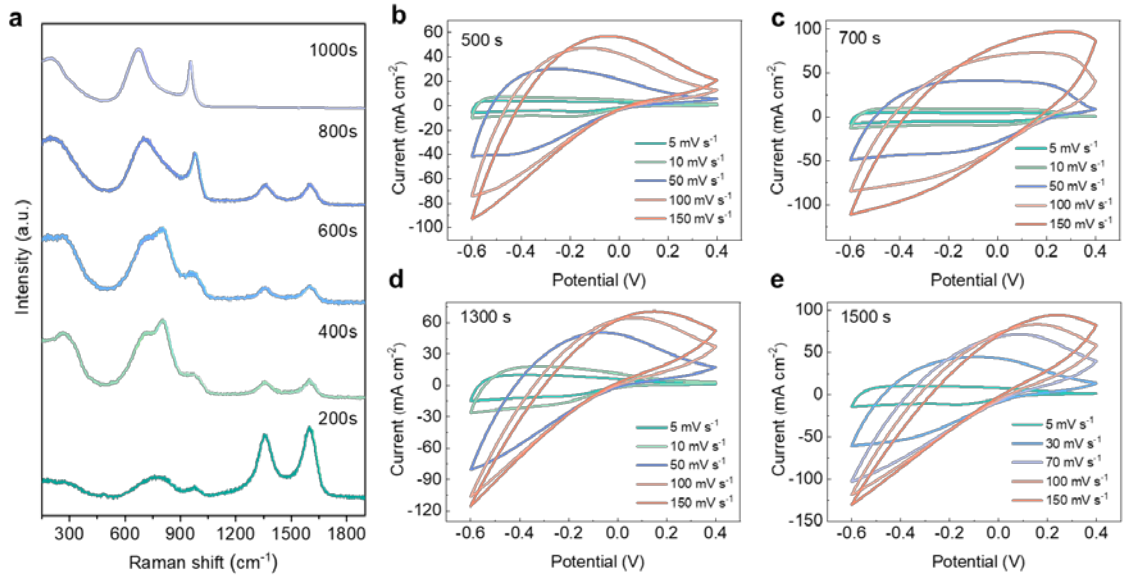


Figure 3.12 a) The Raman spectra of a-WO_3 at different deposition times. b-e) Cyclic voltammograms of WO_3 samples prepared with a deposition time of (b) 500 s, (c) 700 s, (d) 1300 s, and (e) 1500 s at different scan rates.

In addition, the electrochemical behavior of a-WO_3 materials deposited at varied durations was also examined (**Figure 3.12b-e**). As the deposition time increases, the enclosed CV area and the prominence of redox peaks initially grow, reflecting enhanced charge storage and pseudocapacitive behavior. They are due to increased surface areas and improved material connectivity of WO_3 samples. However, beyond a certain duration (e.g., 1000 s), the performance begins to plateau or even decline. This is perhaps since excessive WO_3 deposition leads to aggregation or reduced ion accessibility. Therefore, the optimal deposition time was determined to be 1000 s in this chapter since the resultant WO_3 material balances its surface area, porosity, and charge transfer efficiency.

3.3 Storage mechanism about NH_4^+ ion in the WO_3

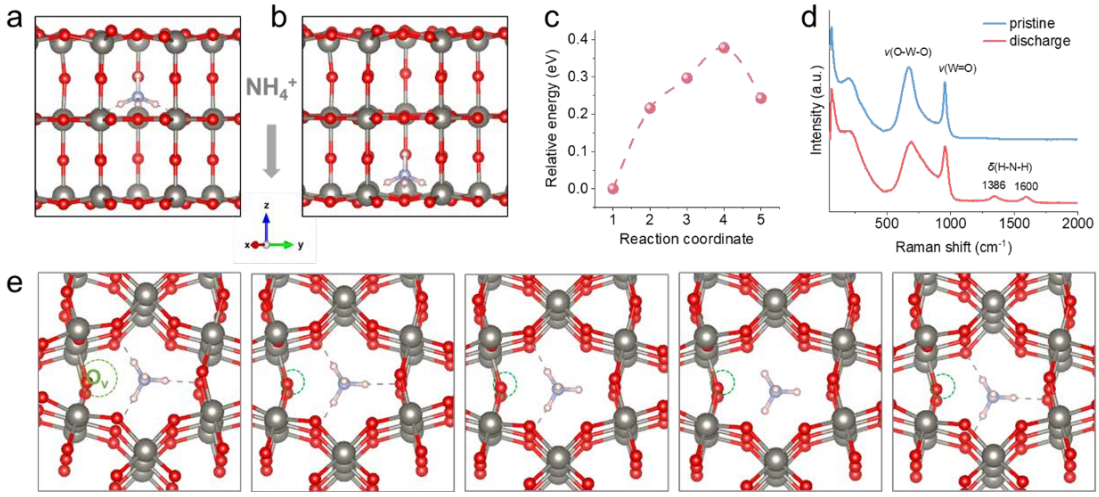


Figure 3.13 Simulated NH_4^+ diffusion in a-WO_3. (a, b) Initial and final configurations. (c) Energy profile showing a diffusion barrier of ~0.38 eV. (d) Raman spectra at the pristine and discharge states. (e) Snapshots of the migration pathway with transient H-bonding interactions.

The migration behavior of ammonium ions was simulated within the tungsten oxide lattice. **Figure 3.13a** and **Figure 3.13b** present the structural configurations before and after the migration of NH_4^+ ions. During the diffusion process, NH_4^+ undergoes a series of reorientations accompanied by local structural rearrangements of the surrounding WO_6 octahedra. The corresponding energy profile (**Figure 3.13c**) reveals a diffusion barrier of approximately 0.38 eV, indicating that protonated NH_4^+ can migrate efficiently within the a-WO_3 network. This barrier is comparable to, or even lower than, the diffusion barriers of protons or other small cations in similar oxides, further demonstrating the superior ion-conduction capability of a-WO_3 in aqueous systems. In addition, Raman measurements performed before and after ammonium insertion clearly show the formation of H-N bonding within the lattice and reversible changes in W-O and W=O bands upon NH_4^+ insertion and extraction. The structural reversibility and retention of vibrational features highlight the robustness of the amorphous–nanocrystalline framework during repeated cycling (**Figure 3.13d**).

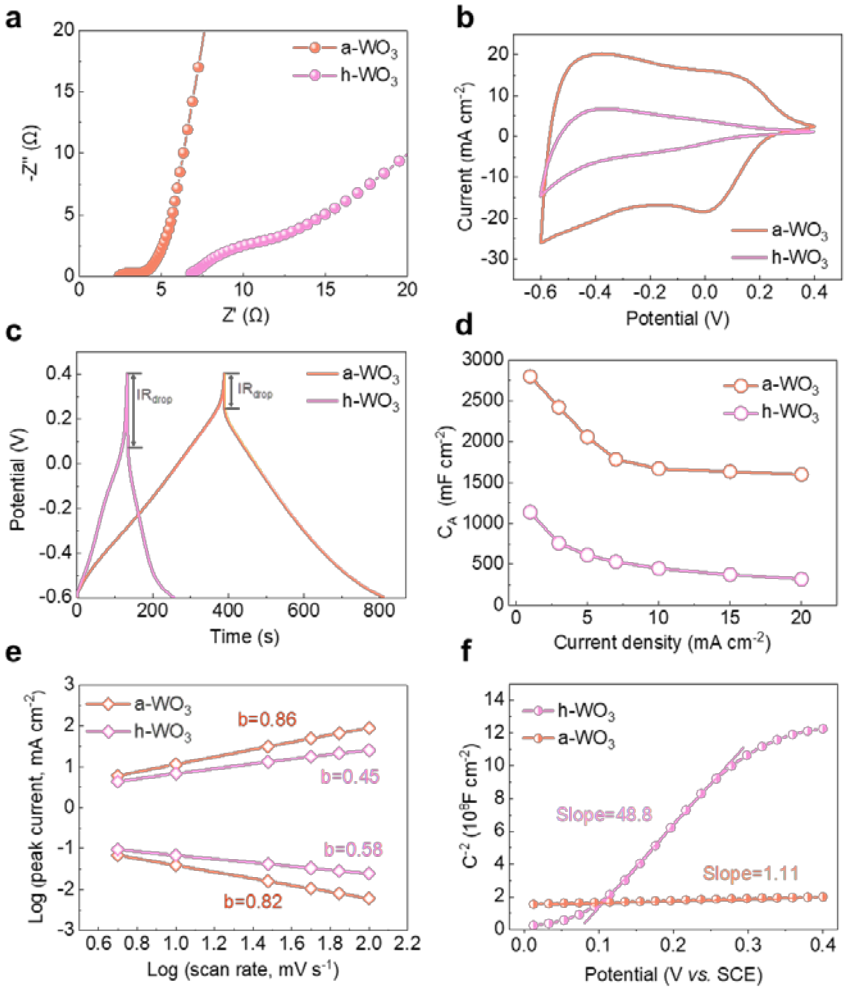


Figure 3.14 Electrochemical performance of a-WO_3 and h-WO_3 anodes: Comparison of (a) Nyquist plots, (b) CVs at a scan rate of 5 mV s^{-1}, (c) GCD profiles at a current density of 10 mA cm^{-2}, (d) Areal capacitance as a function of the current density. (e) Comparison of *b* values of a-WO_3 and h-WO_3. (f) Mott-Schottky plots of the a-WO_3 and h-WO_3 electrodes.

To gain deeper insight into the migration mechanism, several intermediate states along the diffusion pathway were extracted (**Figure 3.13e**). It is evident that ammonium ions form transient hydrogen-bond interactions with nearby lattice oxygen atoms during migration. These dynamic hydrogen bonds serve as temporary "anchoring sites" stabilizing the ion at intermediate positions while simultaneously lowering the overall migration barrier. Such a hopping-like diffusion mechanism, mediated by short-lived

hydrogen-bond networks, not only ensures rapid NH_4^+ transport but also prevents long-range structural collapse.

The electrochemical behavior of the folded nanocrystalline-stacked a-WO_3 electrode was tested to understand its charge storage mechanism with NH_4^+ ions and related diffusion-controlled processes. In the EIS Nyquist plots a significantly smaller semicircle is seen in the high-frequency region for a-WO_3 compared to h-WO_3, indicating a lower charge transfer resistance. Moreover, a near-vertical line in the low-frequency region signals ideal capacitive behavior and efficient NH_4^+ ion transport across the electrode/electrolyte interface. The contact resistance of a-WO_3 was measured to be as low as 2 Ω, considerably lower than the 7 Ω of h-WO_3. It reflects enhanced electrode wetting and improved interfacial compatibility, likely due to the presence of oxygen-containing functional groups and oxygen vacancies (**Figure 3.14a**). The CVs recorded between −0.6 and 0.4 V show nearly rectangular shapes with broad redox features, indicative of capacitive-dominated behavior (**Figure 3.14b**). The a-WO_3 electrode exhibits a larger integrated CV area and more defined peaks than h-WO_3, suggesting a greater pseudocapacitive contribution and enhanced electrochemical reactivity. The GCD profiles further support this, displaying symmetric triangular shapes with extended discharge times (**Figure 3.14c**). The areal capacitance of a-WO_3 reaches 2783 mF cm^{-2} at a current density of 1 mA cm^{-2} and retains over 50% of its capacitance even at 20 mA cm^{-2}, indicating excellent rate capability. In comparison, h-WO_3 shows a significantly lower capacitance and a faster decay with an increased current density (**Figure 3.14d**). The kinetic nature of charge storage was probed *via* the power-law relation $i = av^b$, where i is the peak current, v is the scan rate, a is a constant, and b is a descriptor of the charge storage mechanism. The log(i)–log(v) plots for a-WO_3 (**Figure 3.14e**) yield b-values of 0.88 and 0.82 for cathodic and anodic peaks, respectively. It has been well recognized that a b-value close to 0.5 reflects a diffusion-dominated intercalation process, while a value approaching unity is characteristic of surface-confined capacitive behavior[119]. Hence, the results in this case clearly indicate that the charge storage mechanism in a-

WO_3 is primarily driven by pseudocapacitive surface reactions, which are advantageous for high-rate NH_4^+ storage. Conversely, the crystalline h-WO_3 electrode displays much smaller *b*-values — only 0.45 for the cathodic and 0.58 for the anodic process. In other words, the sluggish and diffusion-limited nature of charge storage happens in bulk crystalline domains. Taking all these facts together, such comparison suggests that the amorphous structure of a-WO_3 inherently favors surface-controlled pseudocapacitive reactions, enabling faster kinetics than the diffusion-governed intercalation commonly observed in long-range ordered crystalline lattices. This structural advantage of a-WO_3 is therefore crucial in achieving superior rate performance for NH_4^+ storage.

Considering that both h-WO_3 and a-WO_3 materials are *n*-type semiconductors, their Mott–Schottky analysis (**Figure 3.14f**) was conducted to gain deeper insights into their electronic behavior. Such an approach has been frequently employed to calculate the donor density since it is inversely proportional to the slope of the Mott–Schottky plot[120]. The stark difference in the slopes, with h-WO_3 exhibiting a value of 48.8 and a-WO_3 only 1.11, underscores a dramatic increase in donor density of a-WO_3. The significantly higher donor density in a-WO_3 aligns with the presence of a greater number of oxygen vacancies. These vacancies act as shallow donors in the conduction band, enhancing the charge carrier concentration and conductivity, eventually making a-WO_3 more suitable for electrochemical NH_4^+ ions storage. Additionally, the near-horizontal slope for a-WO_3 suggests a remarkably uniform distribution of donor states that allows greater flexibility in accommodating oxygen vacancies. In contrast, h-WO_3, featuring a higher slope and a lower donor density, is indicative of fewer oxygen vacancies as indicated and is consistent with its more ordered crystalline structure.

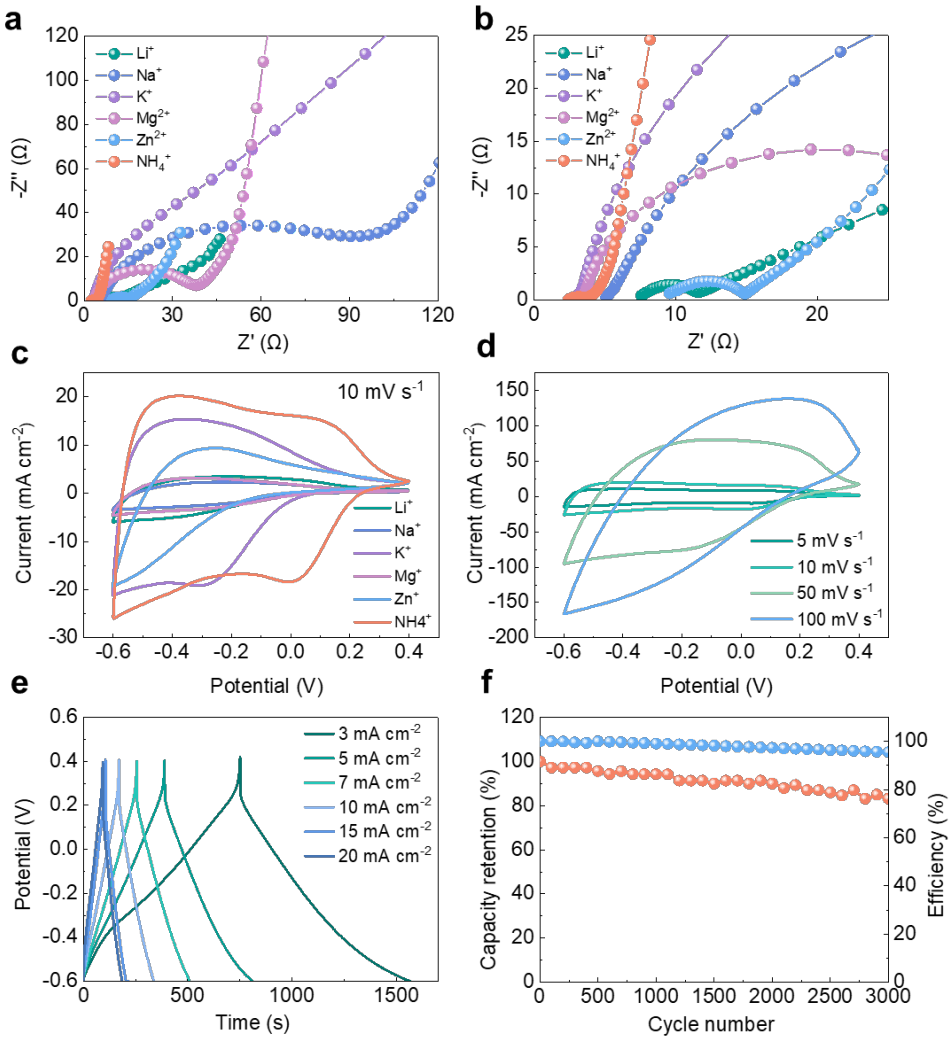


Figure 3.15 Electrochemical performance of the a-WO_3 electrode: a,b) Nyquist plots and c) Cyclic voltammograms in the electrolytes containing various cations, d) Cyclic voltammograms at different scan rates ranging from 5 to 100 mV s^{-1}, e) GCD curves at different current densities varied from 3 to 20 mA cm^{-2}, f) Cycling performance and coulombic efficiency in 1 M NH_4Cl.

The combination of EIS with Cyclic voltammograms was further utilized to evaluate the ion-storage behavior of the a-WO_3 electrode. A series of metal cations, including Li^+, Na^+, K^+, Mg^{2+}, and Zn^{2+}, were selected as charge carriers to systematically probe the ionic response (**Figure 3.15a–c**). Notably, for NH_4^+- and K^+- containing electrolytes, the high-frequency semicircle is almost completely absent in their Nyquist plots, indicating extremely low charge-transfer resistances and facile ion transport. This observation

implies that NH_4^+ and K^+ ions can reversibly intercalate and deintercalated within the WO_3 framework with minimal kinetic barriers, thereby enabling superior high-rate storage capability compared to the other investigated ions.

For cations with a relatively smaller hydrated radius, such as Li^+ (12.3 Ω) and Na^+ (15.4 Ω), the impedance response also remains low, further highlighting the critical role of efficient ionic conductivity and reduced interfacial resistance in facilitating ion accommodation within the WO_3 lattice. In contrast, multivalent or larger-radius ions such as Mg^{2+} (39.6 Ω) and Zn^{2+} (90 Ω) produce significantly more pronounced semicircles in the high-frequency region of their Nyquist plots, which reflects their sluggish interfacial charge-transfer kinetics and limited diffusion capability within the electrode.

Interestingly, the Nyquist profile of NH_4^+ ions in the low-frequency domain exhibits a nearly vertical line, characteristic of an ideal capacitive response. This behavior can be attributed to the relatively small effective hydrated radius and the low molecular weight of NH_4^+ ions, which together with their strong hydrogen-bonding capability toward the WO_3 surface promote rapid ion migration and stable adsorption during the redox process. Such hydrogen-bond-assisted interactions effectively stabilize the intercalation pathway, minimize mass-transport resistance, and accelerate redox reaction kinetics. Collectively, these results confirm that NH_4^+ ions exhibit inherently faster diffusion and more efficient electrochemical dynamics on the WO_3 electrode than their alkali- and multivalent-ion counterparts, thereby delivering enhanced high-rate storage performance.

In summary, the NH_4^+ storage in a-WO_3 follows a pseudocapacitive mechanism enabled by a combination of physical and chemical features: high surface area of a-WO_3 for the double-layer formation, rich defect chemistry for rapid redox transitions, and flexible amorphous domains for strain relaxation during the charge/discharge process. The incorporation of NH_4^+ ions is not limited to bulk intercalation but involves surface adsorption stabilized by hydrogen bonding and electrostatic interactions with defect sites. This mechanism accounts for the excellent rate performance, high capacitances, and cycling stability observed in the a-WO_3 electrode.

3.4 The performance of the ammonium-ion hybrid supercapacitor

To evaluate the practical applicability of the folded nanocrystalline-stacked a-WO_3 electrode, a full AIHS device was assembled using a-WO_3 as the anode and PANI as the cathode. The choice of PANI was motivated by its high theoretical capacitance, favorable redox reversibility, and compatibility with mild aqueous electrolytes. The PANI cathode was fabricated by *in situ* polymerization of aniline monomers on a carbon cloth substrate, ensuring uniform coating and strong adhesion. The a-WO_3 anode and PANI cathode were separated by a glass fiber membrane and immersed in 1 M NH_4Cl aqueous electrolyte. The full cell configuration is illustrated in **Figure 3.16a**.

The a-WO_3 anode operated stably in the potential window of −0.6 V to 0.4 V, while the PANI cathode functioned effectively between 0 and 1.0 V. Based on these stable potential ranges, the full device was operated at a voltage window of 1.6 V. The cyclic voltammogram of the assembled WO_3//PANI AIHS at a scan rate of 50 mV s^{-1} exhibits broad redox peaks across the entire voltage range, confirming the redox behavior of the electrodes and the pseudocapacitive nature of the device. (**Figure 3.16b**) Within the potential window of 0–1.6 V, the device exhibits an areal capacitance of as high as 1716 mF cm^{-2} at a current density of 3 mA cm^{-2}. Even at an elevated current density of 20 mA cm^{-2}, the capacitance retention remains at 67.1%, confirming the favorable rate capability and efficient ion transport kinetics of the system (**Figure 3.16c**). A practical demonstration was carried out by powering an LED after charging the device, which further validates its applicability (**Figure 3.16d**). Electrochemical characteristics were systematically investigated by CV and GCD analysis (**Figure 3.16e-f**). One can see that there is a reversible multi-electron transfer reaction, reflecting excellent reversibility and rapid electron transport and efficient capacitive response of this device. Furthermore, the long-term cycling stability was examined at a current density of 5 mA cm^{-2}, where the WO_3//PANI AIHS retains 81.5% of its initial capacitance after 3000 cycles (**Figure 3.16g**), indicating durable operation under repeated cycling.

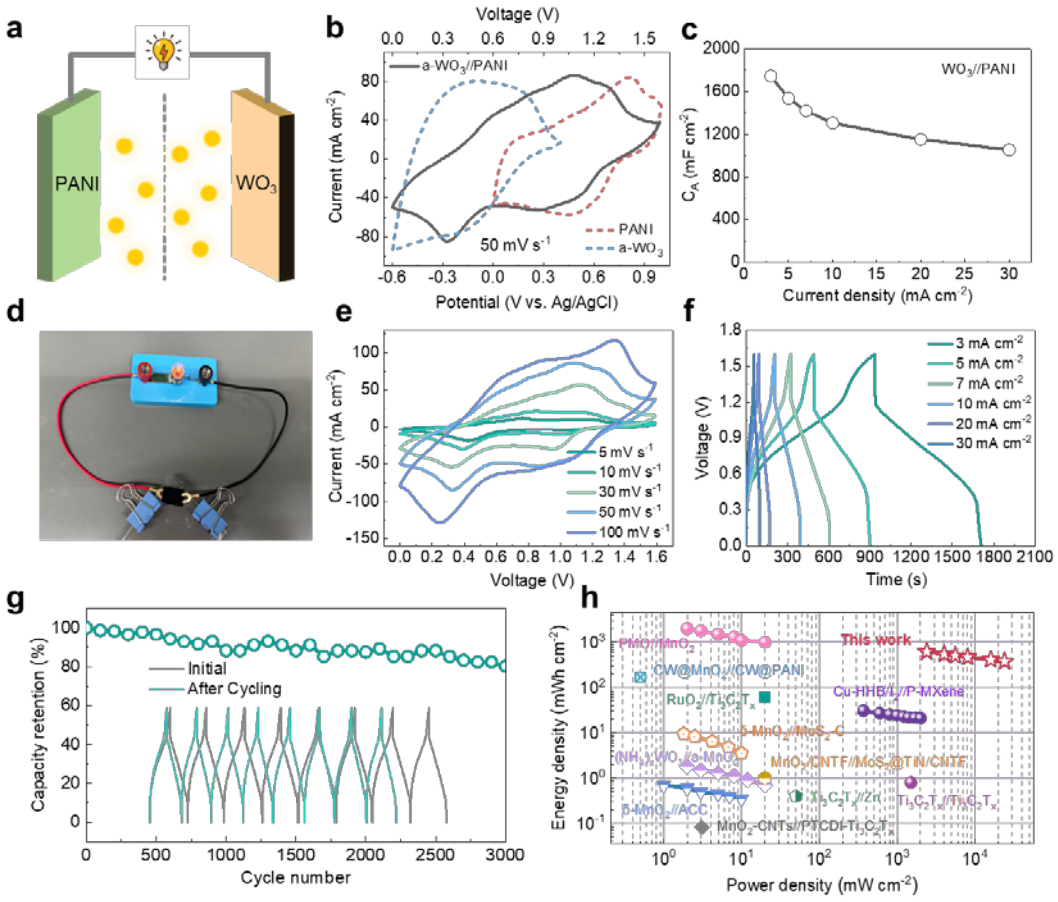


Figure 3.16 Electrochemical performance of a WO_3//PANI AIHS device: a) Schematic illustration, b) CVs of the PANI cathode, the WO_3 anode, and the WO_3//PANI AIHS at a scan rate of 50 mV s^{-1}, c) Specific capacitances calculated from different current densities, d) lighting a LED using a WO_3//PANI AIHS, e) CVs at different scan rates and f) GCD curves at different current densities, g) Cycling stability at a scan rate of 20 mA cm^{-2} for 3000 cycles, h) Ragone plot in comparison with other reported HSCs.

The energy and power characteristics of the WO_3//PANI AIHS were found to be benchmarked against state-of-the-art supercapacitors, as shown in its Ragone plot (**Figure 3.16h**). Its maximum energy density is 620 μWh cm^{-2} at a power density of 2400 μW cm^{-2}, significantly surpassing many previously reported systems. Remarkably, even at an ultrahigh power density such as 23,980 μW cm^{-2}, this device maintains an energy density of 374 μWh cm^{-2}. These values outperform other advanced hybrid

supercapacitors, such as MnO_2/CNTF//MoS_2@TiN/CNTF[121], δ-MnO_2//ACC[77], $Ti_3C_2T_x$/CNF//$Ti_3C_2T_x$/CNF[122], PMO//MnO_2[73], Cu-HHB/I_2//P-Mxene[68], *δ*-MnO_2//MoS_2-C A-HSC[123], MnO_2-CNTs//PTCDI-$Ti_3C_2T_x$[124], CW@MnO_2//CW@PANI AASC[125] These results highlight the superior energy and power output of the WO_3//PANI AIHS, making it a strong candidate for next-generation energy storage systems.

In summary, the integration of the folded nanocrystalline-stacked a-WO_3 anode with a conductive and stable PANI cathode enables a high-performance AIHS with a wide operating voltage, excellent capacity retention, fast rate response, and outstanding energy–power output. These results highlight the promise of defect-engineered amorphous tungsten oxide electrodes for practical energy storage applications and provide a scalable path for the development of next-generation hybrid electrochemical devices.

3.5 Conclusion

In this chapter, a novel amorphous tungsten oxide electrode with a folded nanocrystalline-stacked architecture has been developed, characterized, and evaluated for high-performance NH_4^+ storage. The material design is guided by the need to overcome key limitations of conventional crystalline WO_3, namely its low conductivity, rigid framework, and limited NH_4^+ accessibility. By employing a rapid electrochemical deposition strategy, nanosized WO_3 crystallites are generated and embedded within a disordered matrix, forming a highly porous, grain-boundary-rich film directly on carbon cloth. Structural and spectroscopic analysis confirms the presence of amorphous domains, abundant oxygen vacancies, and surface hydroxyl groups, all of which contribute to improved ionic transport and redox activity.

Through controlled variation of deposition potential and time, the growth mechanism of the folded nanocrystalline-stacked structure has been elucidated. This structure supports capacitive-dominated NH_4^+ storage behavior, as confirmed by electrochemical measurements and kinetic analysis. In particular, the a-WO_3 electrode demonstrates high

areal capacitances, excellent performance, and outstanding reversibility. They are believed to be attributable to the dominance of pseudocapacitive processes and enhanced interfacial charge transfer.

Integration of the a-WO_3 anode with a PANI cathode in a full-cell AIHS configuration results in a device exhibiting a wide operating voltage (1.6 V), high energy and power densities (up to 620 μWh cm^{-2} and 23,980 μW cm^{-2}, respectively), and excellent cycling stability over 3000 cycles. Compared to previously reported hybrid systems, the WO_3//PANI AIHS features superior performance metrics, validating the effectiveness of the material design strategy.

In conclusion, this study establishes the folded nanocrystalline-stacked a-WO_3 as a highly promising electrode architecture for next-generation non-metal ion storage systems. It also offers insights into the role of amorphization, defect engineering, and microstructural control in enabling fast, reversible ion storage under practical conditions. The findings provide a strong foundation for the subsequent chapters, which extend the material design toward photo-enhanced NH_4^+ storage by integrating additional functional material.

4 WO_3/TiO_2 heterojunctions for light-assisted energy storage

Photo-assisted energy storage devices have been paid much attention recently[53]. To establish them, electrodes with excellent electrochemical performance such as the rationally designed tungsten oxide nanoparticles in Chapter 3 are highly needed. Nevertheless, when directly employed as photoelectrodes, WO_3 suffers from several intrinsic material bottlenecks. Although its moderate bandgap (2.6–2.8 eV) enables visible-light absorption, the photocatalytic efficiency remains small in that it is limited by ultrafast charge recombination processes with carrier lifetimes only on the order of ~10^{-9} s[126,127]. In addition, the poor conductivity and possible structural degradation during charge/discharge cycling further exacerbate these issues. Collectively, these limitations highlight the necessity of developing composite electrode architectures that can overcome the constraints of single-component WO_3 while leveraging synergistic effects to enhance both electronic transport and photoelectrochemical performance.

For various composite electrode architectures, TiO_2 is an almost perfect candidate to integrate with WO_3. This is because it presents superior photocatalytic activity, stemming from efficient charge separation mechanisms and extended carrier lifetimes, with electron and hole mobilities[128–130]. The exceptional chemical stability of TiO_2 across diverse electrochemical environments offers potential structural reinforcement for the construction of various composite systems. Crucially, the band alignment between these two materials — the conduction band of TiO_2 at -0.3 V and WO_3 at +0.4 V (*vs*. NHE) — establishes a Type II heterojunction (as demonstrated in Chapter 1) that thermodynamically favors charge separation[131,132]. The wavelength dependence of the photo-enhancement effect reflects the combined optical absorption characteristics of both materials. While TiO_2 primarily absorbs in the ultraviolet region due to its wide bandgap, WO_3 extends the photo response into the visible light range. Therefore, more efficient utilization of the solar spectrum is expected to be enabled[133–135]. The heterojunction formation may also introduce new electronic states at the interface, potentially creating sub-bandgap absorption that further extends the photoactive spectral range[136,137].

The WO_3/TiO_2 composite strategy is believed to exploit three synergistic mechanisms. First, heterojunction-driven charge spatially isolates photogenerated electrons and holes, reducing recombination rates and amplifying photo-enhancement effects[138]. Second, dual-pathway ion storage combines rapid surface adsorption at TiO_2 sites with high-capacity bulk intercalation in WO_3, merging kinetic advantages with capacity benefits. Third, TiO_2 nanoparticles provide structural scaffolding that mechanically stabilizes the WO_3 framework against cycling-induced volume changes[139,140]. This chapter clarifies how to achieve several related objectives: enhanced capacity through cooperative storage mechanisms, improved rate performance *via* facilitated charge transport, superior photo-responsive through efficient charge separation, and extended cycling stability *via* structural reinforcement. The results validate composite electrode strategies and establish precedents for advancing both fundamental understanding of multi-component electrode behavior and practical pathways toward next-generation energy storage systems.

4.1 Band diagram analysis of WO_3/TiO_2 photo-assisted ammonium ion storage mechanism

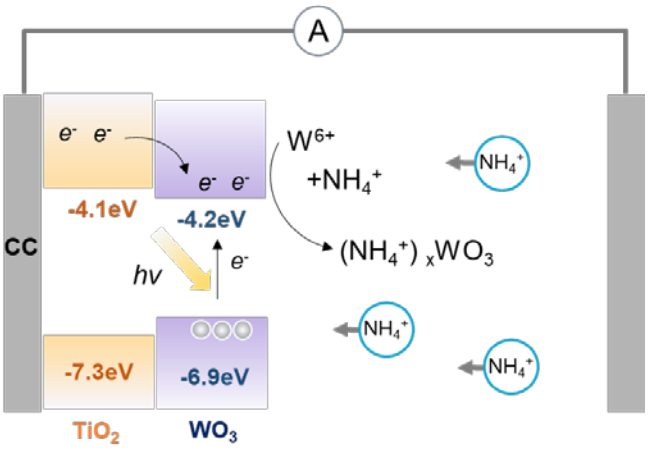


Figure 4.1 Mechanism of photo-assisted charge separation and ammonium ion storage in a WO_3/TiO_2 heterojunction

Figure 4.1 provides a comprehensive visualization of the electronic structure alignment, charge separation processes, and ion insertion pathways in WO_3/TiO_2 composite electrodes. The band alignment between TiO_2 and WO_3 establishes a Type II heterojunction configuration that is thermodynamically favorable for photogenerated charge separation. TiO_2 exhibits a conduction band (CB) positioned at -4.2 eV and a valence band (VB) at -7.3 eV relative to the vacuum level, corresponding to a bandgap of approximately 3.1 eV. In contrast, WO_3 displays a higher-lying conduction band at -4.1 eV and a valence band at -6.9 eV, with a narrower bandgap of 2.8 eV. This staggered band alignment creates energetic driving forces for electron migration from TiO_2 to WO_3 and hole migration in the opposite direction upon photoexcitation, as indicated by the curved arrows in the diagram.

Upon light illumination, electron-hole pairs are generated within TiO_2 and WO_3 respective band structures. The photogenerated electrons in TiO_2, possess higher energy, due to the more negative conduction band position. They spontaneously transfer to the lower-lying conduction band of WO_3. This electron transfer process is energetically favorable by approximately 0.1 eV and thus provides sufficient driving force for efficient charge separation together with minimized energy losses. Simultaneously, photogenerated holes in WO_3 migrate to the valence band of TiO_2 since it lies at a more negative potential by approximately 0.4 eV. This bidirectional charge transfer effectively spatially separates the photogenerated charge carriers, significantly reducing the probability of electron-hole recombination and extending their lifetimes for participation in electrochemical processes.

The accumulated electrons in WO_3 have been found to play a crucial role in facilitating ammonium ion insertion reactions. The reduction of W^{6+} species to lower oxidation states (e.g., W^{5+}, W^{4+}) through electron injection creates favorable sites for NH_4^+ intercalation into the layered WO_3 structure. This process can be illustrated through the transformation of $W^{6+} + NH_4^+ + e^- \rightarrow (NH_4^+)_xWO_3$. The presence of excess electrons in the WO_3 conduction band not only reduces the activation energy for ion insertion but also enhances

the electronic conductivity of the material. Faster charge transfer kinetics are thus facilitated during the battery operation. The heterojunction interface serves as a critical charge transfer platform that enables the cooperative functioning of both materials in the composite system. At this interface, the band bending creates a built-in electric field that assists in charge separation and prevents back-recombination of separated carriers. The intimate contact between TiO_2 and WO_3 phases ensures efficient charge transfer and meanwhile maintains the structural integrity of both components. The interface also provides additional active sites where both surface adsorption and bulk intercalation mechanisms can operate simultaneously. The enhanced overall capacity of the composite electrode(s) is thus expected.

4.2 Material preparation and characterization

The synthesis of WO_3/TiO_2 composite electrodes employed a sequential fabrication approach. They were designed to achieve optimal morphological control and maximize the heterojunction interface area of such electrodes. The initial step involves the magnetron sputtering of a thin TiO_2 onto the CC substrate. Under selected conditions, a uniform 300 nm thick TiO_2 layer was deposited. The CC substrate provides an excellent conductive framework with a high surface area and mechanical flexibility. The sputtered TiO_2 layer ensures intimate contact with the substrate and establishes a continuous electronic pathway. The method for the electrochemical deposition of WO_3 is the same as that described in the previous chapter. To achieve the desired island-like morphologies, voltage and concentration parameters were further optimized. The morphological evolution of WO_3 deposits was systematically investigated as functions of electrolyte concentration and applied potential. Some typical SEM images of these deposits are demonstrated in **Figure 4.2**. When the concentration of Na_2WO_4 in the precursor solution is spanned from 0.01 M, 0.02 M, to 0.05 M, distinct morphological transitions are noticed, which are believed to directly correlate with nucleation density and growth kinetics. In more detail, when the concentration of tungsten precursor solutions is spanned 0.01 M,

the WO_3 deposits exhibit discrete islands with a high aspect ratio and well-defined crystalline facets. As the concentration increases to 0.02 M, the island density increases while maintaining reasonable separation between individual deposits. Further increase of the concentration up to 0.05 M results in higher nucleation densities with smaller individual islands and increased coverage of the TiO_2 surface. Therefore, this potential-dependent morphological evolution demonstrates the critical role of the concentration of tungsten precursor solution in driving or controlling such deposit characteristics.

It has been found that the applied potential also. affects the features of these deposits. At mild cathodic potentials (e.g., -0.3 V *vs*. SCE), the deposition rate is relatively slow, resulting in larger, well-crystallized WO_3 islands with excellent structural definition. The optimal conditions identified through this systematic study correspond to an applied potential of -0.8 V and 0.01 M precursor concentration, as highlighted by the red dashed box in **Figure 4.2**.

Under these optimal conditions, the WO_3 deposits exhibit uniform island morphology with optimal size distribution (50-200 nm in diameter) and a surface coverage of approximately 60-70% that is expected to maximize active material loading and meanwhile maintain TiO_2 surface accessibility. The application of more negative potential (e.g., from -1.3 V to -2.5 V) leads to faster deposition kinetics but results in less controlled morphologies (e.g., an increased surface roughness and the formation of amorphous phases). Considering the balance between deposition rate and morphological control, careful optimization of this potential thus requires achieving the desired composite architecture. Note that the critical innovation in this synthesis approach lies in the controlled electrochemical deposition of WO_3 in island-like morphologies rather than continuous film formation. This morphological control strategy ensures that both TiO_2 and WO_3 components remain accessible to the electrolyte, have maximum utilization of active materials, and expose efficiently their heterojunction interfaces.

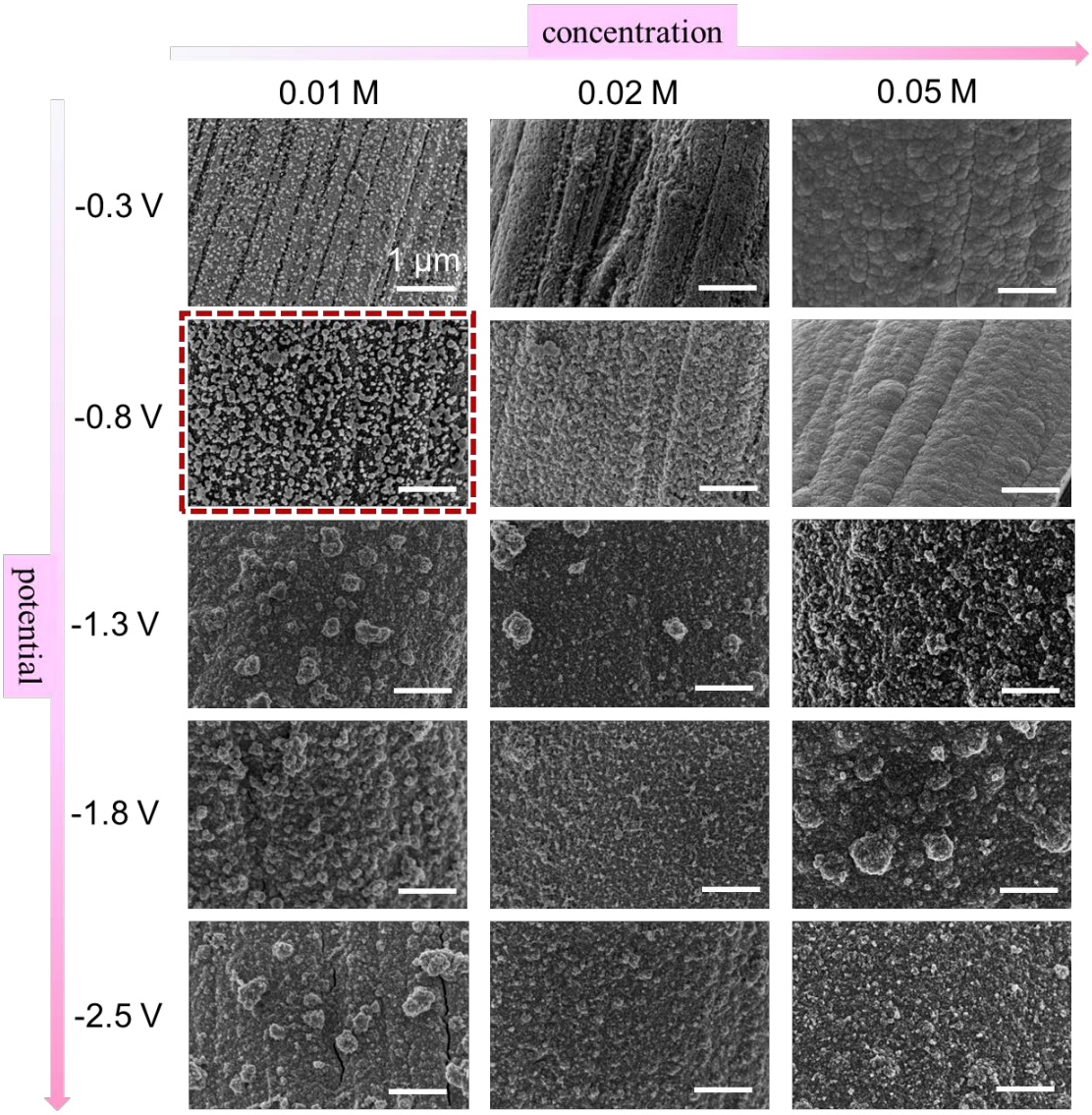


Figure 4.2 Systematic morphological optimization of WO_3 deposited on TiO_2-coated CC substrate, where electrochemical deposition parameters were varied: SEM images of deposited WO_3 when the tungsten precursor concentration was 0.01 M, 0.02 M, and 0.05 M as well as and the applied potential was -0.3 V, -0.8 V, -1.3 V, -1.8 V, and -2.5 V (*vs.* SCE).

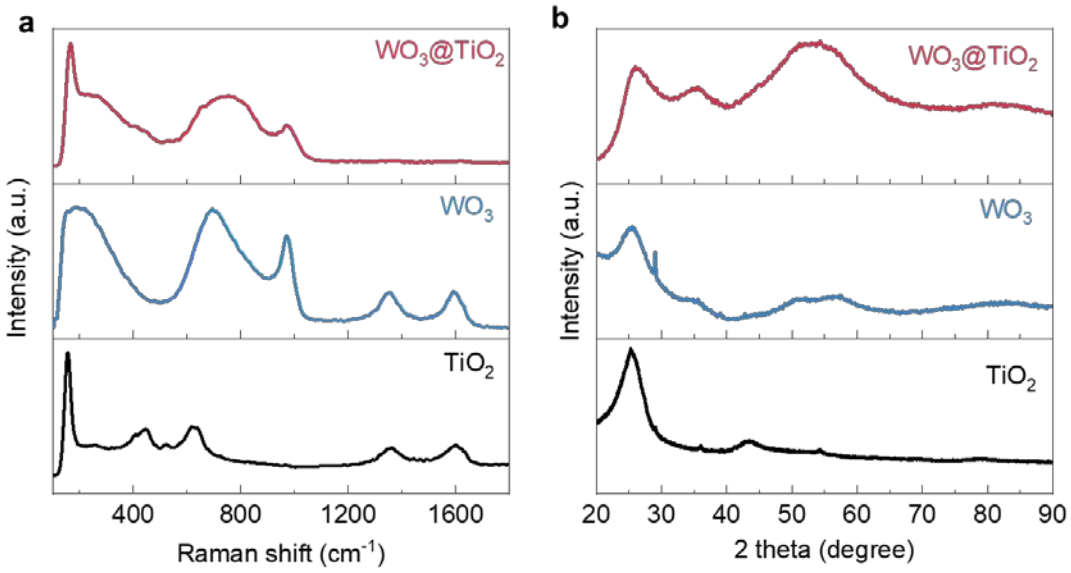


Figure 4.3 Structural characterization of WO_3/TiO_2 composite electrodes: (a) Raman spectra of pristine TiO_2 (black), pure WO_3 (blue), and a WO_3/TiO_2 composite (red); (b) their XRD patterns.

Raman spectra of pristine TiO_2 (black), pure WO_3 (blue), and a WO_3/TiO_2 composite were recorded (**Figure 4.3a**). They confirm the successful formation of both WO_3 and TiO_2 phases in the composite electrode where no significant phase intermixing or secondary compound formation are noticed. The Raman spectrum of pristine TiO_2 exhibits characteristic peaks at 516 cm^{-1} (A_{1g} mode), 639 cm^{-1} (E_g mode), and 197 cm^{-1} (E_g mode), confirming the anatase crystal structure with high phase purity. In Raman spectrum of pure WO_3 reference, distinct vibrational modes are seen at 807 cm^{-1} (corresponding to W-O terminal stretching vibrations), 715 cm^{-1} (attributed to W-O-W bridging modes), and additional peaks in the 200-400 cm^{-1} region (associated with W-O bending vibrations characteristic of the hexagonal WO_3 structure). The Raman spectrum of a $WO_3@TiO_2$ composite represents a superposition of individual component spectra with subtle, but significant modifications. These facts indicate successful formation of a heterojunction. The TiO_2 peaks remain clearly identifiable, but their frequencies shift slightly and their intensities are varied. It suggests interfacial interactions of WO_3 with TiO_2 deposits, again the formation of a heterojunction. The WO_3 characteristic peaks are

well-preserved, confirming that the crystalline WO_3 is successfully produced using electrochemical deposition method. There is no significant structural degradation, either. Importantly, the absence of new peaks in intermediate frequency ranges indicates that unwanted secondary phases (e.g., tungsten titanate compounds) are not formed during this synthesis process, preserving the intended electronic structure of the heterojunction. XRD analysis (**Figure 4.3b**) was also applied to reveal the structural characteristics of both individual components and their composite materials. The XRD pattens of the pristine TiO_2 show a broad diffraction feature centered around 25°, which corresponds to the (101) reflection of anatase TiO_2. Its significant broadening indicates a predominantly amorphous or nanocrystalline structure rather than a well-crystallized material. This amorphous nature is known to be typical for TiO_2 films prepared by magnetron sputtering at relatively low substrate temperatures, where insufficient thermal energy limits long-range crystalline ordering. Similarly, the pure WO_3 reference exhibits broad, diffuse diffraction features in the 20-30° range that correlate with the expected positions of hexagonal WO_3 reflections. The absence of sharp, well-defined peaks indicates that the electrochemically deposited WO_3 possesses largely amorphous character. The broad nature of these features suggests small crystallite sizes or significant structural disorder. The XRD patterns of a WO_3/TiO_2 composite include an even broader and more diffuse hump, reflecting the combined contributions from both amorphous components. The overlapping of the broad features from TiO_2 and WO_3 results in a single, extended diffraction envelope that spans the angular range where both materials contribute. This amorphous character in the composite does not preclude electrochemical activity, as demonstrated by the preserved local structural features revealed through their Raman spectroscopic analysis. This composite thus probes short-range order that remains intact even in predominantly amorphous materials.

4.3 Electrochemical and photoelectrochemical performance

The photoelectrochemical behavior of pristine TiO_2 electrodes was systematically evaluated to figure out the baselined photocatalytic activity that contributes to the performance of composite electrodes.

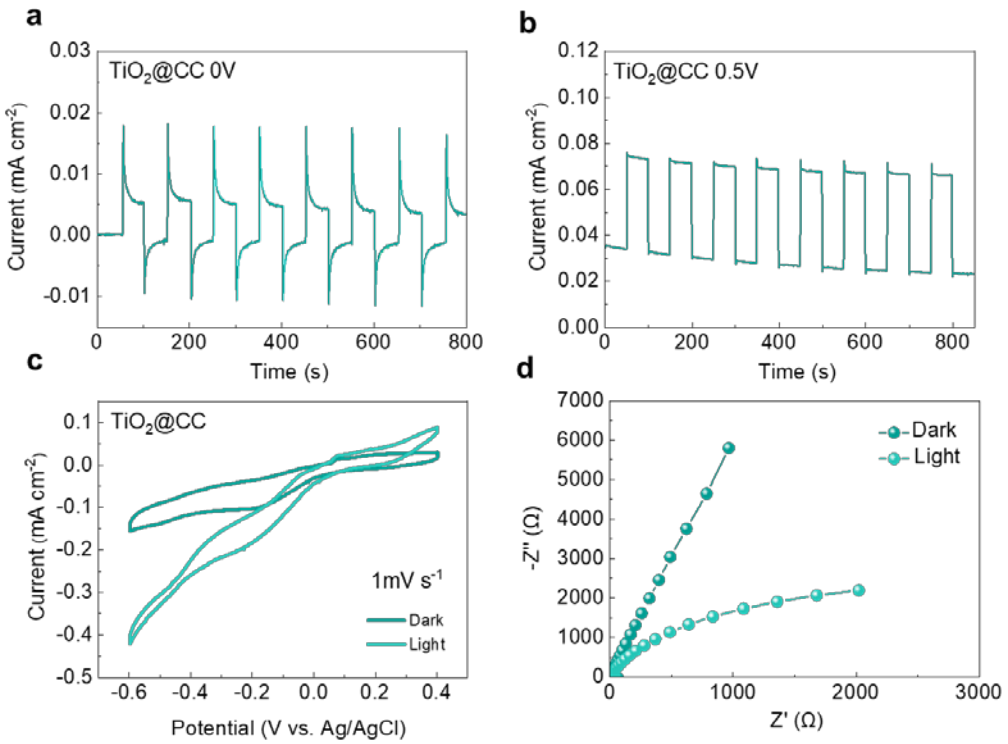


Figure 4.4. Photoelectrochemical characterization of pristine TiO_2 electrodes: *I–t* curves at (a) a bias potential of 0 V (*vs*. OCP) and (b) 0.5 V (*vs*. OCP) under dark and illumination conditions; (c) Cyclic voltammograms comparison between dark and light conditions at a scan rate of 1 mV s^{-1}; (d) Comparison of Nyquist plots under dark and light conditions.

Figure 4.4a shows the chronoamperometric results under chopped light illumination, where provide direct evidence of the photo response characteristics. They are also informative in terms of the stability of the TiO_2 component under electrochemical conditions that are relevant to ammonium ion storage applications. For example, at a bias potential of 0 V (*vs*. SCE), the TiO_2 electrode exhibits characteristic photocurrent transients with rapid response during the light on/off cycles. The photocurrent density reaches approximately 0.018 mA cm^{-2} under illumination, representing a substantial

enhancement over the minimal dark current observed in the absence of light. The photocurrents are reproducible across multiple on/off cycles, demonstrating the stability of the photoelectrochemical response and the absence of significant photo corrosion or surface degradation during the operation. The sharp rise and decay profiles indicate efficient charge separation and collection processes, A rise of such currents as function of times only on the order of seconds suggests good charge transport properties within the TiO_2 film.

Under a bias potential of 0.5 V (*vs*. OCP), the photocurrent response (**Figure 4.4b**) is significant enhanced, reaching approximately a photocurrent of 0.075 mA cm^{-2} together with improved stability when compared to the zero-bias condition. The applied anodic potential provides additional driving force for the photogenerated charge separation since a created depletion layer facilitates electron-hole separation and reduces recombination loss. The sustainable photocurrent levels throughout the measurement period indicate excellent photoelectrochemical stability and efficient charge transfer to the electrode/electrolyte interface. The rectangular-like current profiles during illumination periods suggest that the electrode reaches rapidly the steady-state and can also maintain stable performance throughout the illumination cycles. In addition, CV test (**Figure 4.4c**) show a significant increase in cathodic current density under light illumination compared to that in the dark condition, particularly at more negative potentials (e.g., –0.6 V). This enhancement can be ascribed to the efficient driving of photogenerated electrons by the applied negative bias. In this way, their injection into the electrolyte is accelerated and the reduction reaction is boosted. In contrast, the current difference obtained under light and dark conditions is less pronounced around 0 V and +0.4 V. Namely, in these cases the driving force for electron transfer or hole-driven oxidation reactions is insufficient, leading to negligible photo enhancement.

EIS was performed to probe the interfacial charge-transfer and ion-transport characteristics of the TiO_2 electrode under both dark and illuminated conditions. These results are shown as their Nyquist plots (**Figure 4.4d**). In the dark, the Nyquist plot

exhibits a nearly vertical line at low frequencies, indicating that capacitive charging behavior with severely hindered faradaic reactions dominate the features of electrode/electrolyte interface. This behavior reflects the limited availability of free carriers in TiO_2 under dark conditions and therefore a blocked interface and predominant double-layer capacitance response. Upon light illumination, the shape of the related Nyquist plot changes dramatically. The low-frequency branch tilts away from the vertical direction towards ~45°, which is a hallmark of Warburg-type impedance associated with ion diffusion. Such transition indicates that photoexcitation activates interfacial charge-transfer processes. It is believed that photogenerated electrons reduce the kinetic barriers for faradaic reactions, enabling actual electrochemical conversion to occur at the electrode surface. Consequently, ion transport through the electrolyte and within the porous electrode structure becomes a new rate-limiting step, manifesting as a diffusion-controlled response in the Nyquist plots. Although the apparent low-frequency response under illumination appears more resistive, this behavior still reflects the activation of faradaic charge storage pathways that are absent in the dark. In summary, illumination completely alters the interfacial properties of TiO_2: the electrode transitions from a purely capacitive, kinetically blocked state in the dark to an electrochemically active, diffusion-limited state under light. This photo-activation of faradaic charge storage thus provides a mechanistic explanation for the enhanced electrochemical performance of TiO_2-based composite electrodes.

4.4 photoelectrochemical performance towards ammonium ion storage

Since the growth parameters of WO_3 electrodes have been re-optimized, their capacitive performance was re-evaluated prior to composite studies. The CV and GCD measurements were performed in 1 M NH_4Cl aqueous electrolyte. As shown in **Figure 4.5a**, the cyclic voltammogram exhibits quasi-rectangular shapes with an increasing enclosed area when a higher scan rate is applied, an indication of typical pseudocapacitive

behavior with stable ion insertion/extraction processes. The nearly symmetric shape of the cyclic voltammograms confirms highly reversible charge storage.

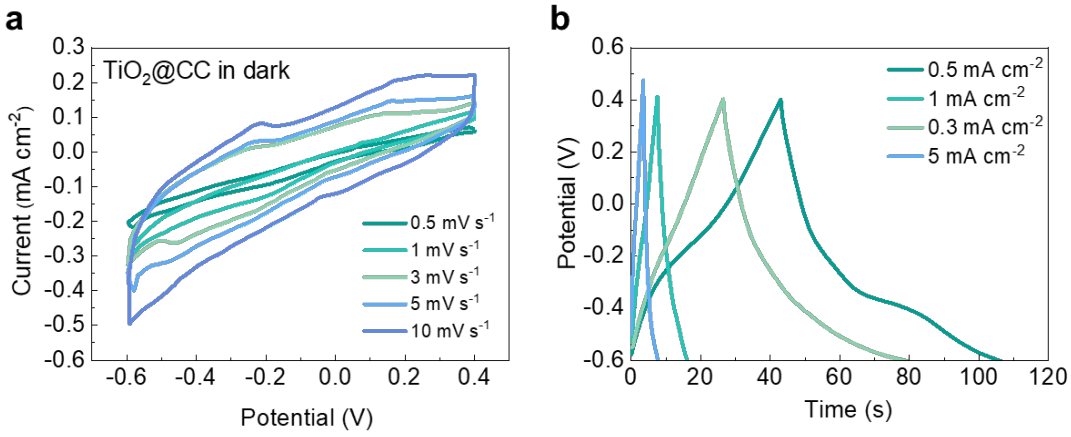


Figure 4.5. (a) Cyclic voltammograms of a WO_3 electrode at different scan rates (e.g., 0.5, 1, 3, 5, 10 mV s^{-1}), and (b) corresponding GCD curves at different current densities (e.g., 0.5, 1, 3, 5 mA cm^{-2}).

Meanwhile, the GCD curves at various current densities (**Figure 4.5b**) display triangular and symmetric shape without obvious voltage plateaus, confirming the capacitive-dominated behavior of the WO_3 electrode. An increase of the current density leads to the shortened discharge time while the curves retain good linearity, demonstrating excellent rate capability of such an electrode. Compared to TiO_2, the WO_3 electrode shows pronounced NH_4^+ storage activity even in the absence of illumination, highlighting its intrinsic pseudocapacitive properties. The photoelectrochemical response of a WO_3 electrode at different bias potentials was examined when the light is on and off with a time interval of 800 s (**Figure 4.6**). At a bias potential of 0 V (*vs*. OCP), the electrode exhibits a pronounced cathodic photocurrent of approximately –0.003 mA cm^{-2} (**Figure 4.6a**), indicating that photogenerated electrons are efficiently injected into the electrolyte. This phenomenon arises because a bias potential of 0 V is slightly negative relative to the flat-band potential of the *n*-type WO_3. Upon illumination, the electron quasi-Fermi level shifts upward, generating an effective cathodic overpotential. The injected electrons drive NH_4^+ insertion into the WO_3 lattice, resulting in a net reductive current. The initial

negative spikes are attributed to both double-layer/surface-state charging and fast $W^{6+} \rightarrow W^{5+}$ trapping processes.

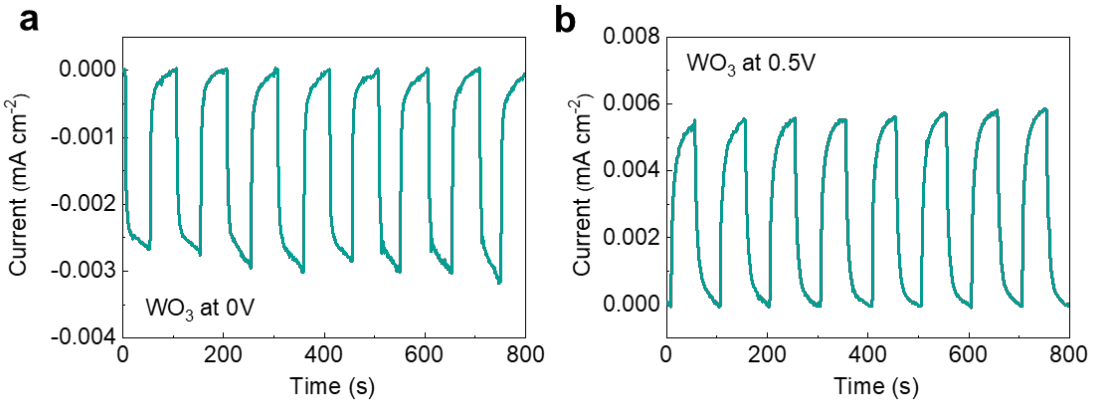


Figure 4.6. Photoelectrochemical response of a WO_3 electrode when chopped illumination is on and off with an interval of 800 s: *I–t* curves at a bias potential of (a) 0 V (*vs*. OCP) and (b) 0.5 V (*vs*. OCP) in 1 M NH_4Cl electrolyte.

The subsequent quasi-steady current is obviously limited by ion diffusion. Importantly, the cathodic photocurrent response is stable and reproducible over multiple cycles. This fact confirms the interfacial stability of WO_3 under photoelectrochemical conditions and further highlights its capability for the sustained electron transfer processes that are associated with NH_4^+ reduction and insertion. Once the bias potential is enhanced to +0.5 V (*vs*. OCP) (**Figure 4.6b**), the photocurrent polarity reverses to the anodic direction. This is because the applied bias in this case is more positive than the flat-band potential. In other words, it depletes the surface region and enables photogenerated holes to migrate toward the electrode/electrolyte interface. As a result, the cathodic NH_4^+ insertion channel is suppressed and then the response is dominated by hole-driven oxidation of surface –OH/H_2O species. The transient exhibits a sharp positive spike, followed by decay to a steady-state value. It thus reflects a fast space-charge charging process, of which kinetics are limited by hole transfer and reactant supply. Compared with the photocurrent intensity obtained at a bias potential of 0 V, it becomes smaller. This is consistent with slower hole-transfer kinetics and stronger/faster surface recombination in WO_3.

The comparison of photoelectrochemical response of a WO_3 electrode with a TiO_2 electrode leads one to believe that WO_3 shows more moderate photocurrent magnitudes. Meanwhile it exhibits different directional characteristics, stemming from its distinct electronic structure and band positioning. The lower photocurrent density of a WO_3 electrode suggests that WO_3 can participate in photoelectrochemical processes. Note that its primary value in energy storage applications lies more in its bulk intercalation capability rather than surface photocatalytic activity. This observation highlights the importance of complementary design strategy where WO_3 provides capacity while TiO_2 provides photocatalytic enhancement.

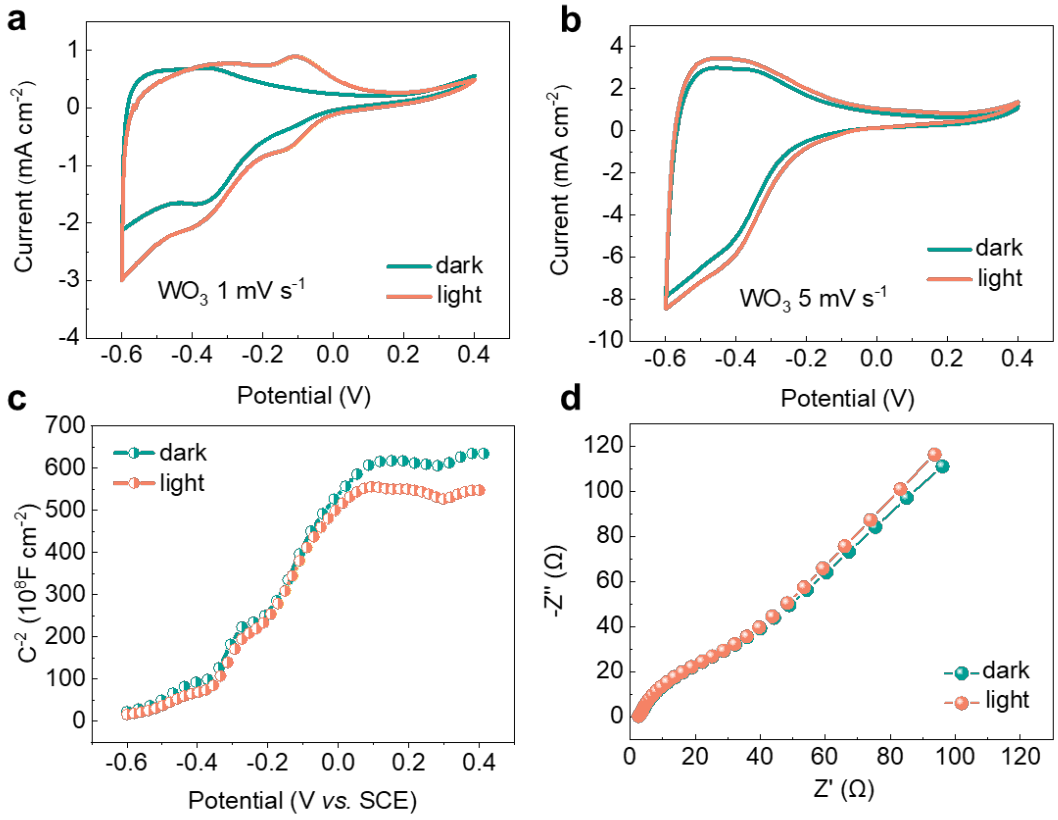


Figure 4.7. (a, b) Cyclic voltammograms of a WO_3 electrode in dark and under illumination at different scan rates, (c) Mott–Schottky plots of WO_3 electrode in dark and under illumination, (d) rate performance comparison in dark and under illumination.

The photoelectrochemical behavior of WO_3 was systematically investigated (**Figure 4.7**) to elucidate the effect of light illumination on NH_4^+ storage kinetics at a very slow scan

rate (e.g., 1 mV s^{-1}) when the light is on and off. Under dark conditions the cyclic voltammogram shows distinct redox features with a current density of approximately ±3 mA cm^{-2} (**Figure 4.7a–b**). This results from significant faradaic activity associated with insertion and extraction processes of NH_4^+. The broad cathodic peak centered around -0.3 V (*vs*. Reference electrode) corresponds to NH_4^+ insertion into the WO_3 lattice with a concurrent reduction reaction of W^{6+} to lower oxidation states. The corresponding anodic features represent the reverse extraction process. Upon light illumination, the electrochemical response is notably enhanced, namely much increased current density and more defined redox features. This light-enhanced performance demonstrates that photoactivation improves the kinetics of NH_4^+ storage processes. The overall current under illumination is approximately 120-130% higher compared to that under dark conditions, indicating moderate but consistent photo-enhancement effects that contribute to improved electrode performance.

At higher scan rates (5 mV s^{-1}, **Figure 4.7b**), the current densities increase proportionally while the characteristic redox features are maintained, demonstrating good rate capability for NH_4^+ storage. The preservation of redox peaks at higher scan rates indicates that the insertion/extraction kinetics are sufficiently fast to high power density, unlike the purely capacitive behavior observed for a TiO_2 electrode. The enhancement effect under illumination persists at higher scan rates, confirming that photoactivation provides consistent benefits across different operating conditions. The interfacial electronic properties were further probed by means of Mott–Schottky analysis under dark and illuminated conditions (**Figure 4.7c**). Both curves exhibit a positive slope, the nature of a *n*-type semiconductor. The slope of the $1/C^2–V$ relationship decreases under illumination, indicating a higher donor density (N_d), which is attributed to the generation of additional free carriers. Furthermore, the flat-band potential (E_{FB}) shifts slightly toward the negative direction when light is on, reflecting reduced band bending and more favorable energetics for electron injection into the electrolyte. These results confirm that

illumination not only increases the carrier density, but also improves band alignment, thereby facilitating faster interfacial charge transfer.

The EIS measurements (**Figure 4.7d**) provide further evidence of this effect in a quantitative way. The Nyquist plots recorded under dark conditions show a large semicircle, corresponding to a high R_{ct} at the WO_3 electrode/electrolyte interface. Upon illumination, the semicircle diameter decreases significantly, indicating pronounced reduction of R_{ct}. This reduced R_{ct} directly demonstrates that photogenerated carriers can enhance the interfacial charge transfer kinetics by lowering the activation barrier for NH_4^+ insertion/extraction reactions. In addition, the slopes of the low-frequency tails become steeper under illumination, suggesting improved ion diffusion and capacitive response.

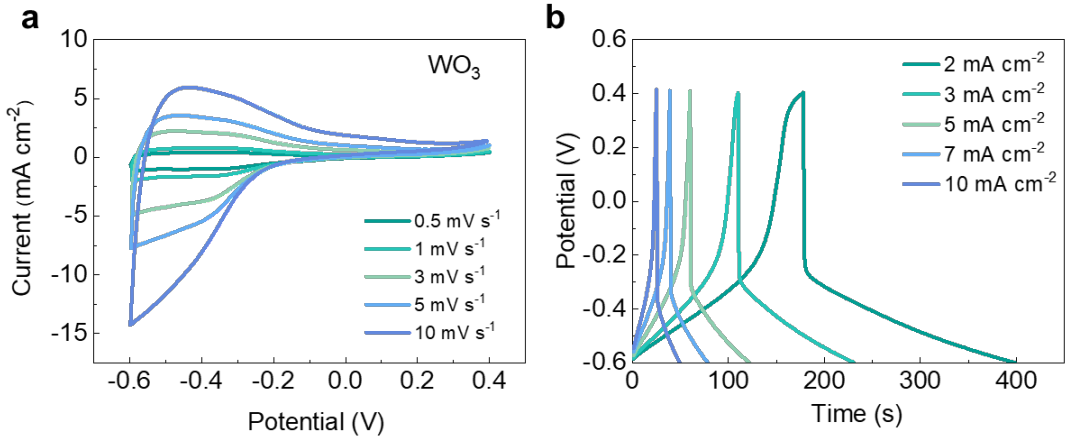


Figure 4.8. (a) Cyclic voltammograms of a WO_3 electrode at different scan rates, (b) its GCD profiles at different current densities.

The intrinsic electrochemical storage capability of a WO_3 electrode toward NH_4^+ was further evaluated under dark conditions. The cyclic voltammograms at different scan rates (**Figure 4.8a**) exhibits a pair of broad redox peaks, obviously from the reversible NH_4^+ insertion/extraction process coupled with the W^{6+}/W^{5+} redox transition. The redox peaks remain visible even at high scan rates, although they become slightly broadened and shift to positive values, indicating that the NH_4^+ insertion is diffusion-limited but still highly reversible. The nearly linear increase of peak current as a function of scan rate suggests that a WO_3 electrode stores charge predominantly *via* pseudocapacitive processes rather

than pure diffusion-limited intercalation. This is consistent with the tunnel-type structure that facilitates fast ion transport as expected.

The GCD profiles of a WO_3 electrode recorded at various current densities (**Figure 4.8b**) also support these observations. The discharge curves exhibit distinct potential plateaus, which are associated with the CV redox peaks and reflect the phase transformation between WO_3 and H_xWO_3-like bronzes formed upon NH_4^+ insertion. Importantly, these plateaus are retained even at high current densities, demonstrating that a WO_3 electrode possesses good rate capability. The minor increase in the IR drops and polarization with an increase of the current density reflects moderate kinetic limitations, yet the electrode maintains stable charge–discharge behavior.

In short, the CV and GCD results confirm that a WO_3 electrode exhibits intrinsic pseudocapacitive NH_4^+ storage performance, with reversible redox activity and favorable kinetics. These findings contrast sharply with a TiO_2 electrode, which only shows negligible NH_4^+ storage. All these thus highlight the critical role of WO_3 as the active host material in subsequent WO_3/TiO_2 composite systems.

The electrochemical performance of WO_3/TiO_2 composite electrodes was then studied using CV and GCD methods. As expected, this composite electrode demonstrates remarkable enhancement than both a WO_3 electrode and a TiO_2 electrode, where synergistic heterojunction effects are believed to exist. For example, the comparison of cyclic voltammogram at a scan rate of 5 mV s^{-1} (**Figure 4.9a**) reveals that the composite displays the largest enclosed area and the most pronounced redox features, of which peak current densities reach ±12 mA cm^{-2}, much bigger compared to ±8 mA cm^{-2} for a pristine WO_3 electrode and negligible current densities of below ±2 mA cm^{-2} for a TiO_2 electrode. The composite exhibits significantly reduced peak separation and higher peak currents compared to pristine WO_3, evidencing its lower polarization and accelerated charge-transfer kinetics. This improved response arises from fast electron pathways and enhances ionic accessibility on the WO_3/TiO_2 heterointerface. In more detail, the Type II band

alignment creates built-in electric fields that facilitate charge separation and reduce activation barriers for redox processes.

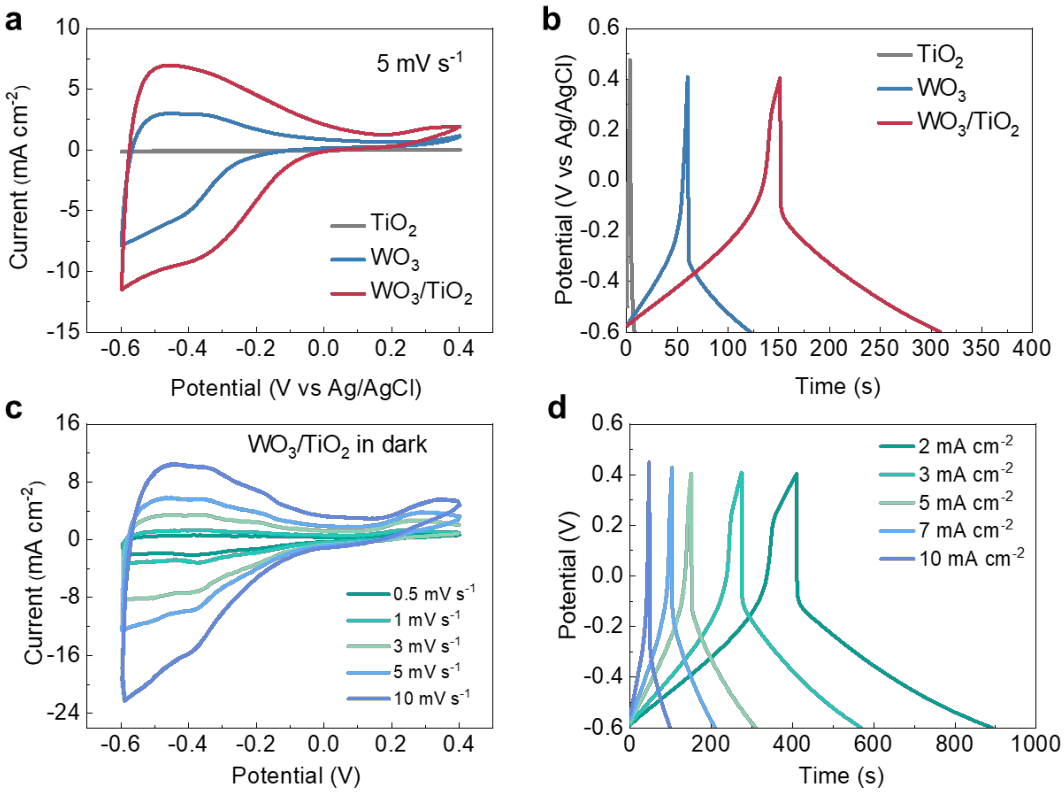


Figure 4.9 (a) Comparison of the Cyclic voltammograms of TiO_2, WO_3, and WO_3/TiO_2 electrodes. (b) The comparison of their GCD curves at a fixed current density. (c) Cyclic voltammograms of the WO_3/TiO_2 composite at different scan rates. (d) GCD curves of the WO_3/TiO_2 composite at different current densities.

Related GCD curves (**Figure 4.9b**) demonstrate superior capacity performance of this composite electrode since it delivers the longest discharge time (250 s) among three electrodes and also clearer voltage plateaus compared to a WO_3 electrode (150 s) and minimal capacity for a TiO_2 electrode. Since the well-defined plateaus reflect higher areal capacity and more efficient utilization of redox-active sites, the WO_3/TiO_2 heterojunction thus facilitates better access to the WO_3 intercalation sites. Its smaller initial *IR* drop compared to a pristine WO_3 electrode indicates a reduced internal resistance and improved electronic/ionic transport pathways. This cooperative mechanism probably

involves the role of both WO_3 that provides bulk intercalation sites and TiO_2 that serves as a kinetic facilitator. Eventually charge transfer efficiency is enhanced and more preferential electron injection pathways into WO_3 are created.

The cyclic voltammogram of the composite electrode were recorded at different scan rates (**Figure 4.9c**). The redox peaks remain discernible across 0.5-10 mV s^{-2}, revealing exceptional rate capability of this electrode. One can see that there is a diffusion-assisted pseudocapacitive mechanism instead of a purely surface-limited charging process, demonstrating a successful combination of high-capacity bulk intercalation with fast surface kinetics. The unchanged peak shape across the applied scan rates confirms efficient ion transport pathways within the composite architecture. For example, TiO_2 probably creates additional nucleation sites for NH_4^+ insertion and further provides electronic facilitation that minimizes kinetic limitations.

The GCD curves (**Figure 4.9d**) recorded in the different current densities (e.g., from 2 to 10 mA cm^{-2}) show evident discharge plateaus that are maintained over the entire current range, again confirming robust redox kinetics. The capacity retention validates the synergistic rate capability, where it is believed that WO_3 provides abundant redox sites while TiO_2 furnishes rapid electron extraction routes and improved interfacial wettability. They jointly mitigate transport bottlenecks.

The performance enhancement on this composite architecture is likely achieved through multiple mechanisms: i) electronic-level heterojunction band alignment reduces charge transfer barriers; ii) interfacial-level intimate contact ensures rapid charge equilibration, and iii) structural-level combination of WO_3 bulk storage with TiO_2 kinetic advantages results in electrodes exhibiting both high capacity and excellent rate capability. In conclusion, the photo-enhanced electrochemical performance of the WO_3/TiO_2 composite electrodes demonstrates the successful integration of photocatalytic and electrochemical functionalities through heterojunction engineering.

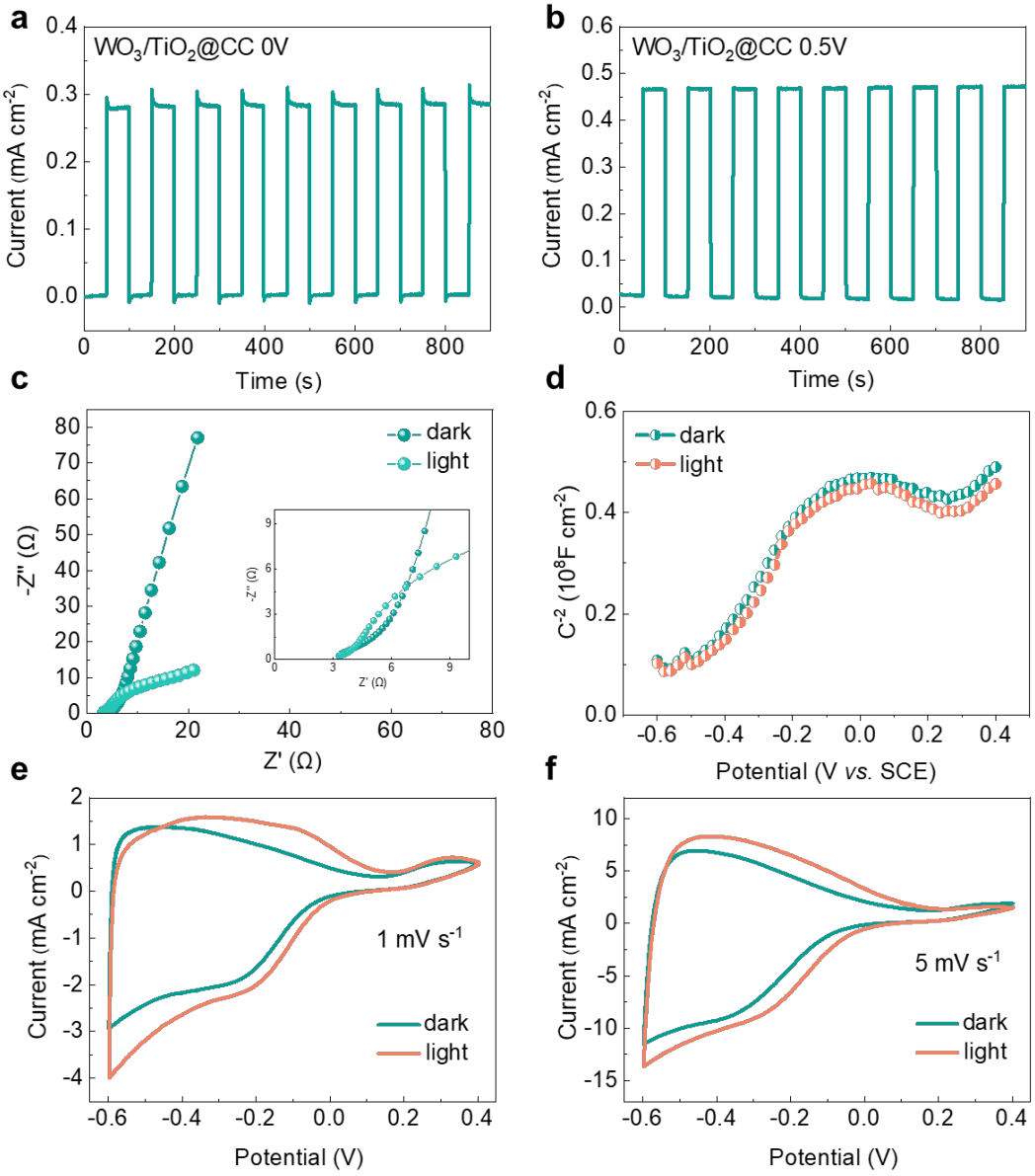


Figure 4.10 Photoelectrochemical characterization of WO_3/TiO_2 composite electrodes in dark and under light illumination: (a, b) *I–t* curves at a bias of +0.5 V and 0 V (*vs*. SCE) under chopped illumination, (c) Nyquist plots, (d) Mott–Schottky plots, (e, f) Cyclic voltammograms.

The photoelectrochemical response of such composite electrodes was investigated under chopped light illumination. Their *I-t* curves (**Figures 4.10a,b**) reveal exceptional photocurrent generation that significantly exceeds the individual component responses. At a bias potential of 0 V (*vs*. SCE), the composite generates the photocurrent density of

approximately 0.28 mA cm^{-2} with excellent reproducibility across multiple light on/off cycles, while at a bias of 0.5 V the response increases up to 0.47 mA cm^{-2}. These values demonstrate the potential-dependent nature of photo response on this heterojunction interface. The sharp rise and decay profiles indicate both efficient charge separation and collection processes. The anodic photocurrent direction confirms that holes become the dominant charge carriers participating in interface reactions, as expected for the Type II heterojunction model. In this case electrons migrate from TiO_2 to WO_3 and holes accumulate in TiO_2.

Further EIS analysis provides quantitative evidence to elucidate the effect of illumination on interfacial charge transfer. As shown in the Nyquist plot (**Figure 4.10c**), the semicircle diameter in the high-frequency region becomes slightly larger under illumination, indicating an increase in charge-transfer resistance (Rct, light > Rct, dark). This counterintuitive trend may arise from light-induced changes in surface band bending or carrier trapping, which partially hinder charge transfer at the applied potential. The unchanged high-frequency intercept confirms that the Rs remains nearly constant. Therefore, the impedance variation specifically reflects interfacial modifications induced by illumination rather than bulk electrolyte effects.

Mott-Schottky analysis of the composite electrodes was conducted in dark and under light illumination (**Figure 4.10d**) with an aim to reveal their electronic properties. From the replotted relationship between C^{-2} and the applied potential, the insights into the density of states and band bending characteristics of these composite electrodes were gained. Upon illumination, the slope decreases markedly, signifying an apparent increase in donor density. For example, a higher carrier concentration is probably due to photogenerated electrons. Simultaneously, the E_{FB} undergoes a slight negative shift under illumination, reflecting reduced band bending at the semiconductor/electrolyte interface. This reduction of WO_3/TiO_2 composite electrodes in interfacial barrier lowers the energetic threshold for electron transfer into the electrolyte, facilitating more efficient electron injections. These findings are consistent with the transient photocurrent results,

where light illumination significantly enhances electron-driven NH_4^+ insertion kinetics under similar bias conditions.

The comparison of cyclic voltammograms of these composite electrodes between under dark and light illumination (**Figures 4.10e,f**) helps one to obtain more direct evidence to prove photo-enhancement of ammonium ion storage processes on these electrodes. For example, at a scan rate of 1 mV s^{-1}, the composite electrode shows substantial electrochemical activity sunder dark conditions. The current density can reach to ±2.5 mA cm^{-2}, indicating its baseline capacity for NH_4^+ storage. Upon light illumination, the current density increases significantly up to approximately ±3.5 mA cm^{-2}. This 40% enhancement spans the entire potential window. Moreover, the light-enhanced curves exhibit more defined redox features and reduced peak separation. Namely, the kinetics for NH_4^+ insertion and extraction processes are improved. At higher scan rates (e.g., 5 mV s^{-1}), the photo-enhancement becomes even more pronounced. The current density is increased from ±8 mA cm^{-2} in dark to ±12 mA cm^{-2} under light illumination. These values clearly demonstrate that photocatalytic activation particularly benefits high-rate performance where kinetic limitations are typically dominated. The mechanistic origin of these photo-enhancements is supposed to lie in heterojunction-driven charge separation, where photogenerated electrons migrate from TiO_2 to WO_3 and they participate in W^{6+} reduction reactions. In this way favorable NH_4^+ insertion sites are created and meanwhile electronic conductivity of WO_3 is enhanced. Simultaneously, the holes in TiO_2 generate reactive oxygen species that modify surface chemistry and improve electrolyte wetting. The spatial charge separation reduces recombination losses and extends carrier lifetimes, enabling sustained photocatalytic activation of this composite electrode. The wavelength-dependent response reflects the combination of UV absorption by TiO_2 with the activity of WO_3 in visible light range. The interface states also provide additional charge separation pathways. These results validate the heterojunction design for integrating high storage capacity with photocatalytic enhancement, establishing a foundation for solar-assisted energy storage systems.

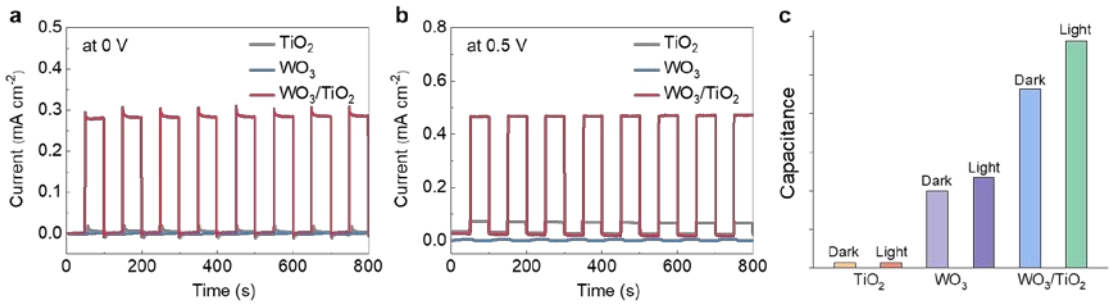


Figure 4.11 Photoelectrochemical response of pristine TiO_2, pristine WO_3, and WO_3/TiO_2 composite electrodes: (a) *I*–*t* curves at a bias potential of 0 V (*vs*. OCP); (b) *I*–*t* curves at a bias of 0.5 V (*vs*. OCP); (c) Capacitance comparison under dark and light conditions for all three materials

In the transient photocurrent curves (**Figure 4.11a**), one can gain insight into the light response of the three electrode systems. At a bias potential of 0 V (*vs*. OCP), the pristine TiO_2 electrode shows negligible photocurrent, due to its wide bandgap (≈3.2 eV) and poor visible-light absorption capability under the experimental illumination conditions. The electrode remains essentially inactive, confirming its intrinsic limitation as a single-component NH_4^+ storage material. The pure WO_3 electrode does exhibit a measurable but modest photocurrent response. It is only approximately 0.005 mA cm^{-2}. Compared with the TiO_2 electrode, this bigger current benefits from its narrower bandgap (≈2.6–2.8 eV) that allows visible-light harvesting. However, the photocurrent of the WO_3 electrode shows rapid decay after each light illumination, indicating severe recombination losses and poor long-term carrier utilization. By contrast, the WO_3/TiO_2 composite demonstrates a dramatically stronger and more stable photocurrent response. It is as high as 0.02 mA cm^{-2}, and its decay is significantly reduced during repeated light on–off cycles. These reflect improved charge separation and suppress recombination, originating from the synergistic operation of the heterojunction of the WO_3/TiO_2 composite electrode.

When an anodic bias of 0.5 V (*vs*. OCP), the performance differences become even more pronounced (**Figure 4.11b**). Again, the TiO_2 electrode shows modest photocurrent enhancement and the WO_3 electrode exhibits limited anodic response. The composite

electrode demonstrates unexceptional photocurrent, reaching 0.47 mA cm^{-2}. It is enhanced with a factor of approximately 10-fold over the TiO_2 electrode and 15-fold over the WO_3 electrode. In other words, the heterojunction architecture on the WO_3/TiO_2 composite electrode creates new pathways for charge separation and utilizes far exceed capabilities of either individual material. The consistent rectangular photocurrent profiles across all materials confirm stable photoelectrochemical behavior, while their magnitude difference highlights the unique advantages of this WO_3/TiO_2 composite system.

The mechanistic origin of this dramatic enhancement is explained as follows. It lies in the complementary electronic properties and efficient charge separation that is enabled by the Type II heterojunction on this WO_3/TiO_2 composite system. In the composite, photogenerated electrons generated from TiO_2 migrate to the lower-lying conduction band of WO_3, while holes migrate in the opposite direction, creating spatial separation that minimizes recombination losses. This charge separation mechanism converts the predominantly cathodic response of WO_3 and the limited response of TiO_2 into a substantial anodic photocurrent in the composite. Consequently, the heterojunction alters the photoelectrochemical behavior beyond simple material combination.

The capacitance analysis (**Figure 4.11c**) reveals the dramatic and quantitative differences in electrochemical activity under both dark and light conditions. Under dark conditions, the TiO_2 electrode shows a minimal capacitance, consistent with its poor electrochemical activity for ammonium ion storage. The WO_3 electrode exhibits a moderate capacitance, reflecting its intercalation capability. The TiO_2/WO_3 composite demonstrates enhanced capacitance even under dark conditions, indicating that the heterojunction formation in the TiO_2/WO_3 electrode improves the baseline electrochemical performance through enhanced charge transfer pathways and improved ionic accessibility.

Under light illumination, the capacitance enhancements reveal the full potential of each material system. The TiO_2 electrode shows modest improvement, reflecting its limited intrinsic storage capability despite photoactivation, while the WO_3 electrode exhibits moderate enhancement, consistent with improved surface kinetics under illumination.

The composite, however, demonstrates exceptional capacitance enhancement that substantially exceeds both individual components. Therefore, the photocatalytic activation in the heterojunction TiO_2/WO_3 system creates synergistic effects that amplify both the surface activity from TiO_2 and the bulk storage capacity from WO_3.

4.5 Conclusions

This chapter comprehensively validates the rational design strategy for the TiO_2/WO_3 composites, where the intrinsic limitations of individual components—poor storage capacity for TiO_2 and limited photoactivity for WO_3—have been effectively overcome through heterojunction engineering. The formation of a type-II TiO_2/WO_3 junction facilitates directional charge transfer and spatial separation of photogenerated carriers, leading to enhanced interfacial kinetics and suppressed charge recombination.

Structural and spectroscopic characterizations confirm the intimate interface coupling between WO_3 and TiO_2, as evidenced by coherent lattice contact and well-aligned band structures. Electrochemical analyses further demonstrate that the composite electrode exhibits a significantly reduced charge-transfer resistance and improved pseudocapacitive response under illumination, achieving superior areal capacitance, rate capability, and cycling stability compared with either single component.

The photo-enhanced behavior can be ascribed to the synergistic effects between the TiO_2 conduction band and the WO_3 valence band, which together broaden the light absorption range and create built-in electric fields to promote carrier migration. This efficient charge utilization mechanism directly contributes to the higher energy density and improved long-term reversibility observed in the composite.

Overall, the results establish the TiO_2/WO_3 heterojunction as a promising platform for the development of photo-assisted aqueous energy storage systems. The insights gained here regarding interfacial band alignment, charge-separation dynamics, and illumination-enhanced kinetics also provide a conceptual and methodological foundation for the next-stage design of more advanced composites.

5 WO_3/BDD p-n junction for light-assisted energy storage

Light-assisted energy storge has been becoming an innovative and efficient approach for the development of various energy devices. For them, one of the key components is the employed electrode(s), for example numerous heterointerfaces and junctions have been paid extensive attention. Building upon the successful demonstration of WO_3/TiO_2 heterojunctions for enhanced ammonium ion storage, this chapter explores an approach utilizing boron-doped diamond (BDD) as the composite partner for WO_3, aiming to represent a significant advancement in electrode material design.

The motivation for such innovative systems stems from diamond's exceptional properties that complement and potentially surpass those of conventional semiconductor materials such as its ultra-wide bandgap (5.5 eV), exceptional chemical stability, superior thermal conductivity, and unique electrochemical characteristics[141–143]. When appropriately doped with boron, diamond transforms from an insulator to a *p*-type semiconductor with remarkable electrochemical activity. If it is properly integrated with other *n*-type semiconductors (e.g., WO_3) novel heterojunction designs will be created and some unprecedented opportunities are expected[144,145].

The combination of WO_3 with BDD creates a *p-n* junction configuration that fundamentally differs from the Type II heterojunction as observed in WO_3/TiO_2 systems. This *p-n* junction design leverages the intrinsic electric field established at the interface between *p*-type BDD and *n*-type WO_3[146], providing enhanced charge separation efficiency and directional electron transport. It is thus expected that this *p-n* junction can dramatically improve both photoelectrochemical and energy storage performance[147–149]. Moreover, the wide bandgap of diamond extends the operational stability under harsh electrochemical conditions. Furthermore, its exceptional thermal and electrical conductivity ensures efficient heat dissipation and electron transport throughout the composite structure[150]. Last but the least, chemical inertness and electrochemical stability of diamond enable operation across extended potential windows without degradation,

addressing one of the primary limitations encountered in conventional composite electrodes[144,151].

On the other hand, WO_3 presented in this junction is capable of or provides active sites for NH_4^+ storage. Together with BDD (thanks to its superior electronic properties and electrochemical stability), this junction will create a synergistic platform that is extremely suitable for the development of next-generation photo-assisted energy storage devices. Therefore, this chapter summarizes the results about comprehensive electrochemical and photoelectrochemical characterization, the assembly and evaluation of complete photo-assisted AIHS devices. These devices are believed to feature enhanced performance such as extended cycle life and improved power characteristics. Such a study will be helpful to establish fundamental design principles of diamond-based composite electrodes and meanwhile to demonstrate their practical energy storage applications.

5.1 Working principle of WO_3/BDD photo-enhanced electrode

The design of the *p*-*n* junction between WO_3 and BDD represents a fundamental departure from conventional heterojunction approaches since it leverages the unique electronic properties of both materials to create an optimized interface for photo-assisted ammonium ion storage. Its energy storage mechanism is illustrated in its energy band alignment (**Figure 5.1a**), where demonstrates the formation of a *p*-*n* heterojunction for charge separation and enhanced electrochemical activity. The electronic structure of the WO_3/BDD composite features a strategically engineered band alignment. In more detail, the *n*-type WO_3 exhibits a conduction band positioned at -4.2 V and its valence band at -6.9 V relative to the vacuum level, corresponding to a bandgap of approximately 2.7 eV. In contrast, the *p*-type BDD displays a significantly deeper valence band at -5.8 V with a conduction band at -0.3 V, reflecting its ultra-wide bandgap of 5.5 eV. Such band configuration thus can create a substantial valence band offset of 1.1 eV and a conduction band offset of 3.9 eV. In other words, strong driving forces will be established across the heterojunction interface of the WO_3/BDD junction for charge carrier separation.

In more detail, the *p*-*n* junction formation at the WO_3/BDD interface creates an intrinsic electric field that fundamentally alters the charge transport dynamics compared to the Type II heterojunction observed in the WO_3/TiO_2 systems. Upon illumination, electrons photogenerated in WO_3 migrate toward the more positive conduction band of BDD, while holes generated in BDD are driven toward the higher-lying valence band of WO_3. This charge separation mechanism is energetically favorable by approximately 3.9 eV for electron transfer and 1.1 eV for hole transfer. This system thus provides substantial thermodynamic driving forces that minimize recombination losses and extend carrier lifetimes for participation in electrochemical processes.

The unique advantage of this *p*-*n* junction design lies in the exceptional properties of BDD that complement the electrochemical activity of WO_3. The ultra-wide bandgap of diamond ensures high transparency across the visible spectrum and meanwhile diamond features exceptional chemical and electrochemical stability under harsh operating conditions. The heavy boron doping creates a quasi-metallic surface layer that exhibits excellent electronic conductivity. BDD can thus effectively function as a current collector. Namely it can facilitate rapid electron extraction from the WO_3 component during ammonium ion insertion processes. Additionally, the high thermal conductivity of diamond materials ensures efficient heat dissipation during high-rate electrochemical operation[152,153]. The charge separation efficiency in the WO_3/BDD p-n junction is expected enhanced by the built-in electric field established at the interface since there exists a big difference in Fermi levels between the *p*-type and *n*-type materials. This built-in field creates a depletion region that facilitates charge separation even in the absence of external bias or photoexcitation. This is a baseline enhancement to electrochemical kinetics of NH_4^+ storage. Under illumination, the photovoltaic effect generated by the *p*-*n* junction provides additional driving force for charge separation, while the wide bandgap of diamond minimizes parasitic light absorption that might compete with WO_3 photoactivity. Furthermore, the chemical inertness of diamond ensures that the heterojunction interface remains stable during extended electrochemical cycling,

preventing the formation of undesired interfacial phases that typically limit the performance of conventional composite electrodes.[154–156]

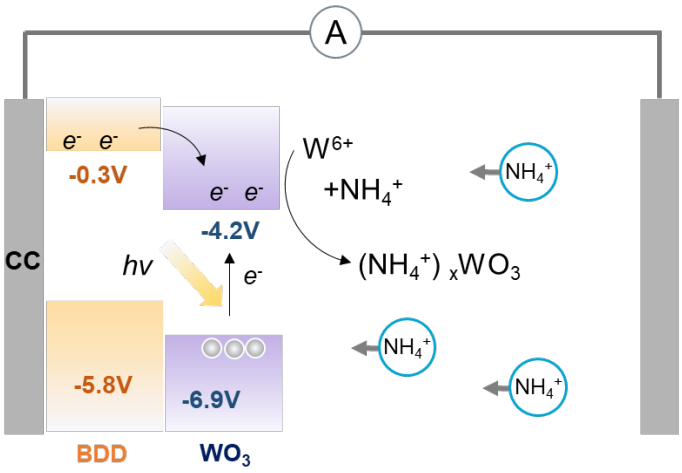


Figure 5.1 Schematic illustration of the band alignment and charge transfer in the WO_3/BDD heterojunction.

5.2 Characterization of WO_3/BDD composites

Several WO_3/BDD composites were prepared according to the process described in experimental session. **Figure 5.2** shows the SEM images of as-prepared materials in different stages. From them one can clearly the structural evolution: from BDD coatings and pristine WO_3 nanocrystals to the integrated WO_3/BDD@CC composite. The BDD layer deposited on the CC substrate (**Figure 5.2a,b**) is continuous and uniform across the whole surface of carbon fibers. These nanocrystalline diamond domains are typically in the range from 150 to 250 nm in size. The homogeneous distribution of diamond crystallites ensures consistent electrical conductivity across the CC substrate, while the dense packing minimizes the exposure of the bare CC in touch with the electrolyte to air. This uniform deposition was then employed as a stable and conductive scaffold for subsequent WO_3 growth. In contrast, pristine WO_3 (**Figure 5.2c,d**) exhibits irregular nanocrystalline grains and its average lateral size is approximately 200–300 nm. It distributes relatively uniformly but accompanied by localized clusters of up to 500 nm.

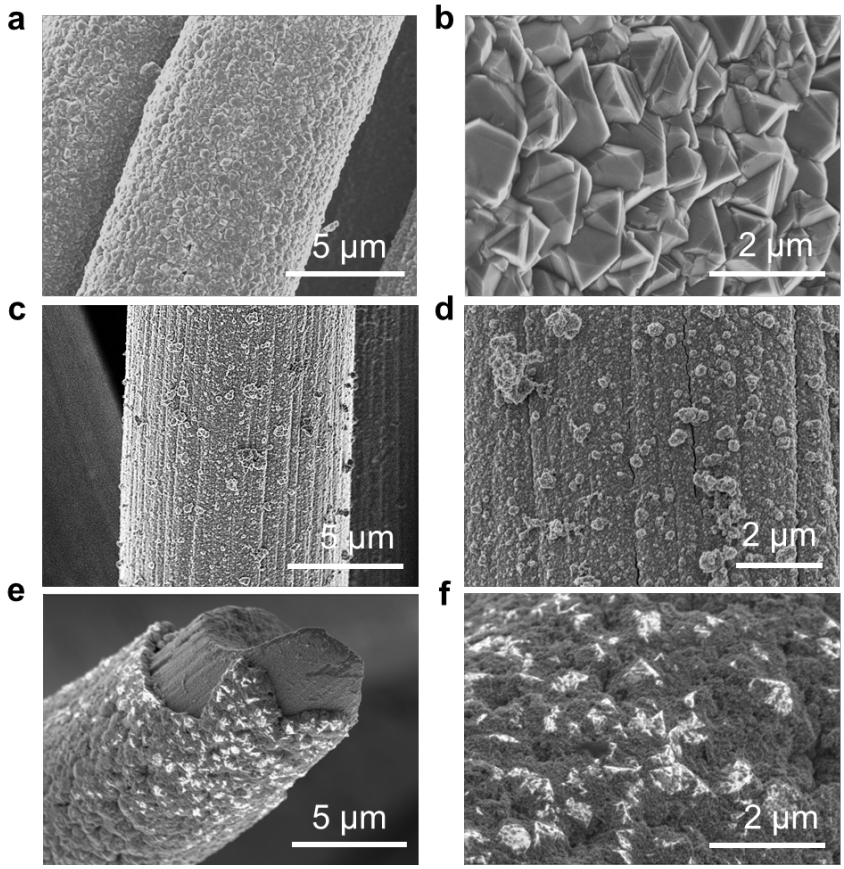


Figure 5.2 SEM images of (a,b) pristine BDD film on a CC substrate, (c,d) pristine WO_3 nanocrystals, and (e,f) a WO_3/BDD composite.

The WO_3/BDD composite (**Figure 5.2e,f**) shows a remarkable refinement of WO_3 morphology. The WO_3 nanoparticles are evenly dispersed across the BDD framework where no obvious aggregation is noticed. Importantly, both WO_3 nanocrystals and BDD domains remain simultaneously exposed to the electrode surface. The former provides abundant redox-active sites for NH_4^+ storage, while the latter contributes to rapid electron transport and structural integrity. This morphological evolution highlights the synergistic benefits of the composite design. Namely, the uniform and conductive BDD coating provides a stable current-collecting backbone, while the reduction in WO_3 particle size eliminates aggregation-related limitations and enhances the active surface area. The co-existence of exposed BDD and WO_3 phases at the electrode/electrolyte interface ensures efficient *p–n* junction coupling and maximized participation of both materials in photo-

assisted electrochemical processes, ultimately enabling enhanced charge separation, ionic diffusion, and overall energy storage performance.

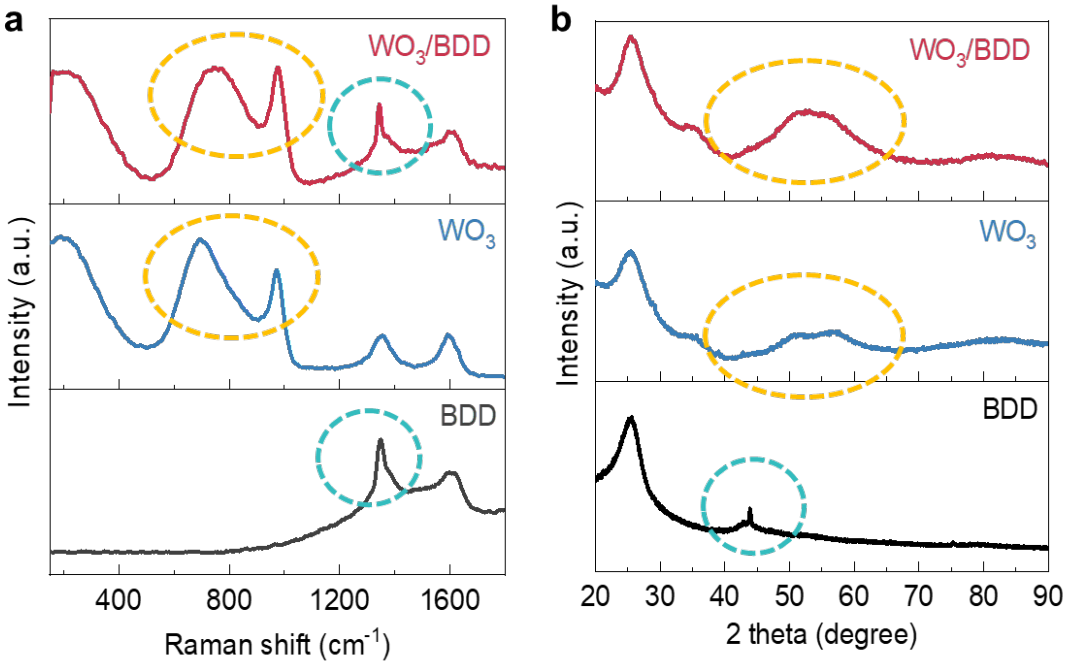


Figure 5.3 (a) Raman spectra of pristine BDD, pristine WO_3, and a WO_3/BDD composite. (b) XRD patterns of pristine WO_3 and a WO_3/BDD composite.

The Raman analysis of the pristine materials and the WO_3/BDD composite (**Figure 5.3a**) provides further insights into their structural characteristics. The Raman spectrum of the pristine BDD exhibits a characteristic sharp diamond peak at 1332 cm^{-1}, confirming the successful deposition of crystalline diamond on the CC substrate. The slight broadening of this peak and the appearance of weak bands around 500–1200 cm^{-1} can be attributed to boron incorporation, consistent with the *p*-type doping. For pristine WO_3, distinct Raman modes are observed at ~270, 325, 715, and 805 cm^{-1}, which are assigned to either bending or stretching vibrations of the W–O bonds in monoclinic WO_3. These vibrational features confirm the presence of well-crystallized WO_3 with a long-range order. In the WO_3/BDD composite, all these mentioned WO_3 Raman peaks are retained, but with noticeable shifts (2 – 4 cm^{-1}) and broadening relative to the pristine sample. Such changes indicate a reduction in the WO_3 crystallite size, in agreement with related observations in

the SEM images, where the WO_3 nanoparticles are refined to ~80–150 nm in the composite. The coexistence of the BDD diamond peak at 1332 cm^{-1} and the WO_3 vibrational modes demonstrates that both phases remain structurally intact and simultaneously exposed in the hybrid electrode. Compared to pristine WO_3, the narrower and more symmetric line shapes are seen, an indication of the suppression of excessive WO_3 agglomeration. In short, the WO_3/BDD composite has enhanced structural homogeneity and improved interfacial integration.

Additional XRD analysis of the WO_3/BDD composites (**Figure 5.3b**) was conducted in order to reveal the crystalline nature of these composite materials. In the XRD patterns, there shows the characteristic diamond diffraction peak at approximately 44°. It corresponds to the (111) reflection, though its intensity is relatively low, probably due to the thin film nature and boron doping effects. The pure WO_3 exhibits broad diffraction features, characteristics of nanocrystalline or partially amorphous WO_3, consistent with the electrochemical deposition conditions. The patterns of the WO_3/BDD composite are from the contributions of both phases. The diamond peak is clearly identifiable alongside the WO_3 features, confirming the coexistence of both materials without the formation of secondary phases and significant interfacial reactions that compromise the intended electronic properties of the heterojunction.

5.3 Electrochemical performance of the WO_3/BDD composites

Several electrochemical methods have been utilized to examine the performance of the WO_3/BDD composites. **Figure 5.4** shows the *i*-*t* curves of BDD under illumination, where a measurable photo response signal is clearly seen, albeit relatively weak. For example, with a bias potential of 0 V (*vs*. OCP) (**Figure 5.4a**), the BDD electrode demonstrates a modest photocurrent response with a current density of approximately 0.003 mA cm^{-2}. Notably, the photocurrent response decays gradually, which is perhaps due to both charge accumulation at the BDD surface under the zero-bias conditions and the influence of surface states. As a wide-bandgap semiconductor material (5.5 eV), the

intrinsic photo response of BDD is inherently limited under visible light excitation, primarily relying on defect states and surface states that are introduced by boron doping to participate in the photoelectrochemical conversion process.

Upon the application of a +0.5 V positive bias (**Figure 5.4b**), the photoelectrochemical behavior of BDD undergoes significant enhancement. The photocurrent density increases five folds and is up to approximately 0.015 mA cm^{-2}. Moreover, the response stability is dramatically improved, exhibiting ideal rectangular wave response characteristics. This remarkable improvement can be attributed to the optimization of electrochemical kinetics at the BDD surface under positive bias. The applied bias facilitates effective separation and transport of photogenerated holes to the electrode surface, thereby reducing charge recombination losses.

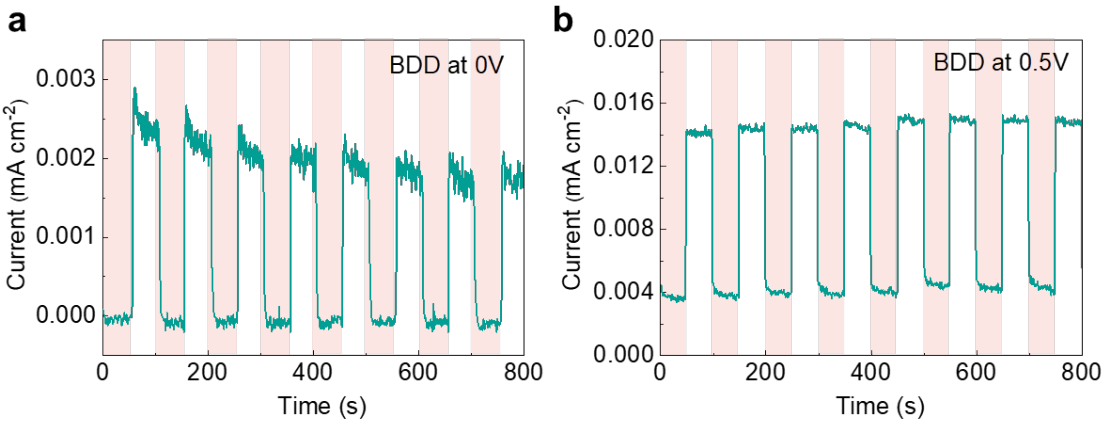


Figure 5.4 *I–t* curves of BDD under illumination and dark at a bias of 0 V and +0.5 V (*vs*. OCP).

Throughout the entire testing period, the photocurrent response maintains high consistency without observable decay or fluctuation, establishing a foundation for providing long-term stable electron transport pathways in composite electrodes. From an energy band structure perspective, the enhanced photoelectrochemical activity of BDD under positive bias validates its suitability as the p-type component in p-n heterojunctions. In the subsequent WO_3/BDD composite system, this potential-dependent

photoelectrochemical behavior will complement the n-type WO_3, achieving more efficient photogenerated charge separation through the built-in electric field.

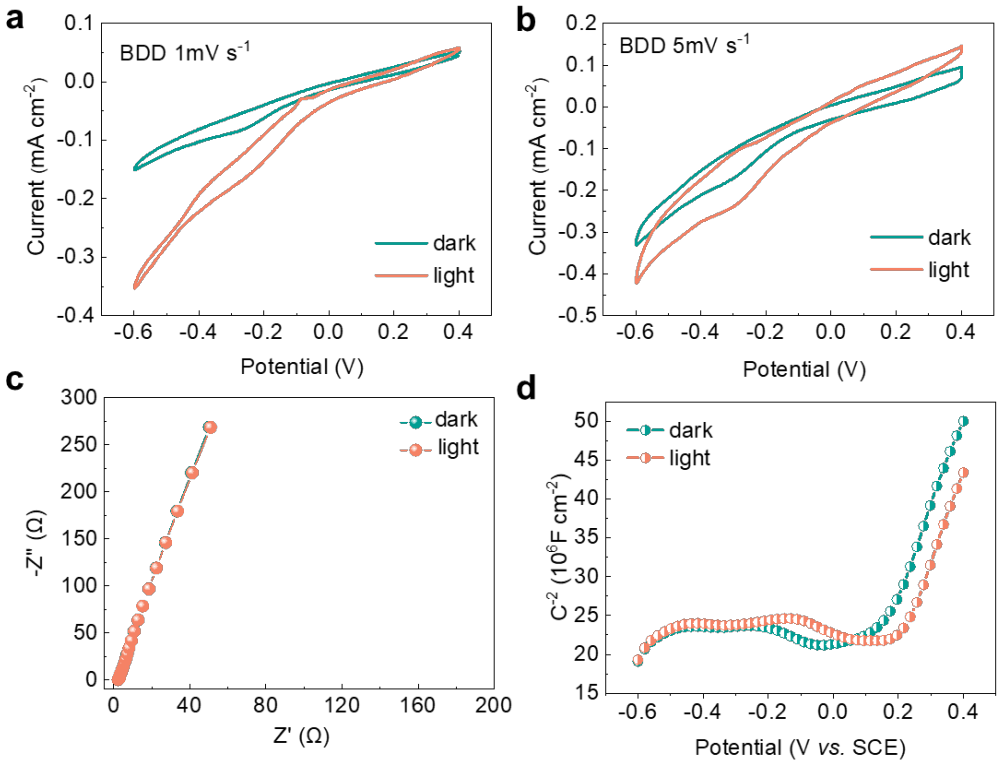


Figure 5.5 Electrochemical characterization of a BDD electrode: (a,b) Cyclic voltammograms at a scan rate of 1 mV s^{-1} and 5 mV s^{-1}, (c) Nyquist curves and (d) Mott-Schottky plots under dark and illuminated conditions.

The cyclic voltammograms of the BDD electrode reveal distinct electrochemical behavior under dark and illuminated conditions. At a low scan rate like 1 mV s^{-1} (**Figure 5.5a**), a pronounced enhancement in cathodic current, particularly in the negative potential region is observed under illumination compared when the light is off. This significant increase of this current is due to the accumulation of photogenerated electrons at the BDD surface, which promote reduction reactions and/or facilitate charge storage processes. The extended time scale at low scan rates allows sufficient opportunity for photogenerated charge carriers to participate in electrochemical processes, leading to the observed cathodic current enhancement. This behavior is similar with that observed in the TiO_2

electrode, where photogenerated electrons similarly enhance reduction processes at negative potentials. At a higher scan rate like 5 mV s^{-1} (**Figure 5.5b**), this enhancement factor of this cathodic becomes much weaker. The reduction of such photo response is because the rate of photogenerated electron production becomes slower in a short time (namely during a faster potential sweep). The Cyclic voltammogram are then similar under dark and illuminated conditions. Meanwhile, the related Nyquist plots under dark and illuminated conditions are nearly identical (**Figure 5.5c**), where minimal differences are found in the charge transfer resistance. This phenomenon is primarily because on BDD there is almost no ammonium ion insertion/extraction processes occurring. Similar size of the semicircles indicates that BDD serves mainly as conductive support rather than an active material for ion storage.

Although BDD is intrinsically a *p*-type semiconductor, the Mott–Schottky plots (Figure **5.5d**) exhibit positive slopes, which are typically associated with *n*-type behavior. This apparent contradiction arises from the heavy boron doping level in the present samples, which renders the depletion region extremely thin and results in quasi-metallic surface conduction. Moreover, surface states and Fermi-level pinning at the diamond/electrolyte interface further distort the space-charge capacitance response, producing an effective *n*-type-like signature. Similar observations have been widely reported for heavily doped BDD electrodes[157,158], highlighting that the Mott–Schottky method can be applied to analyze interfacial electrostatics rather than the intrinsic bulk doping type in such systems.

Figure 5.6a shows the cyclic voltammograms of a BDD electrode recorded at different scan rates. At lower scan rates (e.g., 0.5 - 1 mV s^{-1}), the cyclic voltammograms feature relatively regular rectangular shapes with very low current densities. The message behind is that BDD has essentially no capacity for NH_4^+ adsorption or insertion. In other words, BDD functions primarily as an inert current collector rather than an active material for ammonium ion storage. As the scan rate increases (e.g., up to 5 or 10 mV s^{-1}), polarization becomes evident and significant, particularly in the cathodic region where current density increases substantially. This polarization effect can be attributed to the electrolysis of the

weakly acidic NH_4Cl electrolyte at higher scan rates. The enhanced cathodic current at higher scan rates likely corresponds to hydrogen evolution from NH_4^+ reduction ($NH_4^+ + e^- \rightarrow NH_3 + {}^1/_2H_2$) and/or direct water reduction. From the GCD curves (**Figure 5.6b**), one can see the non-triangular discharge profiles and extremely short discharge times across all current densities. In other words, BDD is not a suitable platform for the NH_4^+ insertion/extraction. The observed electrochemical response likely originates from a minimal double-layer capacitance at the BDD/electrolyte interface as well as some electrolyte decomposition reactions at lower current densities.

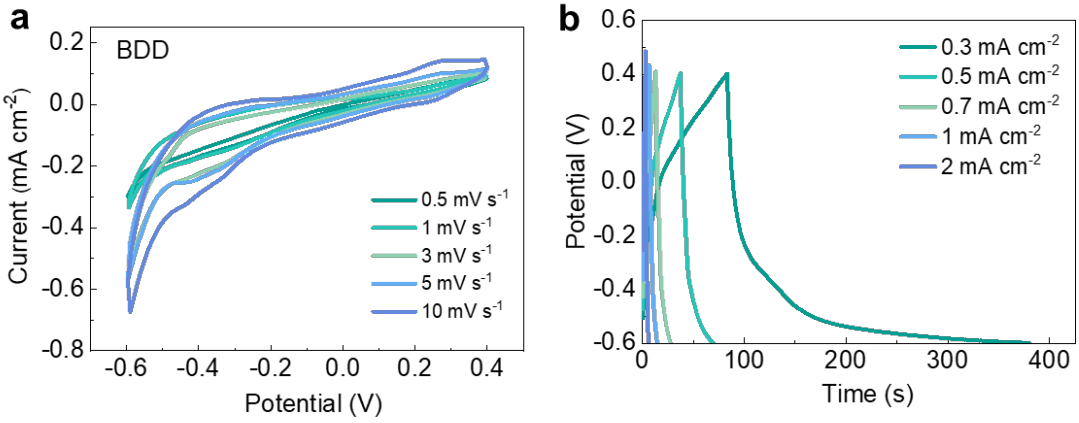


Figure 5.6 Electrochemical characterization of a BDD electrode in 1 M NH_4Cl electrolyte: (a) Cyclic voltammograms at different scan rates. (b) GCD curves at various current densities.

The electrochemical performance of the WO_3/BDD composite electrode was then evaluated in order to verify the synergistic effect between WO_3 and BDD. **Figure 5.7** presents the electrochemical behavior of a WO_3/BDD electrode under dark conditions. Compared to individual BDD and WO_3 electrodes, the composite exhibits significantly improved current response in recoded CVs (**Figure 5.7a**) and also well-preserved GCD profiles with longer discharge times and lower polarization (**Figure 5.7b**). Such difference highlights the role of BDD in facilitating charge transfer and stabilizing the WO_3 nanostructure.

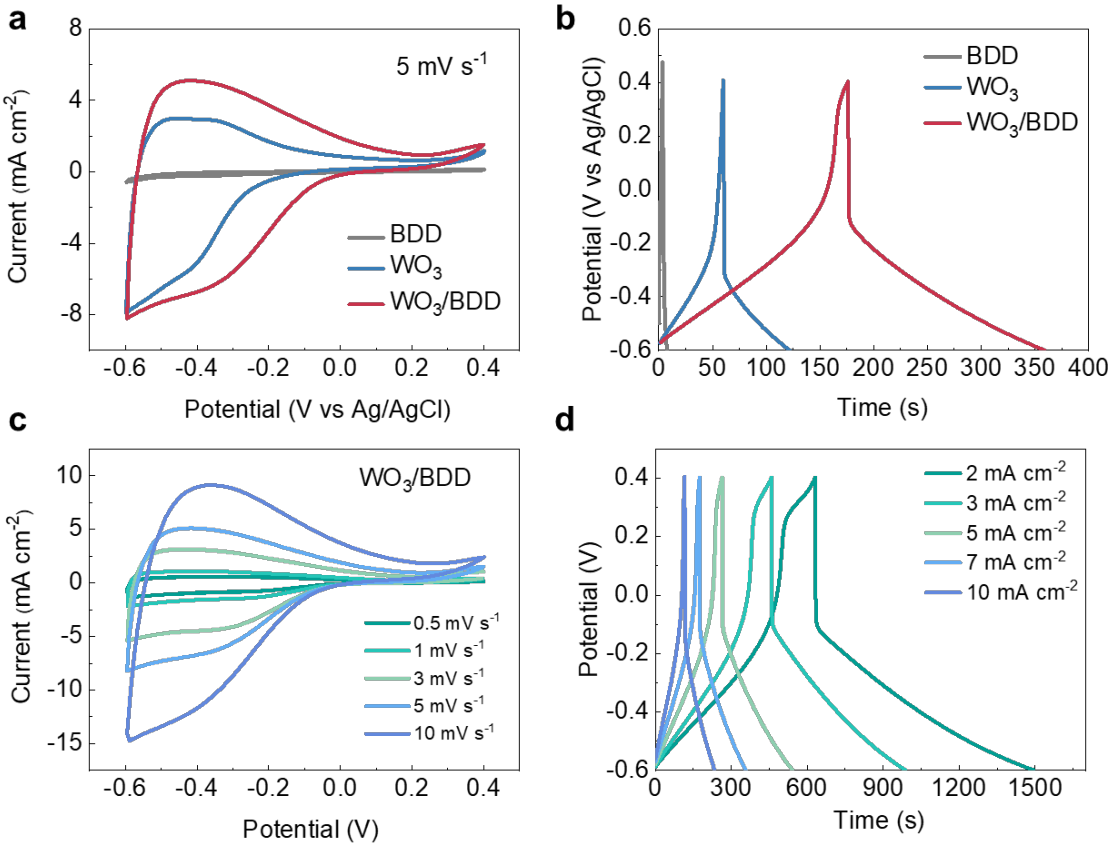


Figure 5.7 Electrochemical performance of WO_3, BDD, and WO_3/BDD electrodes under dark conditions: (a) Cyclic voltammograms at 5 mV s^{-1}, (b) GCD curves at a current density of 5 mA cm^{-2}, (c) Cyclic voltammograms of the WO_3/BDD electrode at different scan rates, and (d) its GCD curves at different current densities.

In addition, the Pristine WO_3 electrode exhibits well-defined redox peaks associated with NH_4^+ insertion/extraction. However, the current density is relatively low, due to its intrinsically poor conductivity. The BDD electrode shows nearly featureless capacitive behavior with negligible currents, reflecting its role as conductive support rather than an active host for ammonium ion storage. In contrast, the WO_3/BDD composite displays significantly enlarged redox peaks as well as a broader enclosed area. Compared to a pristine WO_3 electrode, peak separation is also reduced. This indicates that the conductive BDD backbone not only enhances electron transport but also lowers electrode polarization, thereby accelerating the intercalation kinetics of a WO_3 electrode. At the

same current density, a pristine WO_3 electrode shows relatively short discharge times and noticeable *IR* drops, consistent with its sluggish charge transfer and high internal resistance. The BDD electrode alone delivers negligible capacitance. The WO_3/BDD electrode demonstrates substantially longer discharge durations and highly symmetric charge/discharge profiles with minimal *IR* drop, confirming both improved capacity and enhanced reversibility. These results clearly show that the composite integrates the faradaic storage capability of WO_3 with the superior conductivity of BDD, yielding a synergistic improvement in electrochemical performance in terms of ammonium ion storage. For example, even in the absence of illumination, the WO_3/BDD electrode still delivers superior capacitive behavior and reversible NH_4^+ storage, providing a robust foundation for further investigation of its photo-assisted performance.

Subsequently, the photo response of this WO_3/BDD composite material was examined. At a bias potential of 0 V (*vs*. OCP) (**Figure 5.8a**), the WO_3/BDD composite exhibits a photocurrent density of approximately 0.005 mA cm^{-2}, which is excellently stable throughout the measurement period, as seen from the consistent rectangular wave responses and a minimal decay even over 20 light-on/off cycles. The enhanced performance becomes even more pronounced at a bias potential of +0.5 V (*vs*. OCP) (**Figure 5.8b**), where the photocurrent densities go up to about 0.020 mA cm^{-2}. This photocurrent response remains almost unchanged with sharp on/off transitions and throughout the extended measurement period.

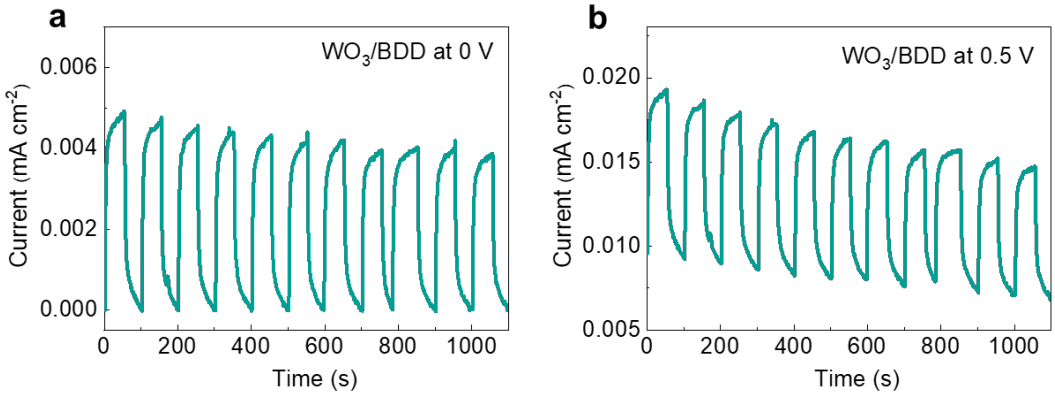


Figure 5.8 *I-t* curves of WO_3/BDD composite under illumination and dark conditions at a bias potential of (a) 0 V and (b) +0.5 V (*vs*. OCP).

The effect of light exposure on these composite materials was investigated during ammonium ion storage. The CV responses of a WO_3/BDD electrode under both dark and illuminated conditions display well-defined redox peaks that are associated with the reversible NH_4^+ insertion/extraction (**Figure 5.9a,b**). Clearly, the overall current response is markedly enhanced across all scan rates upon illumination. This result indicates that photogenerated electrons actively participate in the redox process and increase the availability of reduced tungsten sites for the NH_4^+ storage.

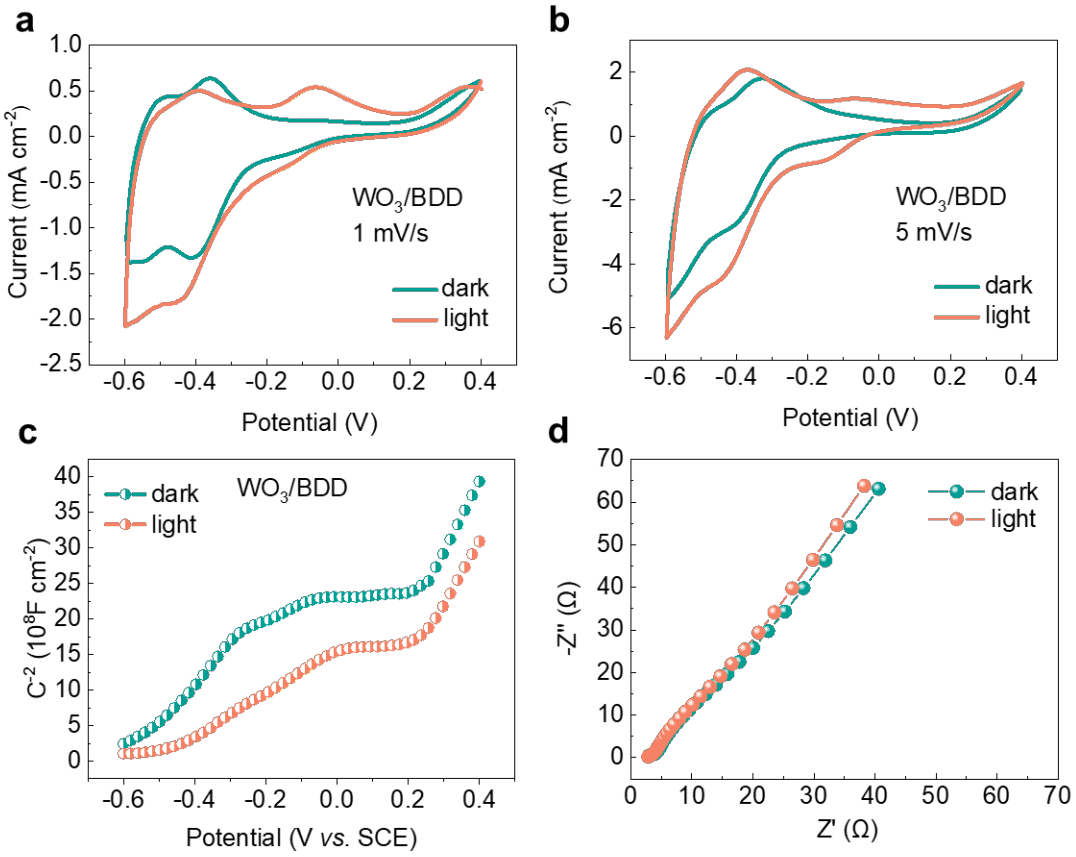


Figure 5.9 Electrochemical characterization of the WO_3/BDD composite when the light is off (dark) and on (light): Cyclic voltammogram at (a) 1 mV s^{-1} and (b) 5 mV s^{-1}, (c) Mott-Schottky plots, and (d) Nyquist plots.

In addition to the current enhancement, the redox peaks exhibit a noticeable potential shift under light illumination. This shift can be attributed to the increased carrier density and the reduced interfacial resistance in the illuminated state since the energetic barrier is

lowered for electron transfer and consequently the reaction kinetics is accelerated. Combination of these peak shifts with the bigger current response leads one to believe that illumination not only increases the reaction rate but also modifies the interfacial energetics of the electrode. In this way more efficient and reversible NH_4^+ storage is realized on this composite electrode.

The properties of this electrode were also investigated by means of the Mott-Schottky analysis in both dark and light (**Figure 5.9c**). Positive slopes are seen these Mott-Schottky plots, the sign of a *n*-type response that arises from the highly defective and amorphous nature of WO_3 in conjunction with the heavily doped BDD substrate. A systematic reduction in this slope is caused by light illumination, indicating an increase in the effective carrier density and a narrowing of the depletion layer at the electrode/electrolyte interface. The extrapolated interception shifts towards more positive potential under light, signifying a reduction in band bending and a decrease in the energetic barrier for electron transfer. Additionally, the Mott-Schottky curve under illuminated conditions shows an extended linear region and a more pronounced low-potential plateau, reflecting trap filling and improved electrostatic screening. These changes confirm that illumination improves interfacial electronic conductivity and facilitates faster charge injection. Related EIS measurements (**Figure 5.9d**) show nearly identical Nyquist plots under dark and illuminated conditions. For example, minimal differences are seen in measured charge transfer resistances. This fact indicates that the primary photo enhancement occurs through improved charge separation and transport, rather than fundamental changes in interfacial kinetics. The relatively low charge transfer resistance confirms the effective charge transport that is facilitated by the BDD support, while the unchanged impedance characteristics suggest stable interface properties during photoelectrochemical operation on this composite electrode.

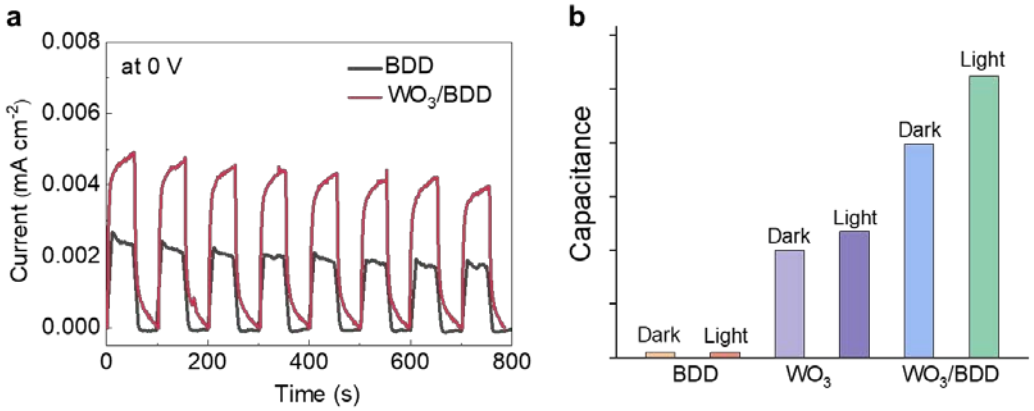


Figure 5.10 Comparative photoelectrochemical performance: (a) Direct comparison of photocurrent response between BDD and WO_3/BDD at a bias potential of 0 V (*vs*. OCP), and (b) capacitance enhancement under dark and illuminated conditions across different electrodes.

The direct photocurrent comparison (**Figure 5.10a**) clearly demonstrates the superior performance of the WO_3/BDD composite electrode compared to a BDD electrode. On the composite electrode (red line) a photocurrent density of ~0.005 mA cm^{-2} is achieved, nearly double that (~0.003 mA cm^{-2}) using a BDD electrode. This enhancement validates that WO_3 provides the primary photoactive component while BDD serves as an efficient charge transport medium. Both materials exhibit gradual decay over the measurement period, but the composite maintains consistently higher photocurrent levels throughout all tests, confirming the effectiveness of the heterojunction design for enhanced light harvesting and charge separation.

The capacitance comparison (**Figure 5.10b**) provides crucial insights into the photo-assisted energy storage mechanism of ammonium ion storage. On a BDD electrode minimal photo enhancement is found, with virtually identical capacitances under dark and illuminated conditions in that this electrode plays a single role as a conductive support rather than an active storage material. On a WO_3 electrode, moderate photo enhancement is seen, indicating that illumination improves its charge storage capability through photogenerated carrier participation in these electrochemical processes. The WO_3/BDD

composite exhibits the most significant photo enhancement effect, with substantially higher capacitances under illumination compared to both its dark-state performance and the individual components. Th synergistic effect between WO_3 and BDD is thus supposed to exist for such enhancement. This probably arises from multiple factors. For example, this *p*-*n* junction can facilitate efficient charge separation, prevent recombination losses that typically limit photoelectrochemical performance. The excellent conductivity of the BDD enables rapid electron extraction from WO_3, maintaining high concentrations of active sites for NH_4^+ storage. The internal electric field at the heterojunction interface can also provide additional driving force for charge transfer processes.

This capacitance enhancement directly translates to improved NH_4^+ storage performance, as a higher capacitance indicates increased charge accumulation capability, which corresponds to enhanced NH_4^+ insertion capacity. The results confirm that photo assisted operation significantly improves the energy storage performance of the composite system beyond what can be achieved through simple additive effects of the individual components.

5.5 Conclusions

In this chapter, a novel WO_3/BDD composite has been successfully designed and evaluated as an advanced electrode material for photo-assisted NH_4^+ hybrid supercapacitors. The integration of WO_3 with the highly conductive boron-doped diamond scaffold enables the construction of a *p*–*n* junction, which significantly improves charge separation, electron transport, and structural stability. Comprehensive electrochemical characterizations under dark conditions demonstrate that the composite electrode exhibits substantially higher capacitance, lower polarization, and enhanced rate performance compared to pristine WO_3, while maintaining the robustness and wide potential window characteristic of BDD. Upon illumination, the electrode displays markedly enhanced photocurrent responses, enlarged CV areas, peak shifts toward lower overpotentials, reduced charge-transfer resistance, and increased carrier density. These

findings confirm that the intrinsic built-in electric field at the WO_3/BDD interface. Together with the superior conductivity of BDD, this composite electrode effectively facilitates photocarrier utilization for NH_4^+ storage.

Overall, this *p*-*n* junction design establishes a new paradigm for composite electrode development, where the exceptional properties of diamond are leveraged to address the fundamental limitations of conventional energy storage materials while maintaining the proven ammonium ion storage capability of WO_3. The WO_3/BDD composite electrode features a synergistic improvement in both electrochemical and photoelectrochemical performance. It is thus a promising platform for the development of high-performance, light-assisted hybrid supercapacitor devices. Moreover, it highlights the great potential of diamond-based materials for next-generation electrochemical energy systems.

6 Summary and outlook

6.1 Summary

This dissertation presents a systematic investigation of advanced tungsten oxide-based electrode materials for the construction of high-performance ammonium-ion hybrid supercapacitors after addressing critical challenges of poor conductivity, limited ion accessibility, and insufficient cycling stability with aid of innovative material design and photo-enhancement strategies. **(Figure 6.1)**

In more detail, folded nanocrystalline-stacked amorphous WO_3 electrodes have been synthesized *via* a rapid electrochemical deposition method. The innovative architecture combines nano-structural fragmentation with controlled amorphization, creating a hierarchical framework where ~5 nm crystallites are loosely assembled within an amorphous matrix. This design provides abundant grain boundaries, shortened diffusion pathways, and enhanced structural flexibility for accommodating volumetric changes during cycling. The a-WO_3 electrode achieves an exceptional areal capacitance of 2783 mF cm^{-2} with excellent rate performance and pseudocapacitive-dominated charge storage behavior. When assembled into a full-cell device with polyaniline cathode, the system delivers remarkable energy and power densities of 620 mWh cm^{-2} and 23,980 mW cm^{-2}, respectively, with 81.5% capacity retention after 3000 cycles. Mechanistic studies reveal that NH_4^+ storage occurs through reversible hydrogen bonding rather than conventional coordination interactions, resulting in lower diffusion barriers (~0.38 eV), reduced lattice strain, and enhanced reversibility compared to traditional metal-ion systems.

The WO_3/TiO_2 heterojunction composites have been designed to harness photo-enhanced energy storage capabilities through synergistic optical and electrochemical properties. These Type II heterojunctions have been engineered by means of aligning the band between WO_3 and TiO_2. A key design strategy of preparing island-like distributed WO_3 nanocrystals on TiO_2 substrates is through controlling electrochemical deposition parameters. This island-like growth mode ensures simultaneous exposure of both

materials to the electrolyte, achieving true synergistic effects rather than simple serial coupling. In the meanwhile, the heterojunction interface area is maximized for efficient charge separation and transport. Under illumination, the optimized WO_3/TiO_2 composite demonstrates 40% capacity enhancement compared to dark conditions, with significantly reduced charge transfer resistance and improved charge carrier dynamics. The photoelectrochemical measurements confirm enhanced light absorption, improved carrier separation efficiency, and accelerated ion transport kinetics. This work thus offers the potential of Type II heterojunctions for solar-rechargeable energy storage devices with dual functionality.

Furthermore, WO_3/diamond composite materials that leverage the exceptional properties of BDD have been synthesized to address fundamental limitations of tungsten oxide electrodes. The strategic combination creates a *p*-*n* junction configuration where the intrinsic electric field between *p*-type BDD and *n*-type WO_3 provides enhanced charge separation efficiency. Superior electrical conductivity, chemical stability, and mechanical properties of diamond provide synergistic enhancements when integrated with WO_3. The BDD serves as highly conductive nodes within the composite matrix, creating percolating networks that dramatically improve electron transport while in the meanwhile maintain structural integrity during repeated charge/discharge cycles. Photoelectrochemical characterization proves significantly improved photocurrent response, enhanced capacity under illumination, and extended cycling lifetime when compared to pristine WO_3. In conclusion, the *p*-*n* junction design is effective for photo-assisted energy storage applications.

Collectively, these three above-shown approaches, namely structural engineering, heterojunction construction, and conductive scaffold integration, can be synergistically applied to unlock superior NH_4^+ storage performance with intrinsic photo-enhanced functionality. The dissertation not only provides detailed mechanistic insight of revealing how defects, band alignment, and internal electric fields govern charge storage and

transport, but also establishes generalizable design principles for next-generation photo responsive electrode materials.

In summary, this work contributes to the advancement of sustainable energy storage by demonstrating the feasibility of combining solar energy harvesting with aqueous NH_4^+ storage in a single electrode system. Beyond AIHSs, the strategies presented here can be extended to other aqueous-ion chemistries and multifunctional electrochemical devices, paving the way toward integrated light-assisted energy storage technologies that are efficient, safe, and environmentally benign.

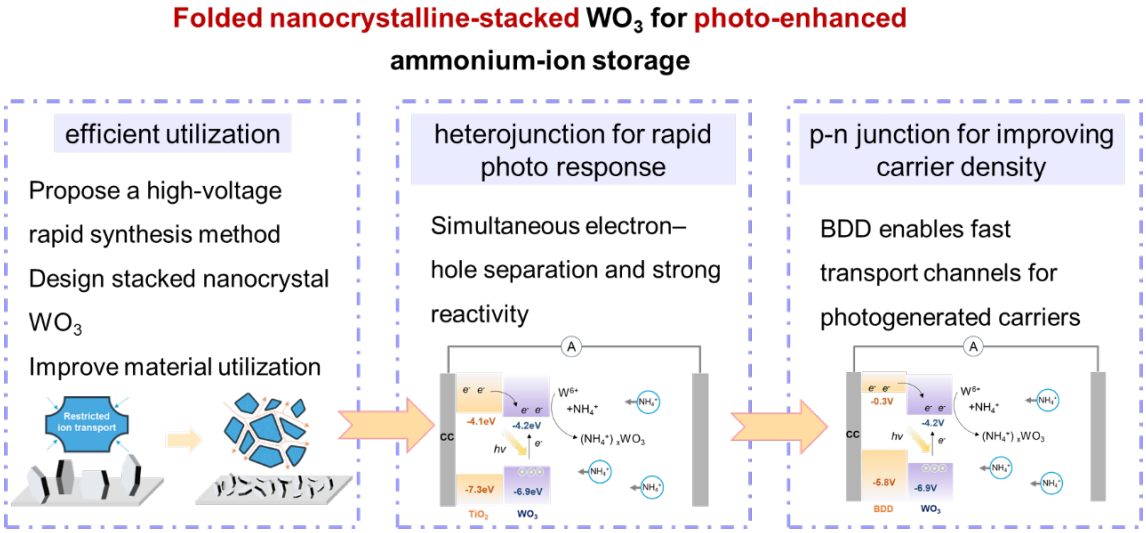


Figure 6.1 Graphical summary of this thesis.

6.2 Outlook

6.2.1 Advanced characterization of nanocrystalline structures

In this work folded nanocrystalline-stacked architectures with ~5 nm crystallites have been successfully synthesized. However, the structural characterization was primarily limited to TEM and XRD techniques. Due to the highly disordered nature of these materials, conventional XRD only provided minimal structural information. Advanced characterization techniques are thus needed to comprehensively understand their nanocrystalline structure and defect chemistry. For instance, *in situ* TEM during electrochemical deposition might be powerful, especially to reveal real-time

nanocrystalline formation and growth mechanisms; *in situ* small-angle X-ray scattering (SAXS) is expected to provide statistical information about particle size distributions and structural evolution during synthesis. These comprehensive characterizations can certainly provide fundamental insights into the relationship between nanocrystalline structure, defect chemistry, and electrochemical performance, enabling rational optimization of synthesis parameters for enhanced NH_4^+ storage capabilities.

6.2.2 Dual-ion systems and multi-chemistry integration

The concept of photo-assisted NH_4^+ storage demonstrated in this work needs to be further extended to dual-ion systems, where NH_4^+ insertion can be coupled with other charge carriers such as H^+ or Zn^{2+}. This is because such hybrid configurations may combine the fast kinetics of hydrogen intercalation with the high capacity of multivalent cations, eventually enabling devices that simultaneously benefit from rapid charge–discharge rates and enhanced energy density. Taking coupling WO_3-based photoanodes with Zn^{2+}-storage cathodes as an example, the resultant aqueous Zn–NH_4^+ dual-ion cells are expected to feature superior stability and multifunctionality. Differently, a NH_4^+/H^+ co-insertion device can further reduce intercalation barriers through synergistic hydrogen bonding. Exploring these dual-ion chemistries under light illumination may also open new opportunities for integrated solar-rechargeable devices that deliver higher energy densities, extended lifetimes, and broader applicability in sustainable energy storage.

6.2.3 Advanced characterization of photo-enhancement mechanisms

While several heterojunction architectures — WO_3/TiO_2 type-II structures and WO_3/BDD *p*–*n* junctions — have been proposed in this dissertation to explain the observed photo-enhanced NH_4^+ storage, the current evidence remains insufficient, according to conducted electrochemical measurements, band alignment estimations, and theoretical considerations. The next step is therefore critical about how to clearly clarify

the direct experimental validation of these heterojunction mechanisms. Advanced techniques are supposed to provide real-time insights into carrier generation, separation, and recombination dynamics at the electrode/electrolyte interface, and reveal the structural and electronic evolution of the heterojunction during operation. Establishing such direct evidence will be essential for moving from conceptual designs toward rational, predictive engineering of photoactive heterostructures with robust and reproducible performance.

6.2.4 Mathematical simulation and AI-assisted design

Beyond experimental investigations, mathematical modeling and artificial intelligence (AI) can play pivotal roles in accelerating the understanding and design of photo-assisted ammonium-ion storage systems. Multiphysics simulations—combining electronic structure calculations, ion diffusion dynamics, and photoelectrochemical kinetics—can quantitatively predict charge-transfer pathways and optimize interfacial energetics. In parallel, AI-assisted data analysis and machine learning algorithms can identify hidden correlations between structural parameters and electrochemical performance from large experimental datasets. Such digital approaches are expected to guide the rational selection of electrode materials, predict optimal heterojunction configurations, and enable autonomous optimization of synthesis conditions. The integration of mathematical modeling with AI-driven design will therefore represent a powerful direction toward intelligent, predictive, and efficient development of next-generation light-assisted energy storage devices.

7 References

(1) Armand, M.; Tarascon, J. M. Building Better Batteries. *Nature* **2008**, *451*, 652–657.

(2) Dunn, B.; Kamath, H.; Tarascon, J. M. Electrical Energy Storage for the Grid: A Battery of Choices. *Science* **2011**, *334*, 928–935.

(3) Li, M.; Lu, J.; Chen, Z.; Amine, K. 20 Years of Lithium Ion Battery Development. *Adv. Mater.* **2018**, *30* (33), 1800561.

(4) Liang, Y.; Dong, H.; Aurbach, D.; Yao, Y. Current Status and Future Directions of Multivalent Metal-Ion Batteries. *Nat. Energy* **2020**, *5*, 646–656.

(5) Xu, X.; Sun, C.; Yu, Y. Recent Advances in Aqueous Energy Storage Systems. *Energy Environ. Sci.* **2021**, *14*, 1283–1296.

(6) Zhang, X.; Zhao, Y.; Yu, H. Electrochemical Energy Storage: From Fundamentals to Applications. *Chem. Soc. Rev.* **2020**, *49*, 3040–3102.

(7) Chen, L.; Zhu, X.; Yan, C. Recent Progress on Energy Storage and Conversion. *Nat. Commun.* **2020**, *11*, 2072.

(8) Wang, H.; Cui, Y. Nanostructured Materials for Electrochemical Energy Storage. *Nat. Rev. Mater.* **2021**, *6*, 388–404.

(9) Li, W.; Wang, K.; Jiang, J. Emerging Aqueous Energy Storage Technologies. *Energy Storage Mater.* **2021**, *34*, 282–289.

(10) Wang, Y.; Kuchena, S. F. Recent Progress in Aqueous Ammonium-Ion Batteries. *ACS Omega* **2022**, *7* (38), 33732–33748.

(11) Liang, Y.; Yao, Y. Designing Modern Aqueous Batteries. *Nat. Rev. Mater.* **2023**, *8* (2), 109–122.

(12) Chao, D.; Zhou, W.; Xie, F.; Ye, C.; Li, H.; Jaroniec, M.; Qiao, S.-Z. Roadmap for Advanced Aqueous Batteries: From Design of Materials to Applications. *Science Advances* **2020**, *6* (21), 4098.

(13) Zhang, X.; Cheng, X.; Zhang, Q. Nanostructured Energy Materials for Electrochemical Energy Conversion and Storage: A Review. *J. Energy Chem.* **2016**, *25* (6), 967–984. https://doi.org/10.1016/j.jechem.2016.11.003.

(14) Sun, Y.; Yin, B.; Yang, J.; Ding, Y.; Li, M.; Li, H.; Li, J.; Jia, B.; Zhang, S.; Ma, T. Ammonium-Ion Energy Storage Devices for Real-Life Deployment: Storage Mechanism, Electrode Design and System Integration. *Energy Environ. Sci.* **2023** 16, 5568-5604. https://doi.org/10.1039/D3EE02030D.

(15) Zheng, R.; Li, Y.; Yu, H.; Zhang, X.; Yang, D.; Yan, L.; Li, Y.; Shu, J.; Su, B.-L. Ammonium Ion Batteries: Material, Electrochemistry and Strategy. *Angew. Chem. Int. Ed.* **2023**, *62* (23), e202301629. https://doi.org/10.1002/anie.202301629.

(16) Chen, Q.; Jin, J.; Song, M.; Zhang, X.; Li, H.; Zhang, J.; Hou, G.; Tang, Y.; Mai, L.; Zhou, L. High-Energy Aqueous Ammonium-Ion Hybrid Supercapacitors. *Adv. Mater.* **2022**, *34* (8), 2107992. https://doi.org/10.1002/adma.202107992.

(17) Wang, J.; Liao, W.; Tan, Y.; Henrotte, O.; Kang, Y.; Liu, K.; Fu, J.; Lin, Z.; Chai, L.; Cortes, E.; Liu, M. Transfer Dynamics of Photo-Generated Carriers in Catalysis. *Chem. Soc. Rev.* **2025**, *54* (13), 6553–6596. https://doi.org/10.1039/D5CS00512D.

(18) Hu, S.; Zhu, M. Semiconductor for Oxygen Electrocatalysis in Photo-Assisted Rechargeable Zinc-Air Batteries: Principles, Advances, and Opportunities. *Energy Storage Mater.* **2023**, *61*, 102866. https://doi.org/10.1016/j.ensm.2023.102866.

(19) Lv, J.; Xie, J.; Mohamed, A. G. A.; Zhang, X.; Wang, Y. Photoelectrochemical Energy Storage Materials: Design Principles and Functional Devices towards Direct Solar to Electrochemical Energy Storage. *Chem. Soc. Rev.* **2022**, *51* (4), 1511–1528. https://doi.org/10.1039/D1CS00859E.

(20) Xu, J.; Li, Y.; Wang, T.; Dong, Z.; Jin, R.; Guo, K.; Lin, X.; Huang, K.-J. MoS2/ReS2 Hollow Heterojunction for Enhanced Aqueous Zinc-Ion Storage Performance. *ACS Appl. Mater. Interfaces* **2024**, *16* (18), 23734–23741. https://doi.org/10.1021/acsami.4c01993.

(21) Bisquert, J.; Cendula, P.; Bertoluzzi, L.; Gimenez, S. Energy Diagram of Semiconductor/Electrolyte Junctions. *J. Phys. Chem. Lett.* **2014**, *5* (1), 205–207. https://doi.org/10.1021/jz402703d.

(22) Lewis, N. S. Light Work with Water. *Nature* **2001**, *414* (6864), 589–590. https://doi.org/10.1038/414589a.

(23) Zhao, L.; Li, Y.; Yu, M.; Peng, Y.; Ran, F. Electrolyte-Wettability Issues and Challenges of Electrode Materials in Electrochemical Energy Storage, Energy Conversion, and Beyond. *Adv. Sci.* **2023**, *10* (17), 2300283. https://doi.org/10.1002/advs.202300283.

(24) Zhou, M.; Huang, X.; Li, H.; Duan, X.; Zhao, Q.; Ma, T. Hydrogen Bonding Chemistry in Aqueous Ammonium Ion Batteries. *Angew. Chem. Int. Ed.* **2024**, *63* (46), e202413354. https://doi.org/10.1002/anie.202413354.

(25) Dunn, B.; Kamath, H.; Tarascon, J.-M. Electrical Energy Storage for the Grid: A Battery of Choices. *Science* **2011**, *334* (6058), 928–935. https://doi.org/10.1126/science.1212741.

(26) Gurung, A.; Qiao, Q. Solar Charging Batteries: Advances, Challenges, and Opportunities. *Joule* **2018**, *2* (7), 1217–1230. https://doi.org/10.1016/j.joule.2018.04.006.

(27) Luo, B.; Ye, D.; Wang, L. Recent Progress on Integrated Energy Conversion and Storage Systems. *Adv. Sci.* **2017**, *4* (9), 1700104. https://doi.org/10.1002/advs.201700104.

(28) Zhao, Y.; He, T.; Li, J.; Zhu, C.; Tan, Y.; Zhu, K.; Chou, S.; Chen, Y. Carbon Superstructure-Supported Half-Metallic V_2O_3 Nanospheres for High-Efficiency Photorechargeable Zinc Ion Batteries. *Angew. Chem. Int. Ed.* **2024**, e202408218. https://doi.org/10.1002/anie.202408218.

(29) Yu, S.; Sun, H.; Ullah, Z.; Chen, L.; An, X.; Chen, M.; Zhu, S.; Liu, L.; Li, Q. Photo-Assisted Bifunctional Cathodes with Lower Energy Gap and Broadened Light Absorbing Region for Lithium-Ion Batteries – Extended Conjugation Through Customization. *Adv. Funct. Mater.* **2024**, 2403295. https://doi.org/10.1002/adfm.202403295.

(30) Zha, W.; Ruan, Q.; Ma, L.; Liu, M.; Lin, H.; Sun, L.; Sun, Z.; Tao, L. Highly Stable Photo-Assisted Zinc-Ion Batteries via Regulated Photo-Induced Proton Transfer. *Angew. Chem. Int. Ed.* **2024**, *63* (15), e202400621. https://doi.org/10.1002/anie.202400621.

(31) Zhang, Z.; Yates, J. T. Jr. Band Bending in Semiconductors: Chemical and Physical Consequences at Surfaces and Interfaces. *Chem. Rev.* **2012**, *112* (10), 5520–5551. https://doi.org/10.1021/cr3000626.

(32) Zhao, L.; Li, Y.; Yu, M.; Peng, Y.; Ran, F. Electrolyte-Wettability Issues and Challenges of Electrode Materials in Electrochemical Energy Storage, Energy Conversion, and Beyond. *Adv. Sci.* **2023**, *10* (17), 2300283. https://doi.org/10.1002/advs.202300283.

(33) Xu, J.; Ku, Z.; Zhang, Y.; Chao, D.; Fan, H. J. Integrated Photo-Supercapacitor Based on PEDOT Modified Printable Perovskite Solar Cell. *Adv. Mater. Technol.* **2016**, *1* (5), 1600074. https://doi.org/10.1002/admt.201600074.

(34) Fehr, A. M. K.; Agrawal, A.; Mandani, F.; Conrad, C. L.; Jiang, Q.; Park, S. Y.; Alley, O.; Li, B.; Sidhik, S.; Metcalf, I.; Botello, C.; Young, J. L.; Even, J.; Blancon, J. C.; Deutsch, T. G.; Zhu, K.; Albrecht, S.; Toma, F. M.; Wong, M.; Mohite, A. D. Integrated Halide Perovskite Photoelectrochemical Cells with Solar-Driven Water-Splitting Efficiency of 20.8%. *Nat. Commun.* **2023**, *14* (1), 3797. https://doi.org/10.1038/s41467-023-39290-y.

(35) Lv, J.; Xie, J.; Mohamed, A. G. A.; Zhang, X.; Wang, Y. Photoelectrochemical Energy Storage Materials: Design Principles and Functional Devices towards Direct Solar to Electrochemical Energy Storage. *Chem. Soc. Rev.* **2022**, *51* (4), 1511–1528. https://doi.org/10.1039/d1cs00859e.

(36) Yan, N.-F.; Gao, X.-P. Photo-Assisted Rechargeable Metal Batteries for Energy Conversion and Storage. *Energy Environ. Mater.* **2021**. https://doi.org/10.1002/eem2.12182.

(37) Liu, R.; Wang, Z. L.; Fukuda, K.; Someya, T. Flexible Self-Charging Power Sources. *Nat. Rev. Mater.* **2022**, 1–17. https://doi.org/10.1038/s41578-022-00441-0.

(38) Man, Y.; Hao, Q.; Chen, F.; Chen, X.; Wang, Y.; Liu, T.; Liu, F.; Li, N. A Photo-Assisted Chargeable Aqueous Zinc-Iodine Battery. *ChemElectroChem* **2019**, *6* (23), 5872–5875. https://doi.org/10.1002/celc.201901712.

(39) Miyasaka, T.; Murakami, T. N. The Photocapacitor: An Efficient Self-Charging Capacitor for Direct Storage of Solar Energy. *Appl. Phys. Lett.* **2004**, *85* (17), 3932–3934. https://doi.org/10.1063/1.1810630.

(40) Yu, M.; Ren, X.; Ma, L.; Wu, Y. Integrating a Redox-Coupled Dye-Sensitized Photoelectrode into a Lithium–Oxygen Battery for Photoassisted Charging. *Nat. Commun.* **2014**, *5* (1), 5111. https://doi.org/10.1038/ncomms6111.

(41) Liu, X.; Yuan, Y.; Liu, J.; Liu, B.; Chen, X.; Ding, J.; Han, X.; Deng, Y.; Zhong, C.; Hu, W. Utilizing Solar Energy to Improve the Oxygen Evolution Reaction Kinetics in Zinc–Air Battery. *Nat. Commun.* **2019**, *10* (1), 4767. https://doi.org/10.1038/s41467-019-12627-2.

(42) Li, C.; Cong, S.; Tian, Z.; Song, Y.; Yu, L.; Lu, C.; Shao, Y.; Li, J.; Zou, G.; Rümmeli, M. H.; Dou, S.; Sun, J.; Liu, Z. Flexible Perovskite Solar Cell-Driven Photo-Rechargeable Lithium-Ion Capacitor for Self-Powered Wearable Strain Sensors. *Nano Energy* **2019**, *60*, 247–256. https://doi.org/10.1016/j.nanoen.2019.03.061.

(43) Guan, D.-H.; Wang, X.-X.; Li, M.-L.; Li, F.; Zheng, L.-J.; Huang, X.-L.; Xu, J.-J. Light/Electricity Energy Conversion and Storage for a Hierarchical Porous In_2S_3@CNT/SS Cathode towards a Flexible Li-CO_2 Battery. *Angew. Chem. Int. Ed.* **2020**, *59* (44), 19518–19524. https://doi.org/10.1002/anie.202005053.

(44) Hauch, A.; Georg, A.; Krašovec, U. O.; Orel, B. Photovoltaically Self-Charging Battery. *J. Electrochem. Soc.* **2002**, *149* (9), A1208. https://doi.org/10.1149/1.1500346.

(45) Hodes, G.; Manassen, J.; Cahen, D. Photoelectrochemical Energy Conversion and Storage Using Polycrystalline Chalcogenide Electrodes. *Nature* **1976**, *261* (5559), 403–404. https://doi.org/10.1038/261403a0.

(46) Liu, X.; Tao, S.; Zhang, J.; Zhu, Y.; Ma, R.; Lu, J. Ultrathin p–n Type Cu_2O/CuCoCr-Layered Double Hydroxide Heterojunction Nanosheets for Photo-Assisted Aqueous Zn–CO_2 Batteries. *J. Mater. Chem. A* **2021**, *9* (46), 26061–26068. https://doi.org/10.1039/D1TA07522E.

(47) Boruah, B. D.; Mathieson, A.; Wen, B.; Jo, C.; Deschler, F.; De Volder, M. Photo-Rechargeable Zinc-Ion Capacitor Using 2D Graphitic Carbon Nitride. *Nano Lett.* **2020**, *20* (8), 5967–5974. https://doi.org/10.1021/acs.nanolett.0c01958.

(48) Boruah, B.; Mathieson, A.; Wen, B.; Feldmann, S.; M. Dose, W.; Volder, M. D. Photo-Rechargeable Zinc-Ion Batteries. *Energy Environ. Sci.* **2020**, *13* (8), 2414–2421. https://doi.org/10.1039/D0EE01392G.

(49) Gouder, A.; Podjaski, F.; Jiménez-Solano, A.; Kröger, J.; Wang, Y.; V. Lotsch, B. An Integrated Solar Battery Based on a Charge Storing 2D Carbon Nitride. *Energy Environ. Sci.* **2023**, *16* (4), 1520–1530. https://doi.org/10.1039/D2EE03409C.

(50) Du, X.-Y.; Song, L.-N.; Liang, S.; Wang, Y.-F.; Wang, Y.; Wang, H.-F.; Xu, J.-J. Photo-Assisted Chemical Self-Rechargeable Zinc Ion Batteries with High Charging and Discharging Efficiency. *Angew. Chem.* **2024**, e202411845. https://doi.org/10.1002/ange.202411845.

(51) Wang, M.; Chen, J.; Tian, Z.; Dai, W.; Cui, B.; Cui, X.; Wang, D.; Xiao, Y.; Lian, X.; Jiang, C.; Yang, H.; Wang, Y.; Sun, Z.; Ding, Y.; Sun, Y.-Y.; Zhang, J.; Chen, W. Facet-Controlled Bifunctional WO_3 Photocathodes for High-Performance Photo-Assisted Li–O_2 Batteries. *Energy Environ. Sci.* **2023**, *16* (2), 523–534. https://doi.org/10.1039/D2EE03724F.

(52) Cai, Q.; Di, G.; Yin, X.; Liu, Y.; Wang, G.; Kuang, Y.; Xiang, X.; Wang, K.; Zhang, L.; Chen, X.; Lv, X. The Photoelectrode of Photo-Rechargeable Zinc-Ion Batteries:

Design, Progress. *J. Power Sources* **2025**, *628*, 235854. https://doi.org/10.1016/j.jpowsour.2024.235854.

(53) Dong, X.; Chen, X.; Jiang, X.; Yang, N. Light-Assisted Energy Storage Devices: Principles, Performance, and Perspectives. *Adv Energy Mater* **2023**, 2301143.

(54) Wang, Y.; Chan, Y.-T.; Oshima, T.; Duppel, V.; Bette, S.; Küster, K.; Gouder, A.; Scheurer, C.; Lotsch, B. V. Decoupling of Light and Dark Reactions in a 2D Niobium Tungstate for Light-Induced Charge Storage and On-Demand Hydrogen Evolution. *J. Am. Chem. Soc.* **2024**, *146* (37), 25467–25476. https://doi.org/10.1021/jacs.4c04140.

(55) Jain, S.; Bhattacharjee, D.; Verma, A. K.; Pathak, H.; Mayes, E. L. H.; Bhattacharya, A.; Dhakate, S. R.; Gahtori, B. Synergistic Optimization of Electronic and Thermal Transport in Hf-Free ZrNiSn HH Alloy through WO_3 Compositing. *ACS Appl. Energy Mater.* **2024**, *7* (17), 7251–7259. https://doi.org/10.1021/acsaem.4c01239.

(56) Varadhan, P.; Fu, H.-C.; Kao, Y.-C.; Horng, R.-H.; He, J.-H. An Efficient and Stable Photoelectrochemical System with 9% Solar-to-Hydrogen Conversion Efficiency via InGaP/GaAs Double Junction. *Nat. Commun.* **2019**, *10* (1), 5282. https://doi.org/10.1038/s41467-019-12977-x.

(57) Lo Vecchio, C.; Giacoppo, G.; Barbera, O.; Carbone, A.; Baglio, V.; Aricò, A. S.; Monforte, G.; Trocino, S. Scalability and Investigation of the Geometrical Features and Shapes of a Tandem Photo-Electrolysis Cell Based on Non-Critical Raw Materials. *Catalysts* **2024**, *14* (2), 98. https://doi.org/10.3390/catal14020098.

(58) Górski, B.; Rein, J.; Norris, S.; Ji, Y.; McEuen, P. L.; Lin, S. Light-Harvesting Microelectronic Devices for Wireless Electrosynthesis. *Nature* **2025**, *637* (8045), 354–361. https://doi.org/10.1038/s41586-024-08373-1.

(59) Ross, B.; Haussener, S.; Brinkert, K. Assessment of the Technological Viability of Photoelectrochemical Devices for Oxygen and Fuel Production on Moon and Mars. *Nat. Commun.* **2023**, *14* (1), 3141. https://doi.org/10.1038/s41467-023-38676-2.

(60) Yang, S.; Zhao, W.; Mi, Y.; Li, B.; Dong, Y.; Xie, K.; Zhao, W.; Long, G.; Du, P. Nitrogen-Induced Hydrogen Bonding Supramolecular Network for Ultra-Stable Ammonium Ion Storage. *Angew. Chem. Int. Ed.* **2025**, e202511826. https://doi.org/10.1002/anie.202511826.

(61) Xu, J.; Liu, T.; Dong, X.; Dong, X.; Zhou, W.; Li, X.; Chao, D.; Zhou, Z.; Zhao, R. Challenges and Opportunities in 2D Materials for High-Performance Aqueous Ammonium Ion Batteries. *Natl. Sci. Rev.* **2025**, *12* (2). https://doi.org/10.1093/nsr/nwae433.

(62) Sun, F.-F.; Guan, X.; Huang, Z.-H.; Han, X.; Li, H.; Ma, T. Fluoride-Based Hydrogen Bond Chemistry in a Layered Double Hydroxide Cathode toward High-Performance Aqueous NH4+ Storage. *Proc. Natl. Acad. Sci.* **2025**, *122* (8), e2414112122. https://doi.org/10.1073/pnas.2414112122.

(63) Shi, M.; Zhang, X. Pioneering the Future: Principles, Advances, and Challenges in Organic Electrodes for Aqueous Ammonium-Ion Batteries. *Adv. Mater.* **2025**, *37* (13), 2415676. https://doi.org/10.1002/adma.202415676.

(64) Tian, Z.; Kale, V. S.; Thomas, S.; Kandambeth, S.; Nadinov, I.; Wang, Y.; Wahyudi, W.; Lei, Y.; Emwas, A.-H.; Bonneau, M.; Shekhah, O.; Bakr, O. M.; Mohammed, O. F.; Eddaoudi, M.; Alshareef, H. N. An Ultrastable Aqueous Ammonium-Ion Battery Using a Covalent Organic Framework Anode. *Adv. Mater.* **2024**, *36* (47), 2409354. https://doi.org/10.1002/adma.202409354.

(65) Wu, X.; Qi, Y.; Hong, J. J.; Li, Z.; Hernandez, A. S.; Ji, X. Rocking-Chair Ammonium-Ion Battery: A Highly Reversible Aqueous Energy Storage System. *Angew. Chem. Int. Ed.* **2017**, *56* (42), 13026–13030. https://doi.org/10.1002/anie.201707473.

(66) Wang, S.; Huang, S.; Yao, M.; Zhang, Y.; Niu, Z. Engineering Active Sites of Polyaniline for $AlCl_2^+$ Storage in an Aluminum-Ion Battery. *Angew. Chem. Int. Ed.* **2020**, *59* (29), 11800–11807. https://doi.org/10.1002/anie.202002132.

(67) Dai, J.; Yang, C.; Xu, Y.; Wang, X.; Yang, S.; Li, D.; Luo, L.; Xia, L.; Li, J.; Qi, X.; Cabot, A.; Dai, L. MoS_2@Polyaniline for Aqueous Ammonium-Ion Supercapacitors. *Adv. Mater.* **2023**, 2303732. https://doi.org/10.1002/adma.202303732.

(68) Gao, M.; Wang, Z.; Liu, Z.; Huang, Y.; Wang, F.; Wang, M.; Yang, S.; Li, J.; Liu, J.; Qi, H.; Zhang, P.; Lu, X.; Feng, X. 2D Conjugated Metal–Organic Frameworks Embedded with Iodine for High-Performance Ammonium-Ion Hybrid Supercapacitors. *Adv. Mater.* **2023**, *35* (41), 2305575. https://doi.org/10.1002/adma.202305575.

(69) Zhang, X.; Javed, M. S.; Ali, S.; Ahmad, A.; Shah, S. S. A.; Hussain, I.; Choi, D.; Tighezza, A. M.; Tag-Eldin, E.; Xia, C.; Ali, S.; Han, W. Band Engineering in $Ti_2N/Ti_3C_2T_X$-MXene Interface Enhance the Performance of Aqueous NH_4^+-Ion Hybrid Supercapacitors. *Nano Energy* **2024**, *120*, 109108. https://doi.org/10.1016/j.nanoen.2023.109108.

(70) Niu, K.; Shi, J.; Zhang, L.; Yue, Y.; Mo, S.; Li, S.; Li, W.; Wen, L.; Hou, Y.; Sun, L.; Yan, S.; Long, F.; Gao, Y. MXene-Integrated Perylene Anode with Ultra-Stable and Fast Ammonium-Ion Storage for Aqueous Micro Batteries. *Adv. Sci.* **2023**, 2305524. https://doi.org/10.1002/advs.202305524.

(71) Zhang, X.; Wei, H.; Ren, B.; Jiang, J.; Qu, G.; Yang, J.; Chen, G.; Li, H.; Zhi, C.; Liu, Z. Unlocking High-Performance Ammonium-Ion Batteries: Activation of In-Layer Channels for Enhanced Ion Storage and Migration. *Adv. Mater.* **2023**, 2304209. https://doi.org/10.1002/adma.202304209.

(72) Zhang, Y.-Z.; Liang, J.; Huang, Z.; Wang, Q.; Zhu, G.; Dong, S.; Liang, H.; Dong, X. Ionically Conductive Tunnels in H-WO3 Enable High-Rate NH_4^+ Storage. *Adv. Sci.* **2022**, *9* (10), 2105158. https://doi.org/10.1002/advs.202105158.

(73) Chen, Q.; Li, H.; Lou, X.; Zhang, J.; Hou, G.; Lu, J.; Tang, Y. Surface Oxygen Coordination of Hydrogen Bond Chemistry for Aqueous Ammonium Ion Hybrid Supercapacitor. *Adv. Funct. Mater.* **2023**, *33* (17), 2214920. https://doi.org/10.1002/adfm.202214920.

(74) Liu, Y.; Xiang, K.; Zhou, W.; Deng, W.; Zhu, H.; Chen, H. Investigations on Tunnel-Structure MnO_2 for Utilization as a High-Voltage and Long-Life Cathode Material in Aqueous Ammonium-Ion and Hybrid-Ion Batteries. *Small* **2024**, *20* (20), 2308741. https://doi.org/10.1002/smll.202308741.

(75) Dong, S.; Shin, W.; Jiang, H.; Wu, X.; Li, Z.; Holoubek, J.; Stickle, W. F.; Key, B.; Liu, C.; Lu, J.; Greaney, P. Alex.; Zhang, X.; Ji, X. Ultra-Fast NH_4^+ Storage: Strong H Bonding between NH_4^+ and Bi-Layered V_2O_5. *Chem* **2019**, *5* (6), 1537–1551. https://doi.org/10.1016/j.chempr.2019.03.009.

(76) Yu, D.; Wei, Z.; Zhang, X.; Zeng, Y.; Wang, C.; Chen, G.; Shen, Z. X.; Du, F. Boosting Zn^{2+} and NH_4^+ Storage in Aqueous Media via In-Situ Electrochemical Induced VS_2/VO_x Heterostructures. *Adv. Funct. Mater.* **2021**, *31* (11), 2008743. https://doi.org/10.1002/adfm.202008743.

(77) Chen, Q.; Jin, J.; Song, M.; Zhang, X.; Li, H.; Zhang, J.; Hou, G.; Tang, Y.; Mai, L.; Zhou, L. High-Energy Aqueous Ammonium-Ion Hybrid Supercapacitors. *Adv. Mater.* **2022**, *34* (8), 2107992. https://doi.org/10.1002/adma.202107992.

(78) Tang, W.; Xie, Y.; Peng, F.; Yang, Y.; Feng, F.; Liao, X.-Z.; He, Y.-S.; Ma, Z.-F.; Chen, Z.; Ren, Y. Electrochemical Performance of $NaFeFe(CN)_6$ Prepared by Solid Reaction for Sodium Ion Batteries. *J. Electrochem. Soc.* **2018**, *165* (16), A3910. https://doi.org/10.1149/2.0701816jes.

(79) Xia, M.; Zhang, X.; Yu, H.; Yang, Z.; Chen, S.; Zhang, L.; Shui, M.; Xie, Y.; Shu, J. Hydrogen Bond Chemistry in $Fe_4[Fe(CN)_6]_3$ Host for Aqueous NH4+ Batteries. *Chem. Eng. J.* **2021**, *421*, 127759. https://doi.org/10.1016/j.cej.2020.127759.

(80) Jiao, S.; Tuo, J.; Xie, H.; Cai, Z.; Wang, S.; Zhu, J. The Electrochemical Performance of Cu3$[Fe(CN)_6]_2$ as a Cathode Material for Sodium-Ion Batteries. *Mater. Res. Bull.* **2017**, *86*, 194–200. https://doi.org/10.1016/j.materresbull.2016.10.019.

(81) Lee, S.-H.; Deshpande, R.; Parilla, P. A.; Jones, K. M.; To, B.; Mahan, A. H.; Dillon, A. C. Crystalline WO_3 Nanoparticles for Highly Improved Electrochromic

Applications. *Adv. Mater.* **2006**, *18* (6), 763–766. https://doi.org/10.1002/adma.200501953.

(82) Zheng, H.; Ou, J. Z.; Strano, M. S.; Kaner, R. B.; Mitchell, A.; Kalantar-zadeh, K. Nanostructured Tungsten Oxide – Properties, Synthesis, and Applications. *Adv. Funct. Mater.* **2011**, *21* (12), 2175–2196. https://doi.org/10.1002/adfm.201002477.

(83) Santato, C.; Odziemkowski, M.; Ulmann, M.; Augustynski, J. Crystallographically Oriented Mesoporous WO_3 Films: Synthesis, Characterization, and Applications. *J. Am. Chem. Soc.* **2001**, *123* (43), 10639–10649. https://doi.org/10.1021/ja011315x.

(84) Chen, C.; Zhu, H.; Shi, M.; Hu, L.; Xue, Z.; Ye, H.; Zhao, L.; Yan, C. Oxygen Vacancies-Modulated Tungsten Oxide Anode for Ultra-Stable and Fast Aqueous Aluminum-Ion Storage. *Energy Storage Mater.* **2022**, *49*, 370–379. https://doi.org/10.1016/j.ensm.2022.04.013.

(85) Yao, Y.; Sang, D.; Zou, L.; Wang, Q.; Liu, C. A Review on the Properties and Applications of WO_3 Nanostructure−Based Optical and Electronic Devices. *Nanomaterials* **2021**, *11* (8), 2136. https://doi.org/10.3390/nano11082136.

(86) Wang, G.; Ling, Y.; Wang, H.; Yang, X.; Wang, C.; Z. Zhang, J.; Li, Y. Hydrogen - Treated WO_3 Nanoflakes Show Enhanced Photostability. *Energy Environ. Sci.* **2012**, *5* (3), 6180–6187. https://doi.org/10.1039/C2EE03158B.

(87) Liu, P.; Wang, B.; Wang, C.; Ma, L.; Zhang, W.; Hopmann, E.; Liu, L.; Elezzabi, A. Y.; Li, H. Amorphous Tungsten Oxide Nanodots for Chromatic Applications. *Adv. Funct. Mater.* **2024**, *34* (34), 2400760. https://doi.org/10.1002/adfm.202400760.

(88) Li, A.; Tan, Y.; Wang, Y.; Cheng, C. Three-Dimensional Ordered Macroporous Amorphous WO3 Arrays for Zinc-Based Electrochromic Device with Large Light Modulation and Fast Switching. *Adv. Mater. Technol.* **2024**, *9* (5), 2301886. https://doi.org/10.1002/admt.202301886.

(89) Wen, X.; Luo, J.; Xiang, K.; Zhou, W.; Zhang, C.; Chen, H. High-Performance Monoclinic WO_3 Nanospheres with the Novel NH_4^+ Diffusion Behaviors for

Aqueous Ammonium-Ion Batteries. *Chem. Eng. J.* **2023**, *458*, 141381. https://doi.org/10.1016/j.cej.2023.141381.

(90) Low, J.; Yu, J.; Jaroniec, M.; Wageh, S.; Al-Ghamdi, A. A. Heterojunction Photocatalysts. *Adv. Mater.* **2017**, *29* (20), 1601694. https://doi.org/10.1002/adma.201601694.

(91) Wang, S.; Guan, B. Y.; Lou, X. W. D. Construction of $ZnIn_2S_4$–In_2O_3 Hierarchical Tubular Heterostructures for Efficient CO_2 Photoreduction. *J. Am. Chem. Soc.* **2018**, *140* (15), 5037–5040. https://doi.org/10.1021/jacs.8b02200.

(92) Wang, H.; Zhang, L.; Chen, Z.; Hu, J.; Li, S.; Wang, Z.; Liu, J.; Wang, X. Semiconductor Heterojunction Photocatalysts: Design, Construction, and Photocatalytic Performances. *Chem. Soc. Rev.* **2014**, *43* (15), 5234–5244. https://doi.org/10.1039/C4CS00126E.

(93) Li, R.; Zhang, F.; Wang, D.; Yang, J.; Li, M.; Zhu, J.; Zhou, X.; Han, H.; Li, C. Spatial Separation of Photogenerated Electrons and Holes among {010} and {110} Crystal Facets of $BiVO_4$. *Nat. Commun.* **2013**, *4* (1), 1432. https://doi.org/10.1038/ncomms2401.

(94) Liu, J.; Liu, Y.; Liu, N.; Han, Y.; Zhang, X.; Huang, H.; Lifshitz, Y.; Lee, S.-T.; Zhong, J.; Kang, Z. Metal-Free Efficient Photocatalyst for Stable Visible Water Splitting via a Two-Electron Pathway. *Science* **2015**, *347* (6225), 970–974. https://doi.org/10.1126/science.aaa3145.

(95) Ong, W.-J.; Tan, L.-L.; Ng, Y. H.; Yong, S.-T.; Chai, S.-P. Graphitic Carbon Nitride (g-C3N4)-Based Photocatalysts for Artificial Photosynthesis and Environmental Remediation: Are We a Step Closer To Achieving Sustainability? *Chem. Rev.* **2016**, *116* (12), 7159–7329. https://doi.org/10.1021/acs.chemrev.6b00075.

(96) Xiang, Q.; Yu, J.; Jaroniec, M. Graphene-Based Semiconductor Photocatalysts. *Chem. Soc. Rev.* **2012**, *41* (2), 782–796. https://doi.org/10.1039/C1CS15172J.

(97) Lewis, N. S. Research Opportunities to Advance Solar Energy Utilization. *Science* **2016**, *351* (6271), aad1920. https://doi.org/10.1126/science.aad1920.

(98) Barber, J. Photosynthetic Energy Conversion: Natural and Artificial. *Chem. Soc. Rev.* **2008**, *38* (1), 185–196. https://doi.org/10.1039/B802262N.

(99) Maeda, K.; Teramura, K.; Lu, D.; Takata, T.; Saito, N.; Inoue, Y.; Domen, K. Photocatalyst Releasing Hydrogen from Water. *Nature* **2006**, *440* (7082), 295–295. https://doi.org/10.1038/440295a.

(100) Mushtaq, M. A.; Kumar, A.; Yasin, G.; Arif, M.; Tabish, M.; Ibraheem, S.; Cai, X.; Ye, W.; Fang, X.; Saad, A.; Zhao, J.; Ji, S.; Yan, D. 3D Interconnected Porous Mo-Doped WO_3@CdS Hierarchical Hollow Heterostructures for Efficient Photoelectrochemical Nitrogen Reduction to Ammonia. *Appl. Catal. B Environ.* **2022**, *317*, 121711. https://doi.org/10.1016/j.apcatb.2022.121711.

(101) Dong, X.; Liang, J.; Li, H.; Wu, Z.; Zhang, L.; Deng, Y.; Yu, H.; Tao, Y.; Yang, Q.-H. Matching Electrode Lengths Enables the Practical Use of Asymmetric Fiber Supercapacitors with a High Energy Density. *Nano Energy* **2021**, *80*, 105523. https://doi.org/10.1016/j.nanoen.2020.105523.

(102) Li, C.; Dong, X.; Zhai, Z.; Huang, N.; Jiang, X.; Yang, N. High-Performance Flexible Supercapacitors Using Diamond Cloth. *J. Phys. Chem. C* **2025**, *129* (14), 6618–6627. https://doi.org/10.1021/acs.jpcc.5c00116.

(103) Kühne, T. D.; Iannuzzi, M.; Del Ben, M.; Rybkin, V. V.; Seewald, P.; Stein, F.; Laino, T.; Khaliullin, R. Z.; Schütt, O.; Schiffmann, F.; Golze, D.; Wilhelm, J.; Chulkov, S.; Bani-Hashemian, M. H.; Weber, V.; Borštnik, U.; Taillefumier, M.; Jakobovits, A. S.; Lazzaro, A.; Pabst, H.; Müller, T.; Schade, R.; Guidon, M.; Andermatt, S.; Holmberg, N.; Schenter, G. K.; Hehn, A.; Bussy, A.; Belleflamme, F.; Tabacchi, G.; Glöß, A.; Lass, M.; Bethune, I.; Mundy, C. J.; Plessl, C.; Watkins, M.; VandeVondele, J.; Krack, M.; Hutter, J. CP2K: An Electronic Structure and Molecular Dynamics Software Package - Quickstep: Efficient and Accurate Electronic Structure Calculations. *J. Chem. Phys.* **2020**, *152* (19), 194103. https://doi.org/10.1063/5.0007045.

(104) Han, J.; Varzi, A.; Passerini, S. The Emergence of Aqueous Ammonium-Ion Batteries. *Angew. Chem. Int. Ed.* **2022**, *61* (14), e202115046. https://doi.org/10.1002/anie.202115046.

(105) Dai, J.; Yang, Y.; Yu, J.; Fu, H.; Xu, Y.; Qin, Q.; Qi, X.; Dai, L.; Cabot, A. Aqueous Ammonium-Ion Hybrid Supercapacitors. *Chem. Eng. J.* **2024**, *500*, 157343. https://doi.org/10.1016/j.cej.2024.157343.

(106) Brezesinski, T.; Fattakhova Rohlfing, D.; Sallard, S.; Antonietti, M.; Smarsly, B. M. Highly Crystalline WO_3 Thin Films with Ordered 3D Mesoporosity and Improved Electrochromic Performance. *Small* **2006**, *2* (10), 1203–1211. https://doi.org/10.1002/smll.200600176.

(107) Zhou, J.; Ding, Y.; Deng, S. Z.; Gong, L.; Xu, N. S.; Wang, Z. L. Three-Dimensional Tungsten Oxide Nanowire Networks. *Adv. Mater.* **2005**, *17* (17), 2107–2110. https://doi.org/10.1002/adma.200500885.

(108) You Zheng, J.; Haider, Z.; Khue Van, T.; Uttam Pawar, A.; Jong Kang, M.; Woo Kim, C.; Soo Kang, Y. Tuning of the Crystal Engineering and Photoelectrochemical Properties of Crystalline Tungsten Oxide for Optoelectronic Device Applications. *CrystEngComm* **2015**, *17* (32), 6070–6093. https://doi.org/10.1039/C5CE00900F.

(109) Hutchins, M. G.; Abu-Alkhair, O.; El-Nahass, M. M.; El-Hady, K. A. Structural and Optical Characterisation of Thermally Evaporated Tungsten Trioxide (WO_3) Thin Films. *Mater. Chem. Phys.* **2006**, *98* (2), 401–405. https://doi.org/10.1016/j.matchemphys.2005.09.052.

(110) Cifre-Herrando, M.; Roselló-Márquez, G.; García-Antón, J.; Mais, L.; Mascia, M. Amorphous Surface Modification and Scalability of WO_3 Nanostructures for Photoelectrocatalytic Degradation of Organic Pollutants. *Electrochimica Acta* **2025**, *535*, 146706. https://doi.org/10.1016/j.electacta.2025.146706.

(111) Zhang, Y.; Zhao, L.; Yang, C.; Sun, S.; Wu, J.; Yao, L.; Liu, Z. Substrate Temperature-Controlled Amorphous-Crystalline Hybrid Structure in Tungsten Oxide

Thin Films for Comprehensive High-Efficiency Electrochromic Performance. *Surf. Interfaces* **2025**, *72*, 107404. https://doi.org/10.1016/j.surfin.2025.107404.

(112) Zhang, Z.; Mo, H.; Li, R.; Zhou, X.; Lin, Z.; Zhang, J.; Tang, X.; Zhan, Y.; Luo, J. The Counterbalancing Role of Oxygen Vacancy between the Electrochromic Properties and the Trapping Effect Passivation for Amorphous Tungsten Oxide Films. *Small Sci.* **2024**, *4* (3), 2300219. https://doi.org/10.1002/smsc.202300219.

(113) Osman, S.; Peng, C.; Li, F.; Chen, H.; Shen, J.; Zhong, Z.; Huang, W.; Xue, D.; Liu, J. Defect-Induced Dense Amorphous/Crystalline Heterophase Enables High-Rate and Ultrastable Sodium Storage. *Adv. Sci.* **2022**, *9* (36), 2205575. https://doi.org/10.1002/advs.202205575.

(114) Zhang, R.; Ning, F.; Xu, S.; Zhou, L.; Shao, M.; Wei, M. Oxygen Vacancy Engineering of WO_3 toward Largely Enhanced Photoelectrochemical Water Splitting. *Electrochimica Acta* **2018**, *274*, 217–223. https://doi.org/10.1016/j.electacta.2018.04.109.

(115) Zheng, J.; Meng, D.; Guo, J.; Liu, X.; Zhou, L.; Wang, Z. Defect Engineering for Enhanced Electrocatalytic Oxygen Reaction on Transition Metal Oxides: The Role of Metal Defects. *Adv. Mater.* **2024**, *36* (28), 2405129. https://doi.org/10.1002/adma.202405129.

(116) Alonzo, S. M. M.; Bentley, J.; Desai, S.; Bastakoti, B. P. Hydrothermal Synthesis of Hierarchical Microstructure Tungsten Oxide/Carbon Nanocomposite for Supercapacitor Application. *Sci. Rep.* **2023**, *13* (1), 21732. https://doi.org/10.1038/s41598-023-48958-w.

(117) Geng, X.; Vega-Paredes, M.; Wang, Z.; Ophus, C.; Lu, P.; Ma, Y.; Zhang, S.; Scheu, C.; Liebscher, C. H.; Gault, B. Grain Boundary Engineering for Efficient and Durable Electrocatalysis. *Nat. Commun.* **2024**, *15* (1), 8534. https://doi.org/10.1038/s41467-024-52919-w.

(118) Zhao, H.; Yu, X.; Yu, S.; Yang, H.; Guo, W.; Li, S.; Zheng, J. Y. Review on Amorphous WO_3 for Electrochromic Devices: Structure, Optimization Strategies and

Applications. *Mater. Today Chem.* **2025**, *43*, 102513. https://doi.org/10.1016/j.mtchem.2025.102513.

(119) Augustyn, V.; Simon, P.; Dunn, B. Pseudocapacitive Oxide Materials for High-Rate Electrochemical Energy Storage. *Energy Environ. Sci.* **2014**, *7* (5), 1597–1614. https://doi.org/10.1039/C3EE44164D.

(120) Albery, W. J.; O'Shea, G. J.; Smith, A. L. Interpretation and Use of Mott–Schottky Plots at the Semiconductor/Electrolyte Interface. *J. Chem. Soc. Faraday Trans.* **1996**, *92* (20), 4083–4085. https://doi.org/10.1039/FT9969204083.

(121) Han, L.; Luo, J.; Zhang, R.; Gong, W.; Chen, L.; Liu, F.; Ling, Y.; Dong, Y.; Yong, Z.; Zhang, Y.; Wei, L.; Zhang, X.; Zhang, Q.; Li, Q. Arrayed Heterostructures of MoS_2 Nanosheets Anchored TiN Nanowires as Efficient Pseudocapacitive Anodes for Fiber-Shaped Ammonium-Ion Asymmetric Supercapacitors. *ACS Nano* **2022**, *16* (9), 14951–14962. https://doi.org/10.1021/acsnano.2c05905.

(122) Zhou, G.; Li, M.-C.; Liu, C.; Wu, Q.; Mei, C. 3D Printed $Ti_3C_2T_x$ MXene/Cellulose Nanofiber Architectures for Solid-State Supercapacitors: Ink Rheology, 3D Printability, and Electrochemical Performance. *Adv. Funct. Mater.* **2022**, *32* (14), 2109593. https://doi.org/10.1002/adfm.202109593.

(123) Li, H.; Yu, R.; Chen, H.; Hu, J.; Zhang, J.; Hou, G.; Chen, Q.; Lu, J.; Tang, Y. Thiocyanate Coordination Regulates the Interlayer Ammonium Ion Storage Structure of Molybdenum Disulfide. *ACS Energy Lett.* **2025**, *10* (1), 168–176. https://doi.org/10.1021/acsenergylett.4c02712.

(124) Niu, K.; Shi, J.; Zhang, L.; Yue, Y.; Wang, M.; Zhang, Q.; Ma, Y.; Mo, S.; Li, S.; Li, W.; Wen, L.; Hou, Y.; Long, F.; Gao, Y. A Self-Healing Aqueous Ammonium-Ion Micro Batteries Based on PVA-NH_4Cl Hydrogel Electrolyte and MXene-Integrated Perylene Anode. *Nano Res. Energy* **2024**, *3* (4). https://doi.org/10.26599/NRE.2024.9120127.

(125) Teng, Y.; Wei, J.; Guo, T.; Zhou, Y.; Zhang, Z.; Su, Z.; Tam, K. C.; A. Wu, Y. High Performance Aqueous Asymmetric Supercapacitors Developed by Interfacial

Engineering Wood-Derived Nanostructured Electrodes. *Mater. Today Adv.* **2023**, *19*, 100391. https://doi.org/10.1016/j.mtadv.2023.100391.

(126) Grätzel, M. Photoelectrochemical Cells. *Nature* **2001**, *414* (6861), 338–344. https://doi.org/10.1038/35104607.

(127) Chen, X.; Shen, S.; Guo, L.; Mao, S. S. Semiconductor-Based Photocatalytic Hydrogen Generation. *Chem. Rev.* **2010**, *110* (11), 6503–6570. https://doi.org/10.1021/cr1001645.

(128) Schneider, J.; Matsuoka, M.; Takeuchi, M.; Zhang, J.; Horiuchi, Y.; Anpo, M.; Bahnemann, D. W. Understanding TiO_2 Photocatalysis: Mechanisms and Materials. *Chem. Rev.* **2014**, *114* (19), 9919–9986. https://doi.org/10.1021/cr5001892.

(129) Guo, Q.; Zhou, C.; Ma, Z.; Yang, X. Fundamentals of TiO_2 Photocatalysis: Concepts, Mechanisms, and Challenges. *Adv. Mater.* **2019**, *31* (50), 1901997. https://doi.org/10.1002/adma.201901997.

(130) Nakata, K.; Fujishima, A. TiO_2 Photocatalysis: Design and Applications. *J. Photochem. Photobiol. C Photochem. Rev.* **2012**, *13* (3), 169–189. https://doi.org/10.1016/j.jphotochemrev.2012.06.001.

(131) Li, Y.; Cheng, D.; Wei, Z.; Sautet, P. Photoelectron Storage at the WO_3/TiO_2 Interface: Modeling in Ambient Conditions from First-Principles Calculations. *ACS Catal.* **2023**, *13* (15), 9979–9986. https://doi.org/10.1021/acscatal.3c01756.

(132) Li, Y.; Zhang, X.; Qian, Z.; Wang, H.; Luo, S.; Li, G. Preparation of Self-Supported TiO_2/WO_3@W Electrode with a Nanostructure and Its Photoelectrocatalytic Performance. *Chem. Phys. Lett.* **2025**, *874–875*, 142176. https://doi.org/10.1016/j.cplett.2025.142176.

(133) Papp, J.; Soled, S.; Dwight, K.; Wold, A. Surface Acidity and Photocatalytic Activity of TiO_2, WO_3/TiO_2, and MoO_3/TiO_2 Photocatalysts. *Chem. Mater.* **1994**, *6* (4), 496–500. https://doi.org/10.1021/cm00040a026.

(134) Paramasivam, I.; Nah, Y.-C.; Das, C.; Shrestha, N. K.; Schmuki, P. WO_3/TiO_2 Nanotubes with Strongly Enhanced Photocatalytic Activity. *Chem. – Eur. J.* **2010**, *16* (30), 8993–8997. https://doi.org/10.1002/chem.201000397.

(135) Akurati, K. K.; Vital, A.; Dellemann, J.-P.; Michalow, K.; Graule, T.; Ferri, D.; Baiker, A. Flame-Made WO_3/TiO_2 Nanoparticles: Relation between Surface Acidity, Structure and Photocatalytic Activity. *Appl. Catal. B Environ.* **2008**, *79* (1), 53–62. https://doi.org/10.1016/j.apcatb.2007.09.036.

(136) Li, L.; Li, J.; Fang, F.; Zhang, Y.; Zhou, T.; Zhou, C.; Bai, J.; Zhou, B. Efficient H_2O_2 Production from Urine Treatment Based on a Self-Biased WO_3/TiO_2-Si PVC Photoanode and a WO_3/CMK-3 Cathode. *Appl. Catal. B Environ. Energy* **2023**, *333*, 122776. https://doi.org/10.1016/j.apcatb.2023.122776.

(137) Lee, M.-J.; Jeong, B.; Kim, D.; Kim, S.-J.; Choi, Y.; Ye, B.; Kim, D.-H.; Kim, H.-D.; Cho, S. Hexagonal Boron Nitride Heterostructure to Control the Oxidation States and SO_2 Resistance of the V_2O_5-WO_3/TiO_2 Catalyst for the NH_3-SCR Reaction across a Wide Temperature Range. *Appl. Catal. B Environ. Energy* **2025**, *378*, 125583. https://doi.org/10.1016/j.apcatb.2025.125583.

(138) Tada, H.; Kokubu, A.; Iwasaki, M.; Ito, S. Deactivation of the TiO_2 Photocatalyst by Coupling with WO_3 and the Electrochemically Assisted High Photocatalytic Activity of WO_3. *Langmuir* **2004**, *20* (11), 4665–4670. https://doi.org/10.1021/la036104f.

(139) Sang, L.; Zhao, Y.; Burda, C. TiO_2 Nanoparticles as Functional Building Blocks. *Chem. Rev.* **2014**, *114* (19), 9283–9318. https://doi.org/10.1021/cr400629p.

(140) Reghunath, S.; Pinheiro, D.; Kr, S. D. A Review of Hierarchical Nanostructures of TiO_2: Advances and Applications. *Appl. Surf. Sci. Adv.* **2021**, *3*, 100063. https://doi.org/10.1016/j.apsadv.2021.100063.

(141) Yokoya, T.; Nakamura, T.; Matsushita, T.; Muro, T.; Takano, Y.; Nagao, M.; Takenouchi, T.; Kawarada, H.; Oguchi, T. Origin of the Metallic Properties of

Heavily Boron-Doped Superconducting Diamond. *Nature* **2005**, *438* (7068), 647–650. https://doi.org/10.1038/nature04278.

(142) Einaga, Y. Boron-Doped Diamond Electrodes: Fundamentals for Electrochemical Applications. *Acc. Chem. Res.* **2022**, *55* (24), 3605–3615. https://doi.org/10.1021/acs.accounts.2c00597.

(143) Roy, N.; Hirano, Y.; Kuriyama, H.; Sudhagar, P.; Suzuki, N.; Katsumata, K.; Nakata, K.; Kondo, T.; Yuasa, M.; Serizawa, I.; Takayama, T.; Kudo, A.; Fujishima, A.; Terashima, C. Boron-Doped Diamond Semiconductor Electrodes: Efficient Photoelectrochemical CO_2 Reduction through Surface Modification. *Sci. Rep.* **2016**, *6* (1), 38010. https://doi.org/10.1038/srep38010.

(144) Yang, N.; Yu, S.; Macpherson, J. V.; Einaga, Y.; Zhao, H.; Zhao, G.; Swain, G. M.; Jiang, X. Conductive Diamond: Synthesis, Properties, and Electrochemical Applications. *Chem. Soc. Rev.* **2019**, *48* (1), 157–204. https://doi.org/10.1039/C7CS00757D.

(145) Yang, N.; Jiang, X. Rational Design of Diamond Electrodes. *Acc. Chem. Res.* **2023**, *56* (2), 117–127. https://doi.org/10.1021/acs.accounts.2c00644.

(146) Jian, Z.; Yang, N.; Vogel, M.; Zhou, Z.; Zhao, G.; Kienitz, P.; Schulte, A.; Schönherr, H.; Jiao, T.; Zhang, W.; Jiang, X. Tunable Photo-Electrochemistry of Patterned TiO_2/BDD Heterojunctions. *Small Methods* **2020**, *4* (9), 2000257. https://doi.org/10.1002/smtd.202000257.

(147) Yao, Y.; Sang, D.; Duan, S.; Wang, Q.; Liu, C. Excellent Optoelectronic Applications and Electrical Transport Behavior of the N-WO_3 Nanostructures/p-Diamond Heterojunction: A New Perspective. *Nanotechnology* **2021**, *32* (33), 332501. https://doi.org/10.1088/1361-6528/abfe24.

(148) Spătaru, N.; Preda, L.; Matei, E.; Satulu, V.; Mihai, M. A.; Radu, M. M.; Donath, C.; Moga, O. G.; Spătaru, T. Beneficial Role of Silicotungstic Acid Presence on the WO_3-Modified Boron-Doped Diamond Substrate on the Electrocatalytic Activity for

Methanol Anodic Oxidation of Supported Platinum. *Int. J. Hydrog. Energy* **2025**, *120*, 403–411. https://doi.org/10.1016/j.ijhydene.2025.03.327.

(149) Yao, Y.; Sang, D.; Duan, S.; Wang, Q.; Liu, C. Review on the Properties of Boron-Doped Diamond and One-Dimensional-Metal-Oxide Based P-N Heterojunction. *Molecules* **2021**, *26* (1), 71. https://doi.org/10.3390/molecules26010071.

(150) Chen, X.; Dong, X.; Zhang, C.; Zhu, M.; Ahmed, E.; Krishnamurthy, G.; Rouzbahani, R.; Pobedinskas, P.; Gauquelin, N.; Jannis, D.; Kaur, K.; Hafez, A. M. E.; Thiel, F.; Bornemann, R.; Engelhard, C.; Schönherr, H.; Verbeeck, J.; Haenen, K.; Jiang, X.; Yang, N. Interlayer Affected Diamond Electrochemistry. *Small Methods* **2025**, *9* (2), 2301774. https://doi.org/10.1002/smtd.202301774.

(151) Jian, Z.; Yang, N.; Vogel, M.; Leith, S.; Schulte, A.; Schoenherr, H.; Jiao, T.; Zhang, W.; Mueller, J.; Butz, B.; Jiang, X. Flexible Diamond Fibers for High-Energy-Density Zinc-Ion Supercapacitors. *Adv. Energy Mater.* **2020**, *10* (44), 2002202. https://doi.org/10.1002/aenm.202002202.

(152) Graebner, J. E.; Jin, S.; Kammlott, G. W.; Herb, J. A.; Gardinier, C. F. Unusually High Thermal Conductivity in Diamond Films. *Appl. Phys. Lett.* **1992**, *60* (13), 1576–1578. https://doi.org/10.1063/1.107256.

(153) Berman, R.; Simon, F. E.; Ziman, J. M. The Thermal Conductivity of Diamond at Low Temperatures. *Proc. R. Soc. Lond. Ser. Math. Phys. Sci.* **1997**, *220* (1141), 171–183. https://doi.org/10.1098/rspa.1953.0180.

(154) Wu, D.; Ma, Y. C.; Wang, Z. L.; Luo, Q.; Gu, C. Z.; Wang, N. L.; Li, C. Y.; Lu, X. Y.; Jin, Z. S. Optical Properties of Boron-Doped Diamond. *Phys. Rev. B* **2006**, *73* (1), 012501. https://doi.org/10.1103/PhysRevB.73.012501.

(155) Cobb, S. J.; Ayres, Z. J.; Macpherson, J. V. Boron Doped Diamond: A Designer Electrode Material for the Twenty-First Century. *Annu. Rev. Anal. Chem.* **2018**, *11*, 463–484. https://doi.org/10.1146/annurev-anchem-061417-010107.

(156) Muzyka, K.; Sun, J.; Haile Fereja, T.; Lan, Y.; Zhang, W.; Xu, G. Boron-Doped Diamond: Current Progress and Challenges in View of Electroanalytical Applications. *Anal. Methods* **2019**, *11* (4), 397–414. https://doi.org/10.1039/C8AY02197J.

(157) Krysova, H.; Vlckova-Zivcova, Z.; Barton, J.; Petrak, V.; Nesladek, M.; Cigler, P.; Kavan, L. Visible-Light Sensitization of Boron-Doped Nanocrystalline Diamond through Non-Covalent Surface Modification. *Phys. Chem. Chem. Phys.* **2014**, *17* (2), 1165–1172. https://doi.org/10.1039/C4CP04148H.

(158) Rycewicz, M.; Nosek, A.; Shin, D. H.; Ficek, M.; Buijnsters, J. G.; Bogdanowicz, R. The Effect of Boron Concentration on the Electrical, Morphological and Optical Properties of Boron-Doped Nanocrystalline Diamond Sheets: Tuning the Diamond-on-Graphene Vertical Junction. *Diam. Relat. Mater.* **2022**, *128*, 109225. https://doi.org/10.1016/j.diamond.2022.109225.